Thermal instabilities in a yield-stress fluid : from the laboratory to the planetary scale

Anna Massmeyer Massmeyer

Thèse

Pour l'obtention du grade de

DOCTEUR DE L'UNIVERSITÉ PARIS-SUD

Spécialité : PHYSIQUE

École Doctorale MIPEGE 534 : MODELISATION et INSTRUMENTATION EN PHYSIQUE, ENERGIE, GEOSCIENCES et ENVIRONNEMENT

Presentée par

Anna Maßmeyer

Sujet de la thèse :

Thermal instabilities in a yield-stress fluid: from the laboratory to the planetary scale

---

Directrice de thèse : Mme Anne Davaille

Co-direction : Mme Erika Di Giuseppe

Soutenue le 27 mai 2013 devant le jury composé de :

M.	Harold Auradou	Examinateur
M.	Patrick Cordier	Rapporteur
Mme	Anne Davaille	Directrice
Mme	Erika Di Giuseppe	Co-directrice
M.	Thibaut Divoux	Examinateur
M.	Chérif Nouar	Rapporteur
M.	Paul Tackley	Examinateur
Mme	Andréa Tommasi	Présidente du Jury

Remerciements

First of all I would like to thank my two "directrices de these", Anne Davaille and Erika Di Giuseppe. Thank you Anne, for all your help with administrative things making the first steps in France much easier, for all your ideas and the resulting discussions and for sending me to all the different workshops and conferences that helped to keep my interest on the work awake during the whole thesis. Thanks to Erika who became a good friend. Thank you for introducing me with your great pedagogic skills to the world of rheology, sharing your knowledge and experience with me and for the plenty discussions we had, that always pushed me a large step forward. Thank you for being my travel planner, hostel during RER-problems, your friendship and so much more, I cannot list everything here...

I would also like to thank Paul Tackley and Tobias Rolf for the collaboration that largely improved our understanding of the laboratory system. Thanks to Tobi for patiently answering my emails and for taking your time to introduce me to the numerical code when I was in Zürich.

Thanks to the two "rapporteurs" Patrick Cordier and Chérif Nouar reading the thesis and your helpful comments and the discussion during and after the defence. Another big thanks to Thibaut Divoux who detailly read and commented the thesis, showing that some things which I thought they were clear needed to be precised, as well as Andréa Tommasi, Paul Tackley and Harold Auradou for the discussions during the defence.

Thanks to my hosts Kathrin & Marcel and Maike & Martin as well as my office mates there, Diana and Bettina, for having a good time in Zürich. Thanks to all the people that made the conferences and workshops so great, especially the "C2P gang" Sonja, Tobi, Marcel, Roberto, Kate, Erwin, Diana, Zhonghai, Flora and Katherine and last but not least Jenny and her continuous supply with Alpen Müsli.

And now coming back to France and FAST! Many thanks to Francois and Georg for the walks towards home, allowing to slowly "shut down", repassing the day and discussing open questions in research and "real life". Thank you Flo, the patient French teacher "alors, tu as mangé quoi hier soir", good friend and holiday planner who convinced me to drive her through Ireland to see the Giant's Causeway, she was the horoscope reader, but only until Sandeep arrived, who gratefully took over this job. Thank you for all the after-work beers, now the Skype meetings and your great Indian Chicken Curry. Thanks to his "mother" Ching, for organizing great events as the "international food day" and her twin sister Symphony, to Jessica and Francisco for organizing picnics, the "king of swearing" Cyril, Severine (even though we did not meet a lot due to different working hours), Fabien for Carbopol related questions and your great cakes, Manish and Bindiya and Awadhesh and Rashmi for hosting me the last days with great Indian food every evening! And special thanks to Mourad (and Sonia) for their warm welcome in Rio as well as Zhonghai for showing us great places in Beijing! Thanks to Yann and Guillaume for having a nice time in the office and to Georges for your support and discussions.

I would also like to thank Alban, Lionel, Rafael and Christian who where always available when there was a technical problem and to Mai and Monique who helped with the bureaucracy concerning the CNRS and travel related questions.

Thanks to Rona for diverse activity in and around Orsay and Oslo, I always enjoyed it when you had to come back to Orsay! Thanks to those who made their way over to France to visit me, as there are Klaus, Nina, Nils, Konrad, André, Karla and Horst. Among this group are also my sister and parents whom I would especially like to thank for their continuous moral support.

And definitely not to forget - the most frequent traveller Robert! Thank you for your support and the every-evening telephone calls, for making the little time that those few weekends were always such a precious time. Thanks for your patience, your curiosity and your enthusiasm.

Abstract

Thermal instabilities in a yield-stress fluid: from the laboratory to the planetary scale

Plumes are known to migrate through the ductile quasi-Newtonian mantle, while dikes fracture and propagate through the solid lithosphere. However, depending on the timescale, the lithosphere presents solid as well as viscous properties. To determine what happens in the complex case, where instabilities propagate through a visco-elastic matrix, we performed a combined study of laboratory experiments and numerical simulations. Here we investigate the development of thermal plumes in aqueous solutions of Carbopol, a polymer gel, forming a continuous network of micrometric sponges. This fluid is shear thinning and has a yield-stress σ_0, whereby flow occurs only if the local stress exceeds this critical value σ_0. Below this value, the fluid acts as an elastic solid. The rheological properties of the solutions can be systematically varied by varying the Carbopol concentration. The setup consists of a localized heat-source operated at constant power, placed at the centre of a square tank.

Depending on the ratio of the thermally induced stresses and the yield stress, Y_0, three different regimes may be obtained. For low $Y_0 < Y_{c1}$ no motion occurs, whereas for $Y_{c1} < Y_0 < Y_{c2}$ a cell develops, that evolves into a plume for $Y_0 > Y_{c2}$. We show that the critical parameters (Y_{c1}, Y_{c2}) strongly depend on the geometry of the heating.

Combined temperature and velocity field measurements show that the morphology of the plume resembles a finger, contrary to the mushroom-like shape encountered in Newtonian fluids. Numerical simulations using a purely viscous description, where the rheology of the fluid is described by a regularized Herschel-Bulkley model, are sufficient to capture the plume dynamics.

A detailed parametric study shows that the plume dynamics are governed by the interplay between yield stress, buoyancy induced stress and viscous stresses. We identify two non-dimensional parameters: the yield parameter Ψ comparing the buoyancy induced stress to the yield stress, and the Bingham number Bi comparing the yield stress to the viscous stresses. We show that a plume can rise only if both parameters are supercritical, i.e. if buoyancy induced stress and viscous stresses each overcome the yield stress. Therefore the plume may come to a halt before it reaches the surface.

We propose scaling laws for the plume stem velocity, temperature and the size of the shear zone in the steady state. We show that the scaling laws describe the behaviour in the plume stem reasonably well, if the yield stress is neglected and only the shear thinning behaviour is taken into account.

Applying the non-dimensional parameters to Earth places severe constraints on the strength of mantle and lithosphere. The maximum strength that allows for thermal instabilities to penetrate the lithosphere or upper mantle is in between 100 kPa and 100 MPa, and strongly depends on the size and buoyancy of the anomaly.

Résumé

Instabilités thermiques dans un fluide à seuil : de l'échelle du laboratoire à celle de la planète

Des panaches sont connus pour migrer à travers le manteau ductile et quasi-Newtonien ; alors que les dikes se fracturent et se propagent dans la lithosphère solide. Cependant, la lithosphère est en fait visco-élastique. Afin de déterminer ce qui se passe dans ce cas complexe, nous avons réalisé une étude expérimentale et numérique sur le développement de panaches thermiques dans des solutions aqueuses de Carbopol, un gel de polymères formant une réseau continu d'éponges microscopiques. Ce fluide est rhéofluidifiant et présente un seuil de contrainte σ_0, de sorte que l'écoulement ne se produit que si la contrainte locale dépasse cette valeur critique σ_0. En dessous de cette valeur, le fluide agit comme un solide élastique. Les propriétés rhéologiques des solutions peuvent être systématiquement ajustées en variant la concentration de Carbopol. Le dispositif consiste en une source locale de chaleur de puissance constante placée au centre d'une cuve cubique.

Selon la valeur du rapport entre la contrainte d'origine thermique et la contrainte seuil, Y_0, on peut observer trois régimes différents. A faible $Y_0 < Y_{c1}$, aucun movement n'est détecté; tandis que pour $Y_{c1} < Y_0 < Y_{c2}$ une cellule se développe, puis évolve vers un panache pour $Y_0 > Y_{c2}$. Nous montrons que les paramètres critiques (Y_{c1}, Y_{c2}) dépendent fortement de la géométrie du chauffage.

Des mesures simultanées de température et de champs de vitesse montrent que la morphologie du panache ressemble à un doigt, contrairement à la forme de champignon rencontrée dans les fluides newtoniens. Utilisant des simulations numériques avec une description purement visqueuse, où la rhéologie du fluide est décrite par un modèle de Herschel-Bulkley régularisé, sont suffisantes pour rendre compte de la dynamique du panache.

Une étude détaillée des paramètres indiquent que la dynamique du panache est gouvernée par la compétition entre la contrainte seuil, la contrainte induite par la flottabilité et les contraintes visqueuses. Nous avons identifié deux paramètres adimensionnés : le paramètre seuil Ψ comparant la contrainte induite par la flottabilité et la contrainte seuil, et le nombre de Bingham Bi comparant la contrainte seuil et les contraintes visqueuses. Un panache ne peut s'élever que si les deux paramètres sont supercritiques, i.e. la contrainte induite par la flottabilité et les contraintes visqueuses sont plus importantes que la contrainte seuil. Par conséquent, le panache peut s'arrêter avant d'atteindre la surface.

Des lois d'échelles dans le conduit du panache ont été determinées pour la vitesse, la température et la taille de la région cisaillée en régime permanent. Elles décrivent raisonnablement le comportement du conduit bien que seul l'effet rhéofluidifiant soit pris en compte.

L'application de ces paramètres adimmensionnées à la Terre contraignent significativement la limite de plasticité du manteau et de la lithosphère. Le contrainte seuil maximale qui permet à une instabilité thermique de pénétrer dans la lithosphère ou le manteau supérieur est entre 100 kPa et 100 MPa, et elle dépend fortement de la taille et de l'anomalie de densité de l'intrusion.

Contents

1. Introduction

The three terrestrial planets - Venus, Earth and Mars - have a similar composition and consist mainly of silicate rocks and metals. Therefore they are also referred to as silicate planets, moreover Venus and Earth are of comparable size. After accretion, all three planets separated into at least three different layers: a core, a mantle and a crust. The rheological behaviour of mantle and crust strongly depends on the time scale where load (stress) is applied and the observed time scale. Hence on a "human" timescale they behave as a solid, whereas they may deform like a viscous fluid on a geological timescale of several 100 Mio. years. Due to the planet being in a cold universe, the planet is cooled from the surface. On the other end, at the core mantle boundary (CMB) the mantle is heated. Hence the dense material will sink into the mantle, while the hot material from the CMB rises, i.e. the planetary mantle convects. These large-scale motions are responsible for volcanism, or on Earth for the formation of plates at mid-ocean ridges, which then spread, cool and sink back into the mantle at subduction zones. Therefore mantle convection is an important mechanism to cool a planet.

Despite their similar composition and size, surface dynamics on Earth, Mars and Venus are very different. Some crustal rocks on Mars formed 4.5 Gyr (billion years) ago (e.g. *Hartmann and Neukum [2001]*) and in most models mars is assumed to be in the *stagnant lid* mode (e.g. *Reese and Solomatov [1998]*), where the cold thermal boundary layer is not participating in mantle convection. The surface of Venus is younger than a billion years (*Schaber et al. [1992]*) which may be due to an episodic resurfacing event about 500 million years ago (e.g. *Schaber et al. [1992], Turcotte [1993]*). The youngest surface can be found on Earth, where 60 % are renewed continuously. Earth's surface is composed of several plates. The plates are formed at mid-ocean ridges and sink as downgoing sheets into the mantle at subduction zones. Deformation of the plates is strongly localized to the plate boundaries, which are regions of high seismicity (cf. fig. 1.1). The plates form a network of cold cells. Inside such a cell hot mantle plumes rise, which manifest themselves by hotspot volcanism at the surface (cf. circles in fig. 1.1).
The key-mechanism leading to these different surface expressions on the different planets, is rheology. This chapter is therefore dedicated to give an overview about the structure and rheology of the Earth and convection models employing different rheologies, leading to convection with different surface expressions.

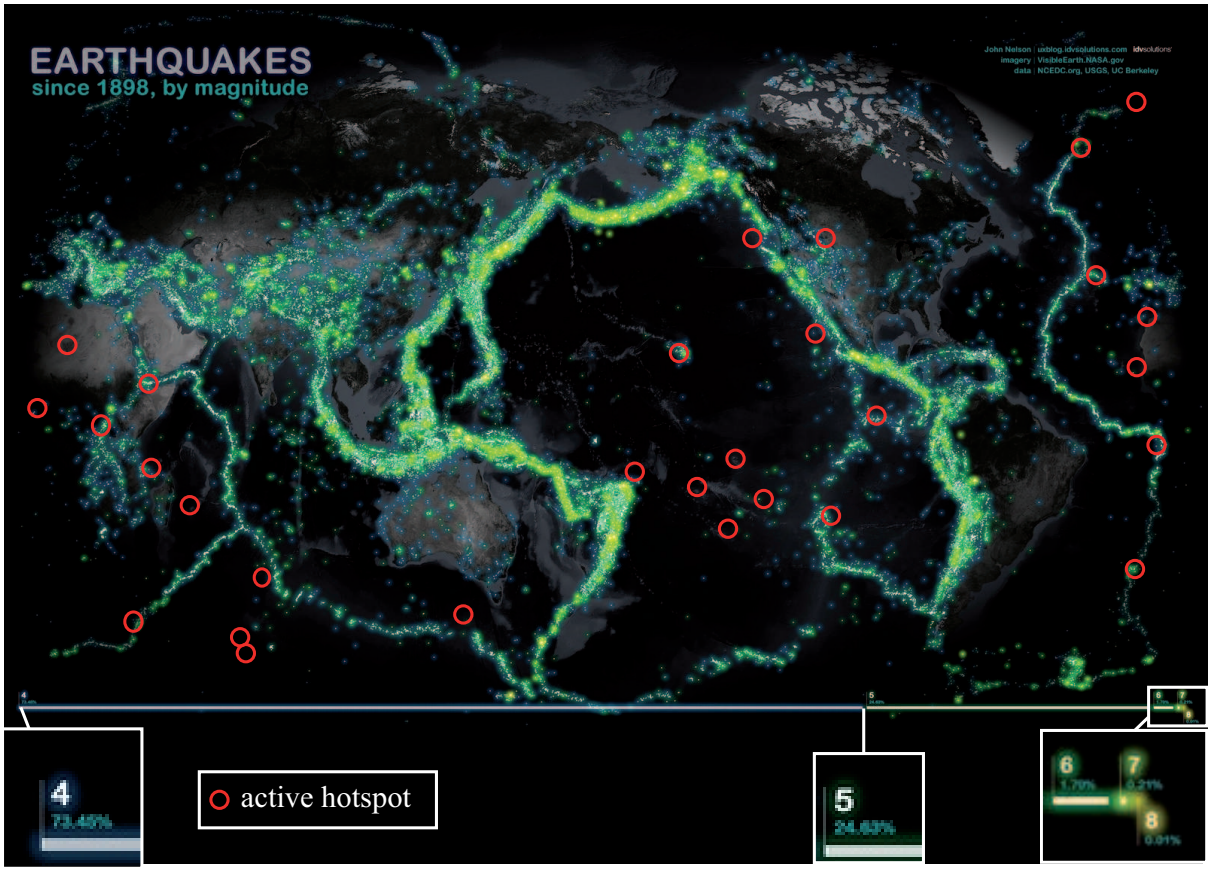

Figure 1.1.: Image ©by John Nelson. Earthquakes recorded since 1898, sorted by magnitude. Red-circles: current location of hotspot volcanism (cf. *Davaille et al. [2005]*).

1.1. The Earth

Earth's internal structure is composed of a solid iron core at the center of the liquid outer core that consists mostly of iron and where the Earth's magnetic field is generated, enclosed by the mantle that forms the outer shell of the planet. The basic understanding of the Earth's structure (fig. 1.2 after *Davies [1999]*), is based on seismological observations and experiments at high pressure and temperature that study the mineralogical structure at Earth's mantle conditions. The mantle rocks undergo several phase changes as pressure and temperature increase with depth. Those changes are recorded as seismic discontinuities and may affect mantle dynamics. At 410 km olivine transforms to Wadsleyite, that undergoes another phase change to Ringwoodite at 520 km that transforms to silicate perovskite at 660 km. Perovskite then might undergo another phase transition to post-perovskite (cf. *Murakami et al. [2004], Oganov and Ono [2004]*) at 2600 km depth. The temperature at the core mantle boundary (CMB) is not well constrained (cf. *Lay et al. [2008]* and references therein) and is in between $3300 - 4300$ K. For a hot CMB, another phase transition might then occur above the core mantle boundary, from post-perovskite back to perovskite (*Hernlund et al. [2005]*). While the 660 km phase transition is endothermic, all other transitions are exothermic. Therefore, e.g. due to the release of latent heat, they may have severe influence on the dynamics of the mantle. The lower and upper thermal boundary layers (TBL) of the convecting mantle correspond to the D"-layer and the lithosphere respectively.

1.2. Rheology of the Earth

Rheology studies the flow of a continuous body or liquid as a response to an applied force. For Earth this may be for example the forces exerted by the convecting mantle on the lithosphere. This section will therefore first explain the basic rheological terms which will then be used to discuss the rheology of the Earth.

1.2.1. Basic Rheological Terms

1.2.1.1. Stress and Deformation

The force exerted on an infinitesimal plane whose orientation is specified by the normal vector $\hat{n}$ is called traction $t(\hat{n})$ (fig. 1.3A). Traction across a surface within a continuous body is linked to the stress σ at this point via Cauchy's formula, which is written as

$$t_i(\hat{n}) = \sigma_{ij}\, n_j \tag{1.1}$$

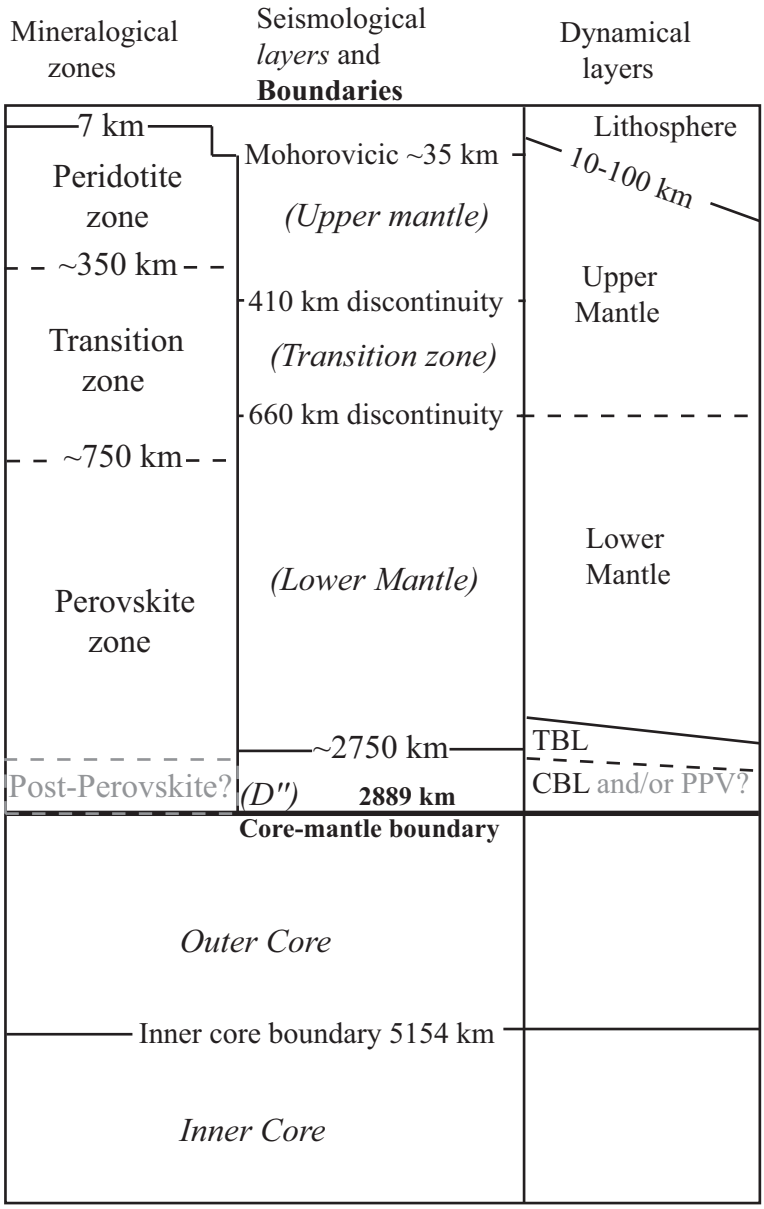

Figure 1.2.: Schematic picture of the Earth after *Davies [1999]*, with mineralogical zones, seismological observations and dynamical layers. Grey zones: post-perovskite (PPV, cf. *Murakami et al. [2004]*, *Oganov and Ono [2004]*) as a possible mineralogical and dynamical phase in the D"-layer. The dynamical thermal boundary layer (TBL) roughly corresponds to the seismological D"-layer.

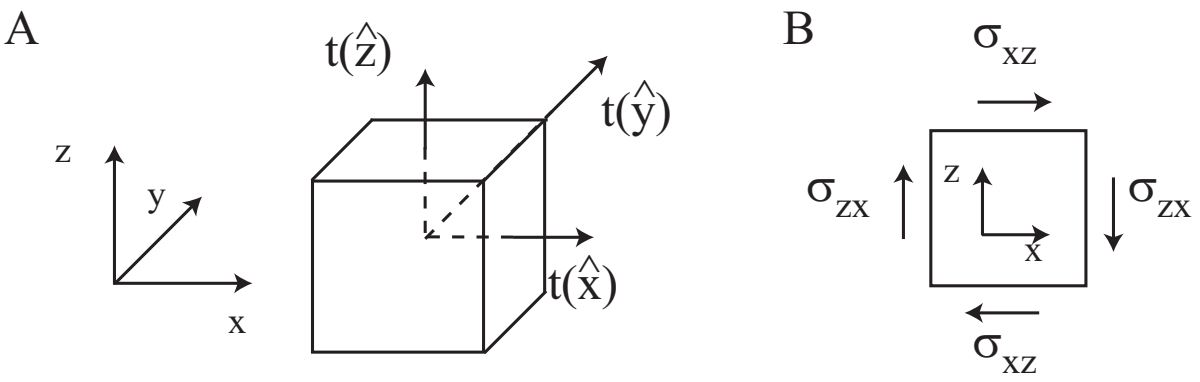

Figure 1.3.: A: traction vectors describing forces on faces of an infinitesimal cube, where $\hat{x}$, $\hat{y}$ and $\hat{z}$ are the normal vectors in the direction of x, y and z respectively. B: shear stress acting on a square. A and B Modified after *Shearer [1999]*.

A material deforms under an applied stress. In a continuum, this deformation is reflected in the displacement of the position of points and can be expressed as the sum of strain and solid body rotation. In the infinitesimal strain theory, the infinitesimal strain tensor is symmetric and is written as

$$\varepsilon_{ij} \equiv \frac{1}{2}\left(\frac{\partial u_i}{\partial x_j} + \frac{\partial u_j}{\partial x_i}\right) , \tag{1.2}$$

where $\mathbf{u} = (u_x, u_y, u_z)$ is the displacement. The tensor for rigid body rotation is asymmetric and is written as

$$\omega_{ij} \equiv \frac{1}{2}\left(\frac{\partial u_i}{\partial x_j} - \frac{\partial u_j}{\partial x_i}\right) . \tag{1.3}$$

Deformation is therefore expressed as

$$\frac{\partial u_i}{\partial x_j} = \frac{1}{2}\left(\frac{\partial u_i}{\partial x_j} + \frac{\partial u_j}{\partial x_i}\right) + \frac{1}{2}\left(\frac{\partial u_i}{\partial x_j} - \frac{\partial u_j}{\partial x_i}\right) . \tag{1.4}$$

Fig. 1.4A illustrates the deformation of a 2D square under strain (no rotation) assuming conservation of volume. The latter requires $\frac{\partial u_x}{\partial x} = \frac{\partial u_z}{\partial z} = 0$ and $\frac{\partial u_x}{\partial z} = \frac{\partial u_z}{\partial x}$ and therefore deformation is given by

$$\varepsilon = \begin{bmatrix} 0 & \theta \\ \theta & 0 \end{bmatrix} = \begin{bmatrix} 0 & \frac{\partial u_x}{\partial z} \\ \frac{\partial u_z}{\partial x} & 0 \end{bmatrix} , \tag{1.5}$$

with θ being the angle of rotation of each side. The rigid body rotation (fig. 1.4B) requires $\frac{\partial u_x}{\partial z} = -\frac{\partial u_z}{\partial x}$ and is written as

$$\omega = \begin{bmatrix} 0 & \theta \\ -\theta & 0 \end{bmatrix} = \begin{bmatrix} 0 & \frac{\partial u_x}{\partial z} \\ \frac{\partial u_z}{\partial x} & 0 \end{bmatrix} . \tag{1.6}$$

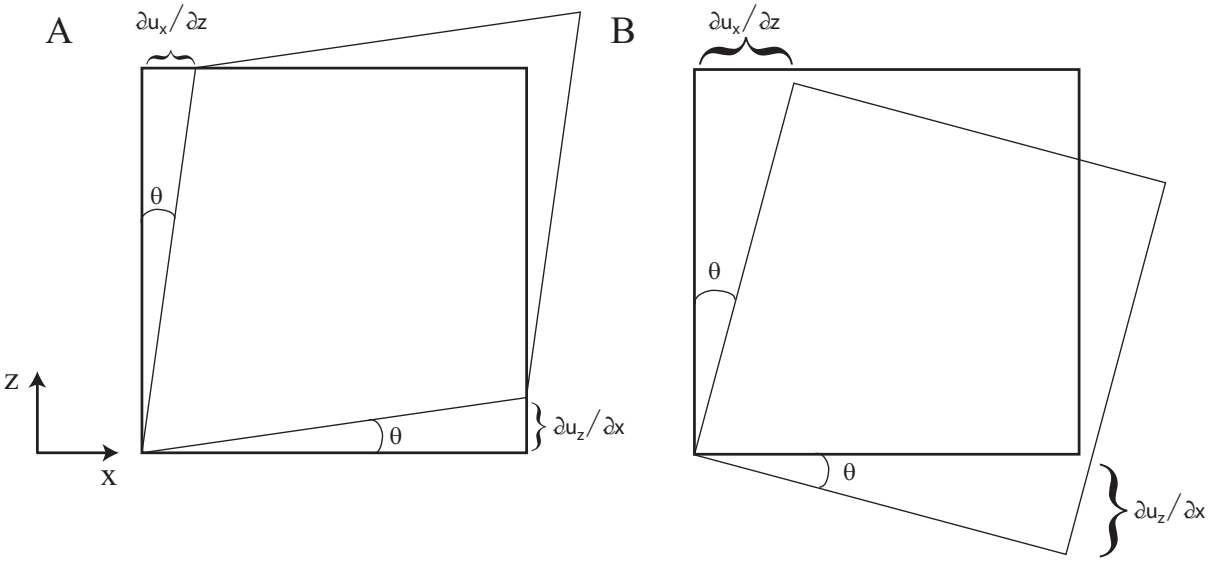

Figure 1.4.: Different effects of strain tensor ε_{ij} (A) and rotation ω_{ij} (B), illustrated by the deformation of a square in the x-z-plane, modified from *Shearer [1999]*.

1.2.1.2. Elasticity

In a purely elastic material, stress is linearly proportional to strain (fig. 1.5A). A continuous elastic body deforming instantaneously under an applied stress, can recover from this deformation. The relationship is called Hooke's law, which describes for example the deformation of a spring. In its general form it is written as

$$\sigma_{ij} = c_{ijkl} e_{kl}, \tag{1.7}$$

where c_{ijkl} is the elastic tensor. For an isotropic material it is written as

$$\sigma_{ij} = \lambda \delta_{ij} e_{kk} + 2\mu' e_{ij} \tag{1.8}$$

where λ and μ' are the Lamé parameters and δ_{ij} is the Kronecker delta.

1.2.1.3. Viscosity

Viscosity is the resistance of a fluid to flow under an applied stress. The mechanical analog to viscosity is the dashpot (fig. 1.5B). While elastic deformation is instantaneous, viscous deformation occurs in steady state. Therefore the time over which deformation, due to an exerted stress, occurs becomes important. Therefore in a viscous material stress

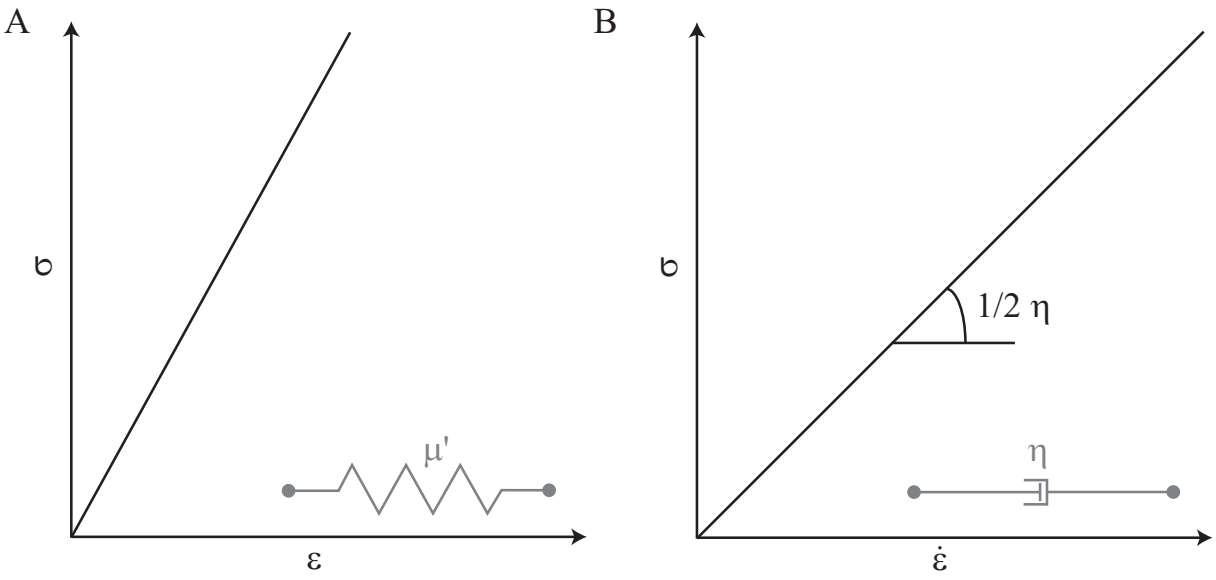

Figure 1.5.: A: Stress-strain relationship for purely elastic material, whose mechanical analogue is represented by a spring with rigidity μ'. B: stress-strain rate relationship for a purely viscous material, whose mechanical analog is described by a dashpot. Modified from *Ranalli [1995]*.

is proportional to the strain rate. For a Newtonian fluid the stress strain rate relationship is linear and is therefore written as

$$\sigma_{ij} = \frac{\mu}{\rho}\,\dot{\varepsilon}_{ij} = \eta\,\dot{\varepsilon}_{ij}\,, \tag{1.9}$$

where μ is the kinematic viscosity, ρ the density and η is the dynamic viscosity. If the viscosity is Non-Newtonian, the stress-strain rate relationship is non-linear, in most cases the viscosity then decreases with increasing stress (*Poirier [1985]*).

1.2.1.4. Visco-Plasticity

In a perfectly plastic solid, deformation occurs elastically until the yield stress σ_0 (limit of plasticity) is reached above which a permanent strain appears and deformation becomes irreversible (*Poirier [1985]*). If plastic deformation is achieved by imposing a constant strain rate that results in plastic strain, the object will deform at constant stress (fig. 1.6A). Above the yield stress, the stress-strain rate relationship is linear, therefore stress increases with increasing strain rate (fig. 1.6B).

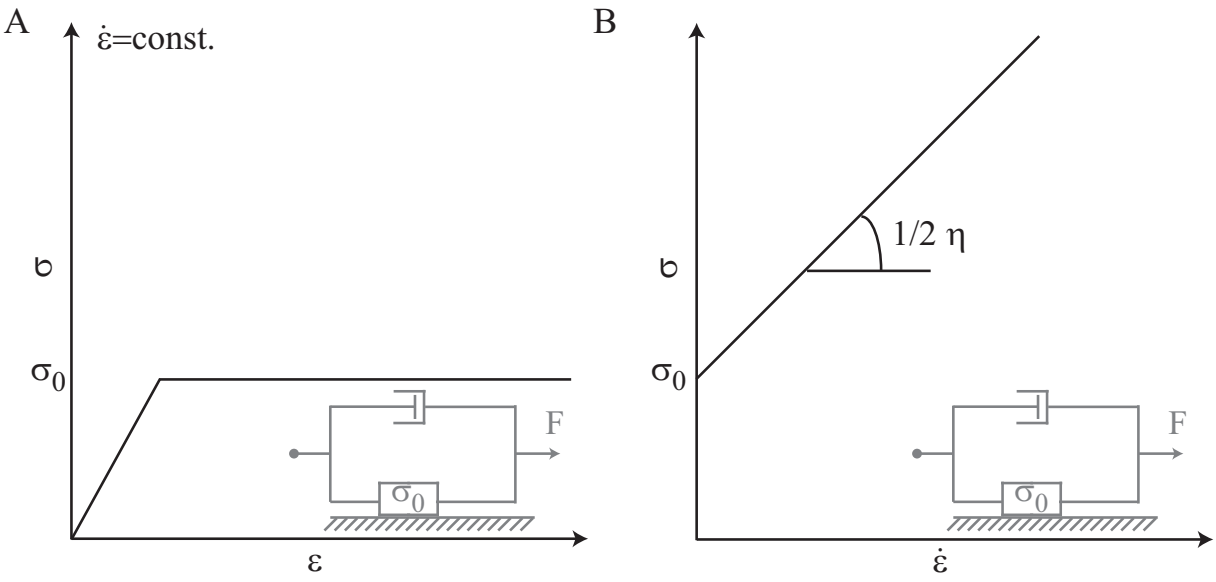

Figure 1.6.: A: Stress-strain relationship for a perfect plastic material at constant shear rate, whose mechanical analogue is represented by a parallel combination of a dashpot and a friction block. B: stress-strain rate relationship for a perfect plastic material.

1.2.1.5. Relationship Between the Deformation of Rocks and Non-Newtonian Fluids

Due to the definition of a viscosity, the deformation of a plastic solid, like rocks, may be compared to the behaviour of a fluid. Like in solids, many fluids have a non-Newtonian viscosity and may only flow, if the yield stress, which is due to the structure of the fluid, is exceeded. Consequently, those fluids are called non-Newtonian fluids. Below σ_0 deformation is elastic and therefore reversible. Different models for yield stress fluids exist, e.g. the Bingham model or the Herschel-Bulkley model. Their general expression in the community of fluid dynamics is

$$\sigma = \sigma_0 + K_\nu \dot{\gamma}^n \tag{1.10}$$

where $\dot{\gamma}$ is the shear rate and K_ν the consistency. For the Bingham model $n = 1$, i.e. once the yield stress is exceeded, the stress-strain rate relationship is linear (fig. 1.7 red dash-dotted curve) and it flows like a Newtonian fluid (fig. 1.7 black straight curve). The Bingham model (*Bingham [1916]*) is a special case of the Herschel-Bulkley model (*Herschel and Bulkley [1926]*). For a shear thinning fluid $n < 1$ (fig. 1.7 green dashed curve) viscosity decreases with increasing shear rate whereas it increases with increasing shear rate for a shear thickening fluid where $n > 1$ (fig. 1.7 blue dotted curve). To avoid confusion with the notation in the geophysics community, the shear rate dependence for geophysical systems will be expressed with n_E (adding the index E for Earth) as the

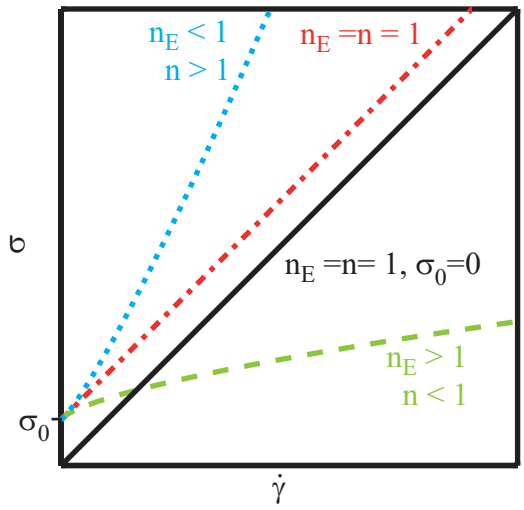

Figure 1.7: Schematic stress-shearrate relation for different rheologies. Black straight curve: Newtonian fluid, red dash-dotted curve: Bingham fluid, green dashed curve: shear thinning fluid and blue dotted curve: shear thickening fluid.

definition of the shear thinning exponents in the two communities is different. In the geophysics community (e.g. *Solomatov [1995]*, *Scott and Kohlstedt [2006]*), the shear-rate dependence is normally expressed as

$$\eta \propto \frac{1}{\dot{\gamma}^{\frac{n_E-1}{n_E}}}. \tag{1.11}$$

Comparing the two formulations this implies

$$\begin{aligned} &\text{Fluid dynamics} \quad \text{Geophysics} \\ \dot{\gamma}^{n-1} =& \dot{\gamma}^{\frac{1-n_E}{n_E}} \\ \Longleftrightarrow n-1 =& \frac{1}{n_E} - 1 \\ \Longleftrightarrow n =& \frac{1}{n_E}. \end{aligned} \tag{1.12}$$

Therefore in the geophysics community $n_E > 1$ indicates that the fluid is shear thinning, while it is shear thickening for $n_E < 1$ (cf. fig. 1.7).

1.2.2. Physics of deformation of solids

Due to its imperfectness, a crystalline solid can deform in two ways. In diffusion creep shear is transported by the propagation of point defects through the crystal, whereas shear rate is transported in the case of dislocation creep, by the propagation of line defects.

Diffusion creep Under an applied stress, the chemical potential changes, as vacancies are created at the grain boundaries perpendicular to the direction of lowest stress (fig.

1.8). Therefore vacancies will flow towards the lower potential, whereas atoms move in the opposite direction. The stress-strain rate dependence is then written as

$$\dot{\varepsilon} \propto \frac{D_{creep}}{d^p}\sigma \tag{1.13}$$

with d being the grain size, p the grain size exponent. From Fick's law follows the diffusion coefficient $D_{creep} = D_0 \exp(-Q/RT)$ with Q being the activation energy for creep and R being the universal gas constant. This shows, that creep flow is getting easier at higher temperatures. Furthermore the mechanism is becoming more effective for smaller grain sizes. The grain size exponent depends on how the vacancy propagates. If vacancies propagate through the crystal, this is called Nabarro-Herring creep and the grain size exponent is $p = 2$, whereas a propagation along grain boundaries is referred to as Coble creep and the grain size index is $p = 3$. The constant relating stress and strain rate is then the viscosity that, in this case, strongly depends on temperature.

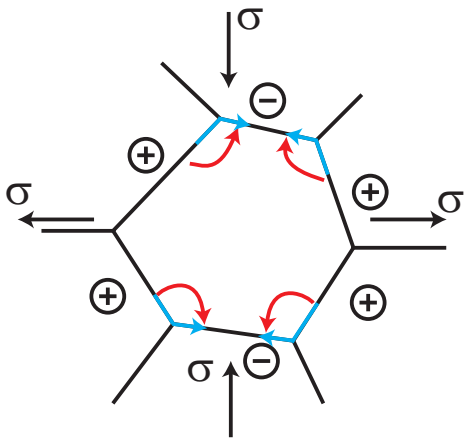

Figure 1.8.: Schematic illustration of diffusion creep: propagation of a point defect. Red paths: Nabarro-Herring creep, where the vacancy moves through the crystal, blue paths: Coble creep, where the vacancy moves along grain-boundaries. Diffusion creep depends on grain-size ($n_E = 1$, $p = 2$ for Nabarro Herring creep and $p = 3$ for Coble creep).

Dislocation creep At lower temperatures, the dominant creep is due to the propagation of line defects through the crystal lattice. This mechanism is called dislocation creep.

$$\dot{\varepsilon} \propto (\sigma - \sigma_0)^{n_E} \exp(-Q/RT) \tag{1.14}$$

While the propagation of a point defect results in a linear stress-strain rate relationship, the propagation of a line defect results in a non-linear relationship. In the case of rocks, the stress exponent is generally in between $n_E = 2 - 4.5$ (*Ranalli [1995]*). Which mechanism

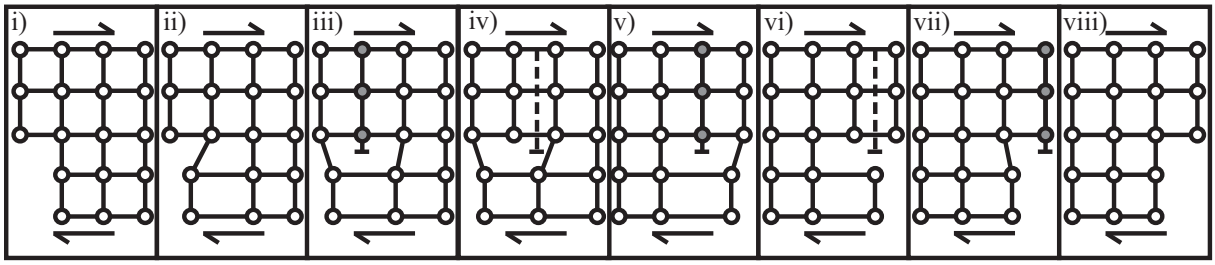

Figure 1.9.: Schematic illustration of dislocation creep: propagation of a line defect through the crystal lattice.

dominates the creep behaviour, strongly depends on several factors. In dislocation creep the stress exponent, activation energy and activation volume are higher than in the case of diffusion creep, whereas the grain size exponent is lower. Consequently, at low stresses, small grain size, low temperature and high pressure, diffusion dominates over dislocation creep (*Karato and Wu [1993]*).

1.2.3. Deformation mechanisms in the Earth's mantle

While most of the mantle deforms under ductile creep, deformation in the upper few kilometres occurs in form of fracture, when grains and crystals are sliding past each other. This is due to the brittle strength σ_b being smaller in this region, than the plastic (ductile) strength σ_p of the rock (fig. 1.10). With increasing depth, brittle and ductile strength are in the same order of magnitude (brittle-ductile transition zone, fig. 1.10), whereby the depth-extend of the brittle-ductile transition zone depends for example on the composition of rocks as well as the strain rate. With increasing strain rate, the ductile creep curve is shifted to deeper levels in the mantle.

In the ductile regime a viscosity can be defined. The viscosity then depends on grain size (*Platt and Behr [2011], Demouchy et al. [2012]*) and stress (*Karato [1986], Ranalli [1995]*), but also on temperature (*Mei and Kohlstedt [2000], Chopra and Paterson [1984], Karato [1986], Hirth and Kohlstedt [1996], Kohlstedt and Zimmerman [1996]*), water fugacity (*Bai et al. [1991], Karato and Jung [2003]*) and melt content (*Karato [1986], Karato and Wu [1993], Hirth and Kohlstedt [1996], Kohlstedt and Zimmerman [1996], Karato and Jung [2003]*). After *Hirth and Kohlstedt [2003]* the deformation rate is then given by

$$\dot{\varepsilon} = A\,\sigma^{n_E}\,d^{-p} f_{H_2O}\,exp\left(\beta\,\Phi\right)\,exp\left(-\frac{E^* + P\,V^*}{RT}\right), \tag{1.15}$$

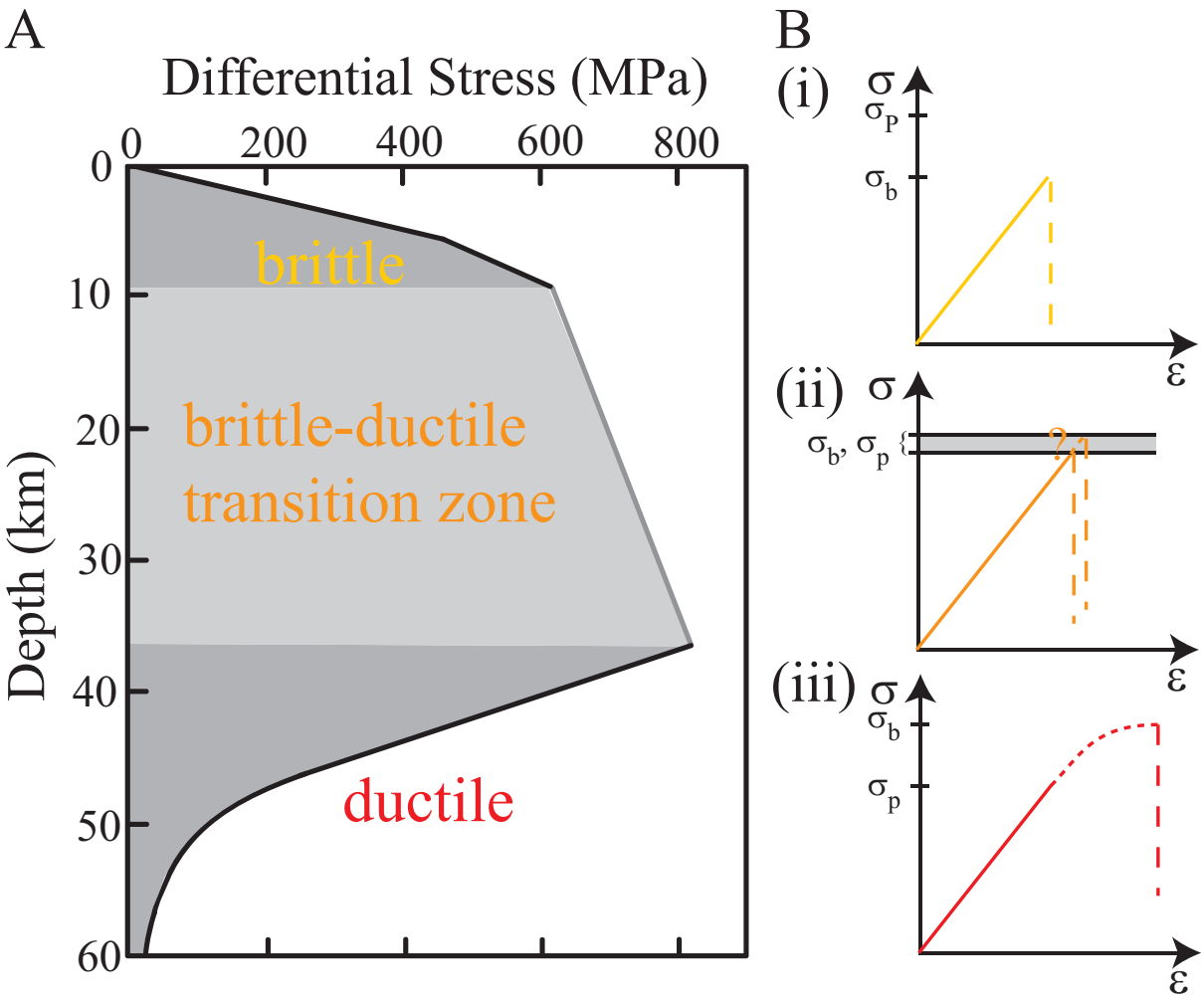

Figure 1.10.: Deformation mechanisms in the Earth's lithosphere. A: modified from *Kohlstedt et al. [1995]*. B: schematic stress-strain relationship in the brittle (i), brittle-ductile transition (ii) and ductile (iii) zones. In the ductile regime, the brittle strength σ_b is higher than the plastic strength σ_p, therefore allowing for plastic deformation to occur. In the brittle regime the rock fractures before plastic deformation may occur, as $\sigma_b < \sigma_p$. In the transition zone both strengths have similar values.

where A is a constant, f_{H_2O} is water fugacity, Φ is the melt fraction, β is a constant, T is the temperature, P is pressure, E^* is the activation energy, V^* is the activation volume and R is the universal gas constant.

A major problem in measuring the viscosity of rocks in the laboratory is the extrapolation from strain rates accessible in the laboratory over several orders of magnitude to strain rates as they actually take place in the mantle. This problem is for example addressed in *Cordier et al. [2012]*, see fig. 1.11. The study shows that a power-law fit for values feasible in the laboratory and a subsequent extrapolation over several orders of magnitude to values relevant for the mantle may lead to large discrepancy between the extrapolated values and the actual values. This shows that the extrapolation of a power-law may not be valid and should be treated with care.

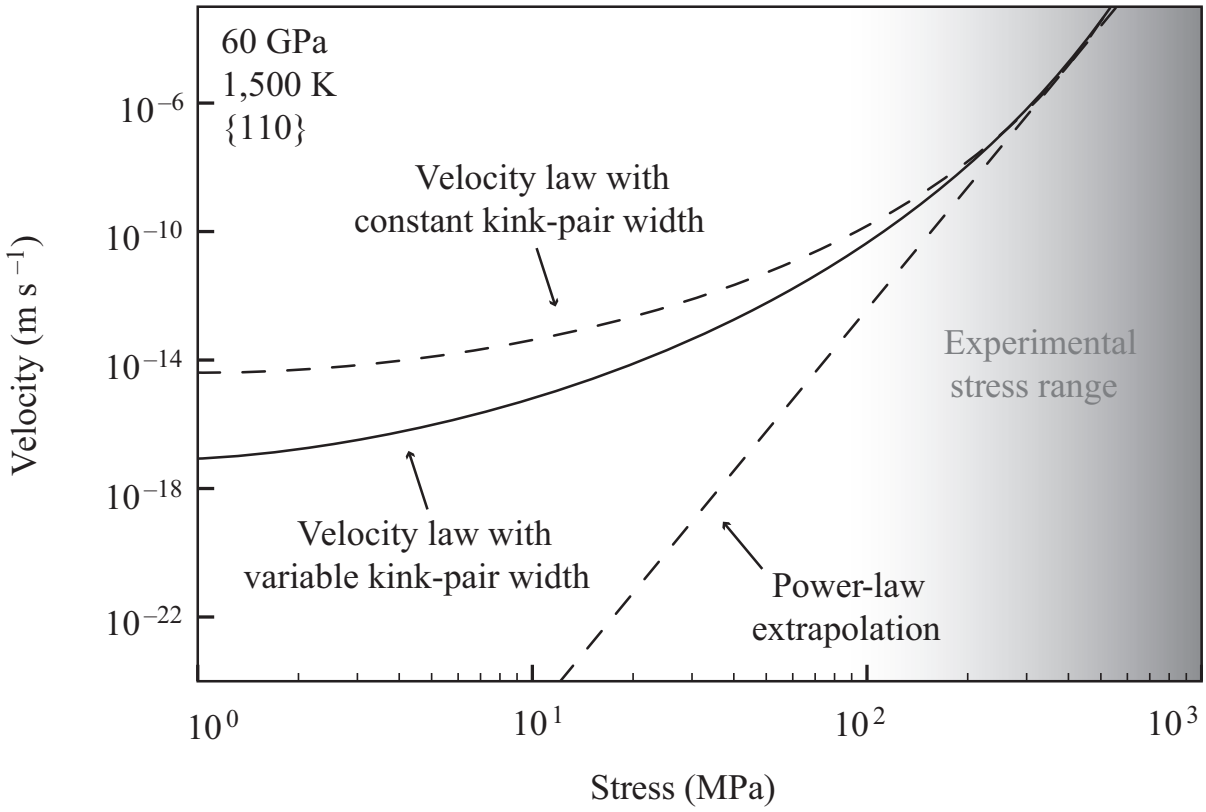

Figure 1.11.: Evolution of the velocity of a dislocation with stress. The power-law fit applied to the range feasible in the laboratory only works in a small range of parameters.

1.3. Thermal Convection

Convection is the motion of a layer of fluid that starts to move due to density-differences. Those density differences can be caused by differences in chemical composition or in temperature. The classical example for thermal convection is the Rayleigh-Bénard Experiment[1], where an infinitely extended fluid in a gravity field between two infinitely extended plates is heated from below and cooled from above, as schematically illustrated in fig. 1.12. Particles near the upper cold wall become denser and tend to sink, while particles near the hot bottom wall decrease their density. The situation is stable as long as i) the buoyancy forces are counterbalanced by the viscous forces acting on a particle while ii) thermal diffusion is larger than momentum diffusivity. Out of equilibrium, less dense particles will rise, while denser particles sink. This motion is called convection.

Fig. 1.13 shows a schematic sketch of the temperature profile that builds up in an isoviscous fluid and a fluid (discussed in section 1.3.2) where the viscosity strongly depends on temperature (discussed in section 1.3.3). In an isoviscous fluid, T_{mean} corresponds to the minimum temperature plus the harmonic mean of the temperature of the two plates. T_{mean} increases as the viscosity contrast Γ, i.e. is the ratio of the viscosity at T_{min} and the viscosity at T_{max}, increases. Hot and cold thermal boundary layers (TBL) have the same thickness in an isoviscous fluid. With increasing Γ the cold TBL grows and becomes significantly thicker than the hot TBL.

1.3.1. Governing Equations and Parameters

Assuming an incompressible fluid in the Boussinesq-approximation (density-differences are neglected everywhere except in the buoyancy-term) the dimensional equations for the conservation of mass, momentum and energy can be written as follows:

$$\nabla \cdot \mathbf{u} = 0 \qquad \text{conservation of mass} \tag{1.16}$$

$$\rho \frac{D\mathbf{u}}{Dt} = -\nabla p + \nabla \cdot \sigma + \alpha \rho \mathbf{g} \boldsymbol{\Delta} \mathbf{T} \mathbf{e_z} \qquad \text{conservation of momentum} \tag{1.17}$$

$$\rho \frac{DT}{Dt} = \kappa \nabla^2 T \qquad \text{conservation of energy} \tag{1.18}$$

where κ is the thermal diffusivity, ρ is the density, α is the thermal diffusivity, $\mathbf{u}$ is the velocity, t is the time, p is the pressure, σ is the stress tensor. The equations can then be non-dimensionalized, to reduce the number of control parameters. Hence the equations become more general as the dimensionalization can be done using different scales. Here we use a length scale d and a characteristical diffusion time to nondimensionalize the time

[1] *Bénard [1901]* reports hexagonally organized convection cells in a layer of walrat heated from below and cooled from above. *Rayleigh [1916]* examined by *"how far the interesting results obtained by Bénard in his careful and skillful experiments can be explained theoretically"*

A

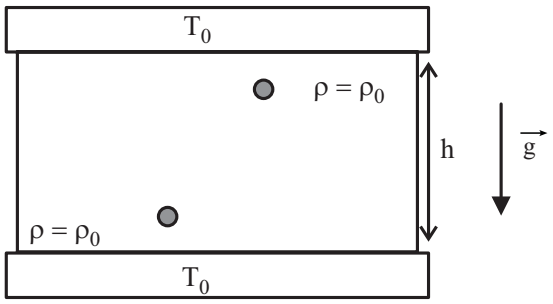

B

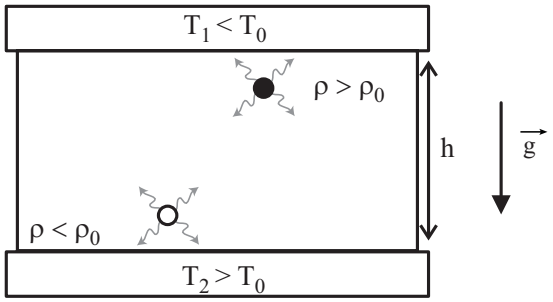

C

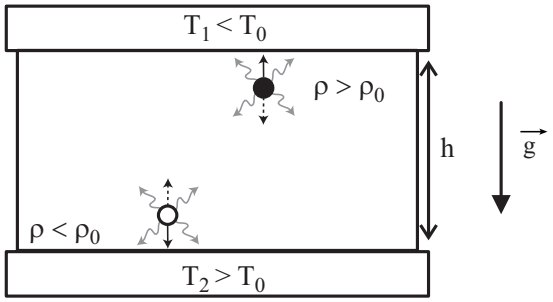

Figure 1.12.: Schematic picture of thermal convection in a constant-viscosity-fluid. A: Initial state, same properties everywhere. B: Heating from below and cooling from above - particle at the bottom (open circle) becomes less dense than particle at the top (black circle). C: Different competing mechanisms acting on particle. Buoyancy (dashed arrow), viscosity (straight arrow) and thermal diffusion (curved arrows).

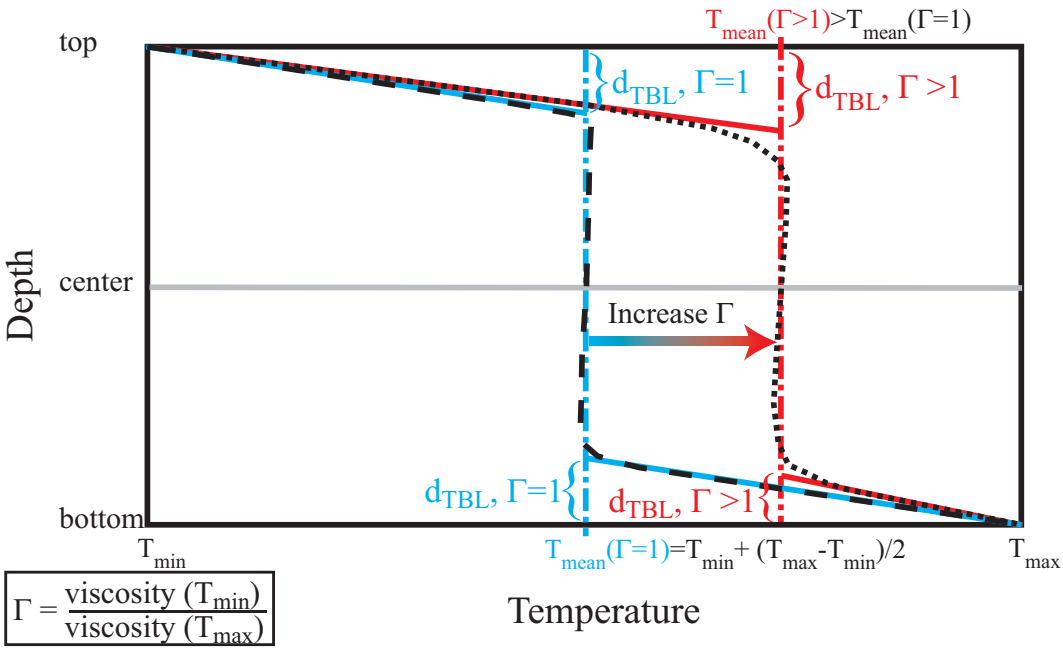

Figure 1.13.: Schematic illustration of the temperature as a function of depth in a box which is cooled from the top at T_{min} and heated from the bottom at T_{max} for two different fluids: isoviscous fluid (black dashed line) and a fluid where the viscosity depends on temperature (black dotted line). Vertical dash-dotted lines indicate the mean temperature T_{mean} for each case. Straight lines show linear approximation of the thermal boundary layer (TBL). The thickness of the TBL (d_{TBL}) is defined as the crossing of linear approximation and mean temperature.

$t' = t\frac{\kappa}{d^2}$. The nondimensional velocity is then written as $\mathbf{u}' = \mathbf{u}\frac{\kappa}{\mathbf{d}}$ and the nondimensional temperature is $T' = \frac{T}{\Delta T}$, where ΔT is the temperature difference between hot and cold plate. Finally the stress may be non-dimensionalized as $\sigma' = \sigma\frac{d^2}{\kappa\eta}$, where η is the viscosity. The equations then write as

$$\nabla \cdot \mathbf{u}' = 0 \qquad \text{conservation of mass} \tag{1.19}$$

$$\frac{1}{Pr}\frac{D\mathbf{u}'}{Dt'} + \nabla p' = \nabla \cdot \sigma' + Ra\, T'\, e_z \qquad \text{conservation of momentum} \tag{1.20}$$

$$\frac{\partial T'}{\partial t'} + \mathbf{u}' \cdot \nabla \mathbf{T}' = \nabla^2 T' + H \qquad \text{conservation of energy} \tag{1.21}$$

Here Pr is the Prandtl-number (explained below), Ra the Rayleigh number (explained below). Rayleigh-Bénard-Convection can generally be characterized as a convection due to temperature-induced density differences. Non-dimensionalizing the basic equations, there are 2 parameters that govern the system.

Prandtl number Pr The Prandtl number describes the ratio of momentum diffusivity (i.e. the kinematic viscosity ν) and thermal diffusivity κ

$$Pr = \frac{\eta}{\rho\kappa} = \frac{\nu}{\kappa} \tag{1.22}$$

where η is the dynamic viscosity and ρ the density. For the Earth Pr is $\mathcal{O}(10^{23})$ so it can be seen as infinite. That means that there is no inertia in the Earth's mantle and implies that a reduction of the driving force (i.e. by decreasing the temperature-difference) below a critical value would result in an instantaneous disrupt of mantle convection.

Grashof number Gr The Grashof number Gr compares buoyancy forces to viscous forces acting on a particle and is therefore defined as

$$Gr = \frac{\alpha\, g\, \Delta T\, h^3}{\nu^2}, \tag{1.23}$$

where α is the thermal expansivity of the fluid, g acceleration due to gravity, h the height of the box and ΔT the temperature difference.

Rayleigh number Ra The product of Grashof and Prandtl number is the Rayleigh number. It therefore represents the ratio of buoyancy forces and forces due to viscous friction in an enviroment where thermal and momentum diffusivity compete. The Rayleigh number is written as

$$Ra = \frac{\alpha\rho\, g\, h^3\, \Delta T}{\kappa\, \eta}. \tag{1.24}$$

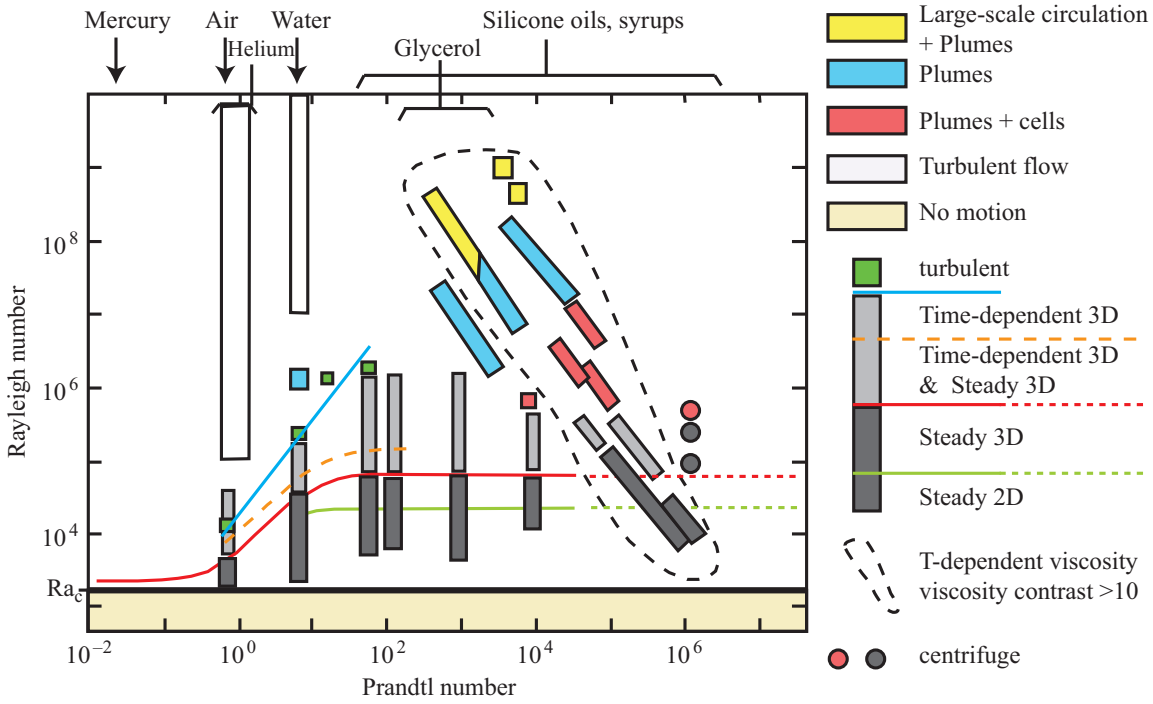

Figure 1.14.: Regime diagram after *Davaille and Limare [2007]*, compiled from *Krishnamurti [1970a,b, 1979]*, *Whitehead Jr. and Parsons [1977]*, *Nataf et al. [1984]*, *Jaupart [1995]*, *Zhang et al. [1997]*, *Manga and Weeraratne [1999]*, *Xi et al. [2004]*, *Nataf et al. [1984]*.

1.3.2. Convection in an Iso-Viscous Fluid

Increasing the Rayleigh number Ra leads to three different regimes. Fig. 1.14 (modified from *Davaille and Limare [2007]*) summarizes the different regimes that can be obtained as a function of Rayleigh and Prandtl number. If the Rayleigh number is below the critical Rayleigh number Ra_c heat is only transported by diffusion. The critical Rayleigh number depends on the boundary conditions. It may therefore range between $Ra_c = 657$ for free-slip boundary conditions and $Ra_c = 1708$ if both boundaries are rigid *Chandrasekhar [1961]*. Above Ra_c the mechanism of heat-diffusion is no longer sufficiently efficient and the fluid starts to organize itself in convecting role-structures. A further increase then leads to a cellular convection and for $Ra > 10^6$ plumes develop and the system is getting more and more time dependent, where turbulence occurs for low $Pr < 100$. The blue line in fig. 1.14 separates the turbulent from the laminar regime.

1.3.3. Convection in a Fluid with Temperature-Dependent Viscosity

Viscosity contrast Γ If the viscosity is temperature-dependent, another dimensionless parameter starts to influence the system - the viscosity contrast

$$\Gamma = \frac{\eta_{cold}}{\eta_{hot}} \tag{1.25}$$

where η_{cold} is the viscosity at the temperature of the cold plate and η_{hot} at the temperature of the hot plate. The temperature dependent viscosity is taken into account in the viscous stress tensor that is written as

$$\sigma = \eta \left(\nabla \mathbf{u} + \nabla \mathbf{u}^{\mathbf{t}} \right). \tag{1.26}$$

Therefore the Navier-Stokes equation for a temperature-dependent viscosity fluid is written as

$$\frac{1}{Pr} \frac{D\mathbf{u}}{Dt} + \nabla p = RaTe_z + \eta' \nabla^2 \mathbf{u} + \frac{\mathbf{d}\eta'}{\mathbf{dt}} \nabla \mathbf{T} \left(\nabla \mathbf{u} + \nabla \mathbf{u}^{\mathbf{t}} \right). \tag{1.27}$$

The case of a temperature-dependent-viscosity has been widely studied (i.e. *Richter [1973]*, *Booker [1976]*, *Nataf and Richter [1982]*, *Richter et al. [1982]*, *Christensen [1984]*, *White [1988]*, *Christensen and Harder [1991]*, *Davaille and Jaupart [1993]*, *Hansen and Yuen [1993]*, *Giannandrea and Christensen [1993]*, *Tackley [1994]*, *Solomatov [1995]*, *Moresi and Solomatov [1995]*, *Tackley [1996]*, *Ratcliff et al. [1997]*, *Solomatov and Moresi [2000]*, *Kameyama and Ogawa [2000]*, *Yoshida and Kageyama [2006]*, *Stemmer et al. [2006]*, *Androvandi et al. [2011]*. Depending on the strength of the temperature-dependence - i.e. the viscosity ratio Γ - different regimes develop (fig. 1.15). It can generally be distinguished between 3 different regimes, as summarized in *Solomatov [1995]*:

(1) Quasi-isoviscous, small Γ ($\Gamma < 2 - 5$)
In case of a low temperature-dependence of the viscosity, the flow generally behaves like convection in a constant-viscosity fluid.

(2) Transient regime, intermediate Γ ($5 < \Gamma < 10^4$)
For an intermediate temperature-dependence of the viscosity, the resistance of motion of the cold TBL due to deformation of the cold TBL becomes comparable to viscous drag of the interior region. *Androvandi et al. [2011]* (fig. 1.15) show that at high Rayleigh number, several hot plumes form inside one cold cell.

(3) Stagnant lid regime, large Γ ($\Gamma > 10^4$)
For a strong temperature-dependence the advective heat transport due to the motion of the cold TBL becomes negligible compared to the much more effective heat transport of

convecting material underneath. A stagnant lid develops, with a linear temperature profile. This big decrease of temperature over a small region leads to an exponential growth of viscosity in the lid. The convection underneath has similar characteristics as isoviscous convection.

The behaviour found in the transient regime (e.g. *Androvandi et al. [2011]*) resembles the behaviour observed on Earth, where several hot plumes form inside one cold cell. However, for Earth-like parameters (e.g. *Karato and Wu [1993]*), convection would fall into the stagnant lid regime. Therefore the question arises: How can this lid be weakened, to localize deformation to subduction zones, where plates sink into the mantle and participate in convection? The answer to this question seems to be a more complex rheology.

1.3.4. Convection with Plate Tectonics - Plastic Yielding

The lack of plate tectonics in convection models with a temperature-dependent viscosity (section 1.3.3) requires a new approach. Numerical models (e.g. *Tackley [2000b]*, *Bercovici [2003]*) show that sufficient strain localization is needed to produce plate-like behaviour. Different approaches are employed to localize deformation, inspired by rock-rheology, cf. section 1.2. Among those approaches are dynamic self-lubrication (*Bercovici [1996]*), grain-size dependent rheology (*Ricard and Bercovici [2003]*) as well as shear heating (*Regenauer-Lieb and Yuen [2000]*, *Kaus and Podladchikov [2006]*, *Crameri and Kaus [2010]*, *Thielmann and Kaus [2012]*). Another way to localize strain is plastic yielding (*Trompert and Hansen [1998]*, *Tackley [2000a]*, *Stein et al. [2004]*). As this mechanism is similar to the rheology of Carbopol where the rheology follows a Herschel-Bulkley law (cf. section 2.4), it is discussed in more detail here.

The models of *Tackley [2000a]* and *Trompert and Hansen [1998]*, *Stein et al. [2004]* employ plastic yielding to weaken the stagnant lid. The same approaches are used in all models of the respective authors (e.g. *Tackley [2000a]*, *van Heck and Tackley [2008, 2011]*, *Rolf and Tackley [2011]* and *Stein and Hansen [2008]*, *Stein et al. [2011, 2013]*).

In the models with plastic yielding, the viscosity consists of a temperature dependent contribution η_T following an Arrhenius-type law and a stress contribution η_E. The effective viscosity is then either taken as the minimum of those two viscosities (e.g. *Tackley [2000a]*) or a mean viscosity is calculated (e.g. *Trompert and Hansen [1998]*, *Stein et al. [2004]*, *van Heck and Tackley [2008]*) as

$$\eta = \frac{2}{\frac{1}{\eta_T} + \frac{1}{\eta_E}} \tag{1.28}$$

which yields viscosity values slightly bigger than the minimum. The viscosity is non-dimensionalized with the viscosity from the Rayleigh-number (cf. *van Heck and Tackley*

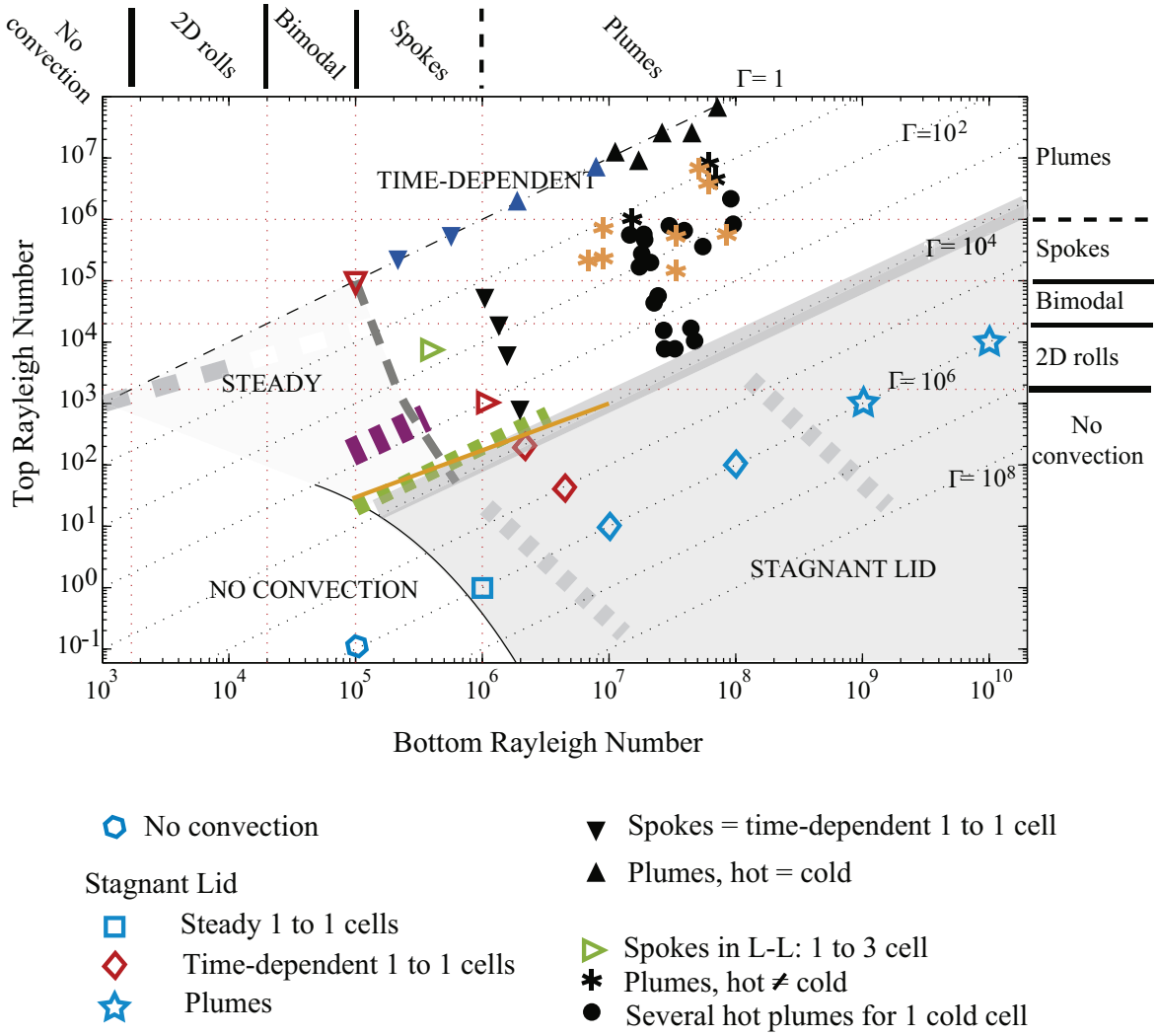

Figure 1.15.: Regime diagram after *Androvandi et al. [2011]*.

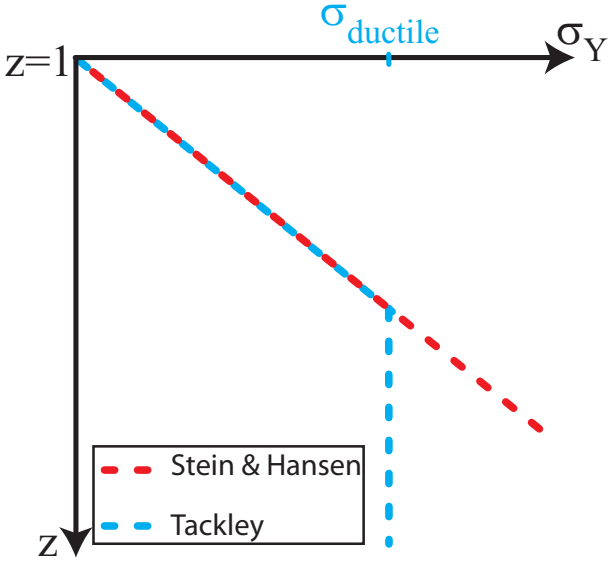

Figure 1.16: Depth dependent yield stress in *Tackley [2000a]* (blue) and *Stein et al. [2004]* (red). In the model of *Tackley [2000a]* the yield stress is set constant, once $\sigma_{ductile}$ is reached.

[2008]). The stress dependent contribution is calculated as a Bingham-type as

$$\eta_E = \eta^* + \frac{\sigma_Y(z)}{\dot{\gamma}} \tag{1.29}$$

with a plastic viscosity $\eta^* = 10^{-5}$ in the models of *Stein et al. [2004]*, where this value was leading to the best plate-like behaviour. The viscosity is normalized by the surface viscosity. In the model of *Tackley [2000a]* the plastic viscosity is equal to zero and the stress dependent viscosity here is written as

$$\eta_E = \frac{\sigma_Y(z)}{2\,\dot{\gamma}} \tag{1.30}$$

The depth dependence of the yield stress that we have seen in fig. 1.10A is mimicked in the numerical simulations using Byerlee's law where the yield stress is defined as

$$\sigma_Y = \sigma_{0n} + \sigma_{brittle}(1 - z) \tag{1.31}$$

where σ_{0n} is zero in *Tackley [2000a]* and takes values between 2 and 13 in *Stein et al. [2004]*. *Tackley [2000a]* then calculates the yield stress as the minimum of σ_Y and $\sigma_{ductile}$ (the upper stress limit for ductile deformation). Hence fig. 1.16 shows that the yield stress increases with depth until $\sigma_{ductile}$ is reached.

While *Tackley [2000a]* uses an upper cutoff to avoid infinite viscosities at vanishing shear rates, *Trompert and Hansen [1998]* reference the biviscosity approach used by *Burgess and Wilson [1996]*, which is generally doing the same as an upper cutoff does, i.e. replacing the theoretically infinite viscosity at vanishing shear rate with a finite viscosity value. The

resulting rheological laws are shown in fig. 1.17, depending on the strain rate. The yield stress is set to 200 MPa. If the lower cut-off in the model of *Tackley [2000a]* is chosen as the same value as η^* in the model of *Stein et al. [2004]* the rheology behaves similar at high strain rates ($\eta^* = 10^{16}$ Pa s in fig. 1.17). If the upper cut-off in *Tackley [2000a]* is chosen to be the same as the upper viscosity in the bi-viscosity approach of *Stein et al. [2004]*, the models behave the same way at low shear rates. With a lower (cut-off) viscosity of 10^{16} Pa s (e.g. $\eta_{max} = 10^{25}$ Pa s in fig. 1.17). The Herschel-Bulkley model is shown for comparison, to illustrate that the different rheological laws are not that much different with the proper parameter-choice ($\sigma_0 = 200$ MPa, $K_\nu = 0.01\,\eta^*$, $n = 0.6$). Even though all three rheologies look different at first glance, they may describe the same, or at least a similar behaviour.

Two important characteristics of plates are the plateness and the poloidal-toroidal ratio.

Plateness: The deformation of the surface can be calculated by regarding the square-root of the second invariant of the strain-rate-tensor, which should be zero where there is no surface deformation, i.e. in the middle of plates and should approach one at plate margins. As there is also deformation within the plate, regions where the deformation is equal or less than 20% of the maximum surface deformation are still regarded as plates, see for example *Tackley [2000a]*, *Stein et al. [2004]*.

Poloidal-Toroidal-Ratio: A 3D- flow field can be divided into a poloidal and a toroidal component. The poloidal component describes convergent or divergent flow and is generated by buoyancy forces. Applied to the earth, poloidal flow is represented by subduction zones or spreading centres. A toroidal component describes strike-slip-motion and can be generated on earth i.e. by the rotation of a plate or transform faults. The ratio of these two components for the velocity field of earth's plate tectonics is between 0.25 and 0.5.

Depending on the yield stress and the viscosity contrast, *Stein et al. [2004]* observe different regimes (fig. 1.18). At high yield stresses and high viscosity contrasts the system stays in the *stagnant lid regime*. Lowering the yield stress, and intermittent *episodic regime* occurs, which would be a possibility to explain the episodic resurfacing observed on Venus. A more Earth-like behaviour, the *mobile lid regime* may develop for low viscosity contrasts at all yield stresses, whereby the yield stress allowing for the mobile lid regime decreases as the viscosity contrast increases.

These models are typically showing plate-like behaviour for a yield-stress range of 100 to 300 MPa, which is below the yield stress of about 700 MPa estimated from the observations of *Kohlstedt et al. [1995]*. A major drawback of those models is that (i) the above mentioned poloidal-toroidal ratio of those models does not match the observed ratio on Earth. However *van Heck and Tackley [2008]* could show that this strongly improves when using a spherical instead of a cartesian geometry. Advancement has recently been made by adressing problem (ii), that subduction is always two-sided in the models, which is contradicting the one-sided subduction that is observed on Earth. *Rolf and Tackley [2011]* introduce continents into the numerical simulation, which are focusing the stress,

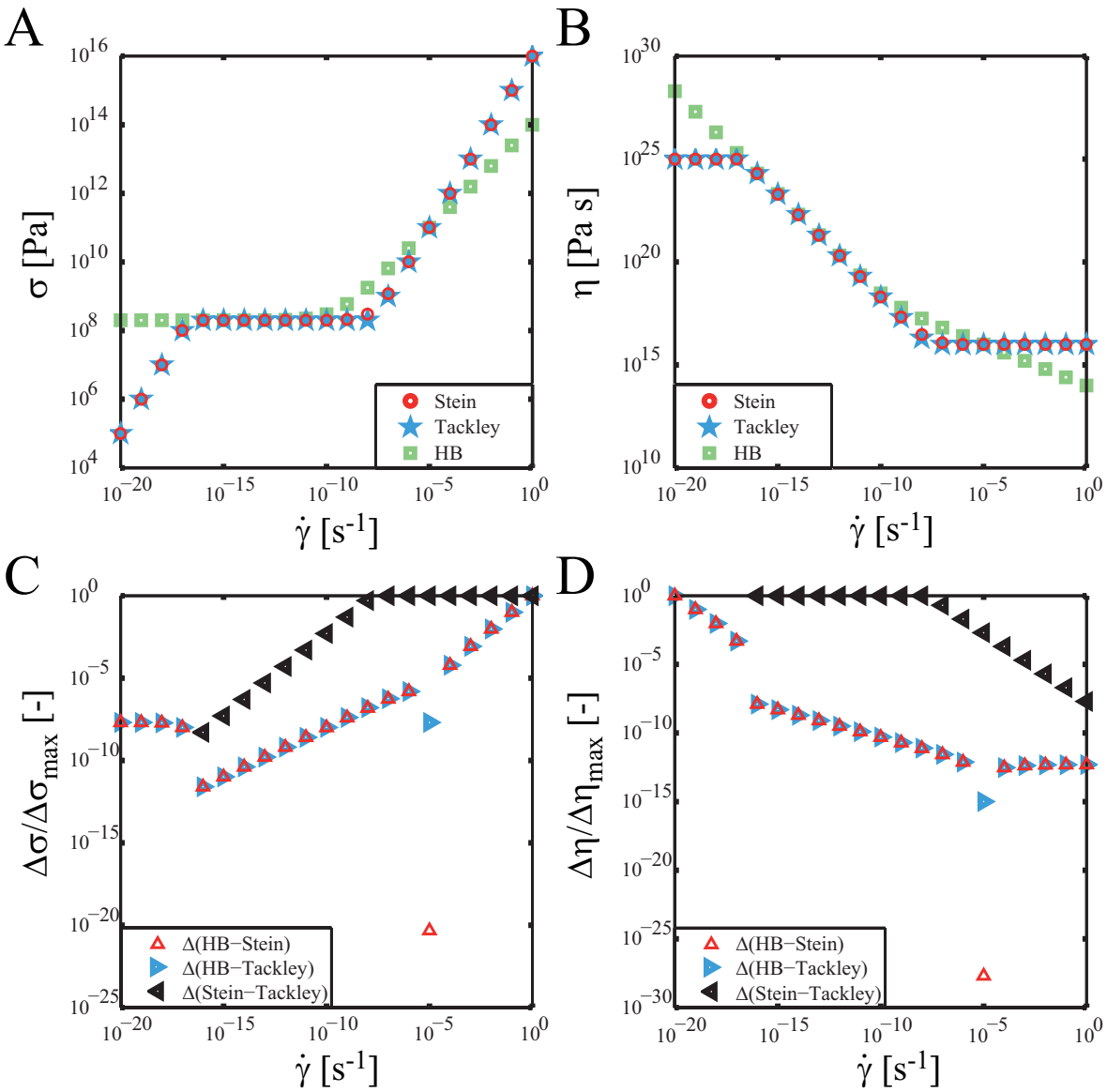

Figure 1.17.: Comparison of different rheological laws for a yield stress $\sigma_{0,y} = 200\,\mathrm{MPa}$. A and B show the stress and the viscosity respectively. Blue stars: *Tackley [2000a]*, red circles: *Stein et al. [2004]* and green boxes Herschel-Bulkley model (eq. 2.4). C and D show the differences between the models, normalized by the maximum difference. Red triangles show the difference between the Heschel-Bulkley model and the model employed by *Stein et al. [2004]*, blue triangles pointing to the right show the difference between the Herschel-Bulkley model and the model employed by *Tackley [2000a]* and black triangles pointing to the left show the difference between the models of *Tackley [2000a]* and *Stein et al. [2004]*.

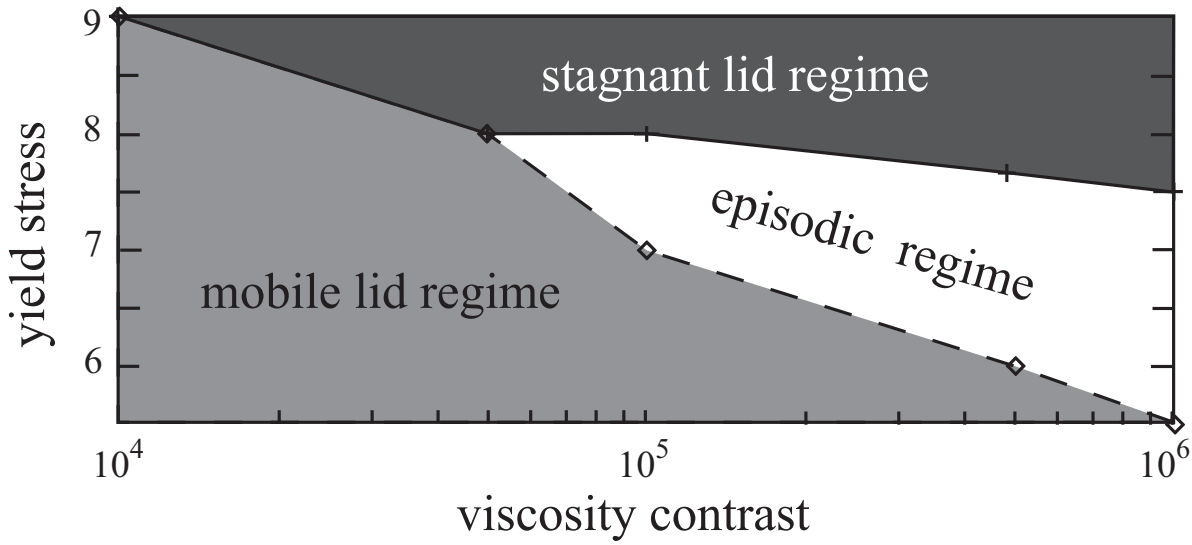

Figure 1.18.: Different regimes evolving depending on the non dimensional yield stress and the viscosity contrast, modified from *Stein et al. [2004]*. The non dimensional yield stress is written as $\sigma_Y = d^2\sigma_{dim}/\eta_0\kappa$, *Stein et al. [2013]*, where η_0 is the viscosity used to calculate the Rayleigh number.

due to the heterogeneity introduced by the continents, and lead to one-sided convection beneath continents. However this model still does not explain how oceanic subduction zones work, i.e. where oceanic lithosphere subducts beneath oceanic lithosphere. Employing the sticky air method that allows for a deformation of the crust by adding a "stick" very viscous "air" at the surface, that usually has a viscosity of only a few orders of magnitude lower than the crust (*Schmeling et al. [2008]*), *Crameri et al. [2012]* obtain one-sided subduction of oceanic lithosphere. A free deformable surface is therefore a key ingredient.

1.3.5. Convection in a Fluid with Complex Rheology

Despite its importance for planetary bodies, only few studies deal with convection in yield stress fluids (*Zhang et al. [1997, 2006]*, *Vikhansky [2009, 2010, 2011]*, *Turan et al. [2010, 2012]*, *Balmforth and Rust [2009]*, *Davaille et al. [2013]*, *Darbouli et al. [2013]*). From a theoretical point of view, the difficulty is that an instability cannot develop from a conductive profile submitted to infinitesimal perturbation *Zhang et al. [2006]*, *Vikhansky [2009]*. The combination of yield stress and shear thinning fluids is hardly studied, as either a Bingham fluid is used (*Zhang et al. [1997]*, *Vikhansky [2010, 2011]*, *Turan et al. [2010, 2012]*), or a shear thinning fluid, that does not exhibit a yield stress *Barr et al. [2004]*, *Solomatov and Barr [2006]*. Convection in a fluid that presents weak shear

thinning effects and a yield stress has been studied by *Balmforth and Rust [2009]*. They conclude, that shear thinning favours convection, while a yield stress suppresses convection.

In a study that had started prior to my arrival at FAST, B. Gueslin and A. Davaille have performed laboratory experiments on the existence and morphology of thermal plumes in a yield stress fluid (*Davaille et al. [2013]*, appendix A.1). The fluid used is Carbopol, a visco-elastic fluid, its rheology can be described by a Herschel-Bulkley model (e.g. *Divoux et al. [2011]*). A localized heat source is employed, consisting of a Peltier-element with copper plate on its top, placed in the centre of a square plexiglas tank. In this study we define a yield parameter, comparing the stresses due to the buoyancy of the fluid to the yield stress. Therefore the yield parameter is written as

$$Y_0 = \frac{\alpha \rho g P}{k \sigma_0}, \tag{1.32}$$

where P is the thermal power of the heat source and k is the thermal conductivity. A systematical variation of the supplied heat and the rheological properties of the fluids shows that depending on Y_0, three different regimes may be observed (fig. 1.19). For $Y_0 < Y_{c1} = 120$ the fluid does not move. For a further increase of Y_0 ($Y_{c1} < Y_0 < Y_{c2} = 260$) a small cell forms that convects around the heater (fig. 1.20)A. For $Y_0 > Y_{c2}$ a plume develops (fig. 1.20)B. The morphology of this plume differs from the mushroom-shape typically encountered in Newtonian fluids (fig. 1.21), and is therefore referred to as a finger-like shape. Inside the thermal anomaly, the velocity field is rather flat, and resembles a plug flow. For small consistencies, an episodic behaviour may be observed (fig. 1.20C). The plume rises fast, then halts and then rises in a second pulse to the surface.

Similar results for the onset of convection are found in a recent study by *Darbouli et al. [2013]*, who investigate Rayleigh-Bénard convection in Carbopol in a circular box. They define a generalized Rayleigh number, which is similar to the yield parameter (eq. 4.2) and is written as

$$Ra_g = \frac{\alpha \rho g \Delta T d}{\sigma_0}, \tag{1.33}$$

where d is the height of the box. Notably, different from the classical notation of the Rayleigh number (eq. 1.24), Ra_g is linear with d (and not cubic). *Darbouli et al. [2013]* find a critical value for the onset of convection which is $Ra_{gc} = 40$ for free-slip boundary conditions and $Ra_{gc} = 80$ for no-slip conditions.

1.4. This Study

The previous section has shown, that two ingredients are needed to produce plate tectonics in a self-consistent manner:

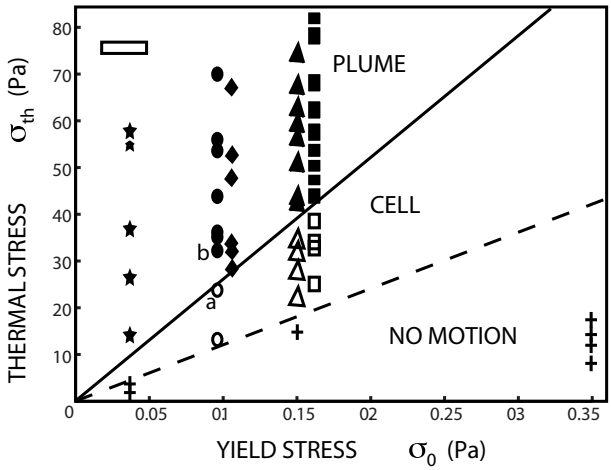

Figure 1.19.: From *Davaille et al. [2013]*. Phase diagram as a function of the yield stress σ_0 and of the stress of thermal origin σ_{th}. Filled symbols stand for the plumes, empty ones for convection confined around the heater, and crosses for no convection. The solid line represents $Y_{c2} = 260$ and the dotted line $Y_{c1} = 120$. Different symbols represent different fluids. The empty black rectangle in the top left corner shows the uncertainty on the stresses. "a" points toward an experiment without any plume even after four days while experiment "b" generated a plume in less than 30 min.

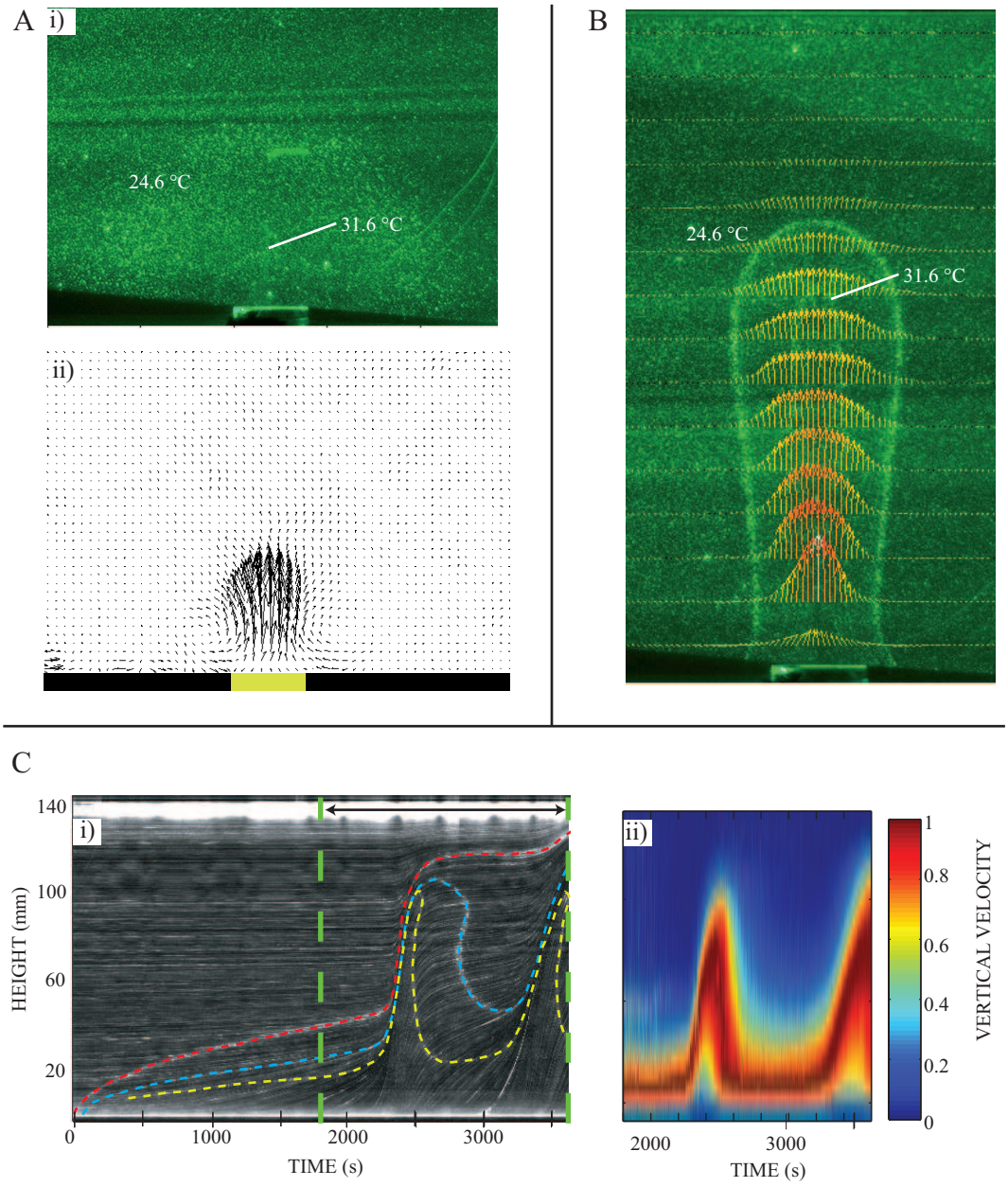

Figure 1.20.: Modified from *Davaille et al. [2013]*. A: isotherms (i) and velocity (ii) for a cell regime. B isotherms and velocity field for the plume regime. C: (i) spatiotemporal evolution of a vertial pixel-line at the plume axis through time. Different colors highlight different isotherms (red: 24.6 °C, blue: 31.5 °C, yellow: 39.5 °C). (ii) velocity at the plume axis, normalized by the maximum velocity, corresponding to the region indicated by the arrow in C(i).

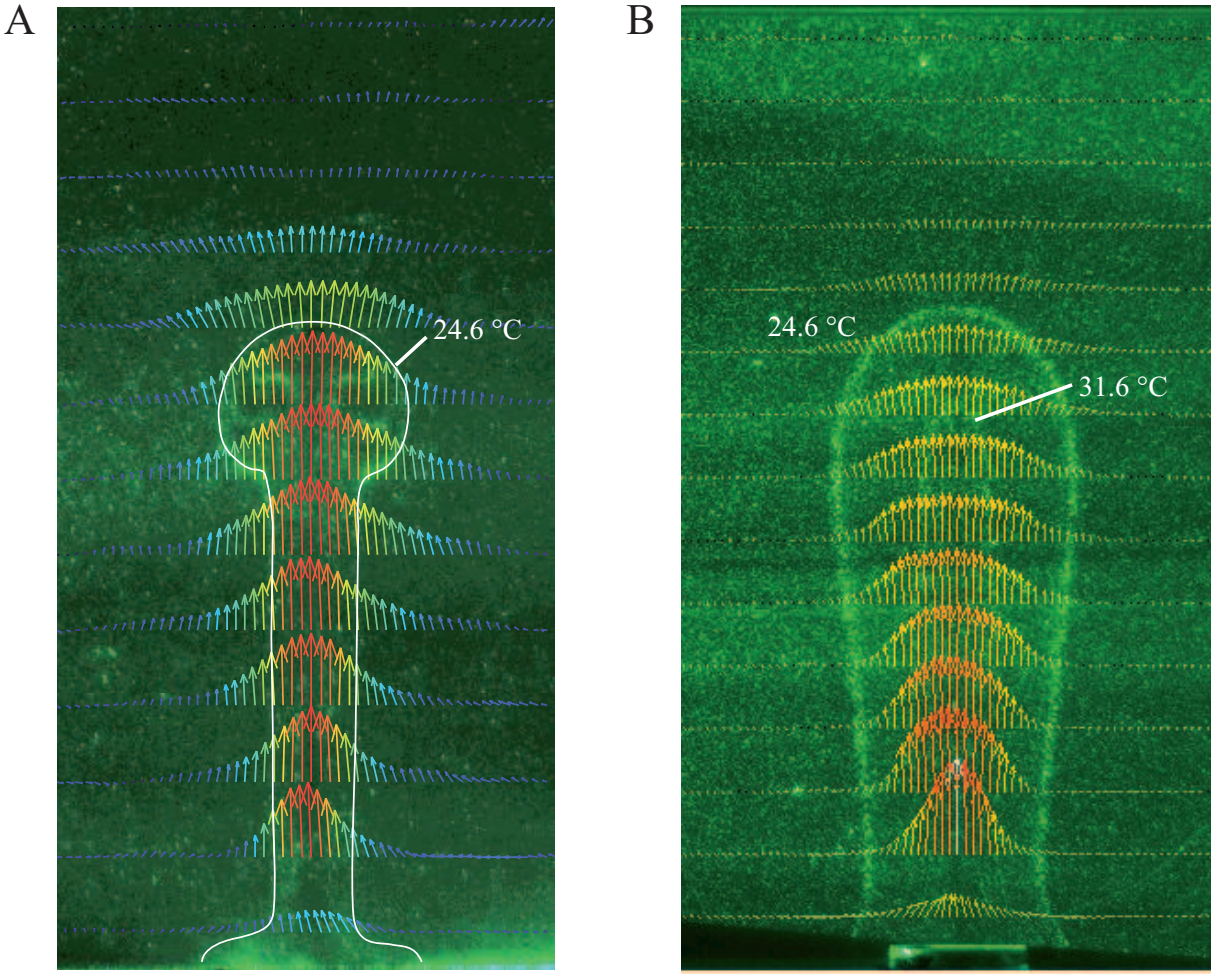

Figure 1.21.: A: Thermal structure and velocity field of a hot instabilitiy in a Newtonian Fluid (sugar syrup, image courtesy of Floriane Touitou) versus B: hot instability in Carbopol (modified from *Davaille et al. [2013]*). Note the mushroom-like structure of the instabilitiy in the Newtonian fluid and the evry smooth velocity field, compared to the finger-like shape of the instability in Carbopol, with a flat velocity field inside the instability and strong gradients of the velocity towards its edges.

- temperature dependent viscosity, whereby the cold thermal boundary layer forms a stiff plate
- a weakening mechanism, which allows to localize the deformation within the cold plate. As a consequence the plate breaks and sinks into the mantle.

The characterization of convection in fluids with temperature dependent viscosity has largely been studied (cf. sec. 1.3.3). In contrast the knowledge about convection in a fluid that presents a yield stress and is shear thinning is sparse. Only two recent studies (*Davaille et al. [2013]*, *Darbouli et al. [2013]*) deal with systematic experiments with convection in a yield stress fluid and characterize the onset and the dynamics. However several questions remain open. The episodic behaviour of the plume, where the plume reaches the surface in a second pulse (*Davaille et al. [2013]*) opens the question whether a plume would need more pulses to reach the surface, if the height of the fluid was increased. In order to study the influence on the dynamics of the plume, I have performed a series of experiments with different fluid heights (chapter 3). Another interesting question is, whether the Herschel-Bulkley model provides a suitable description of the fluid. Hence, I performed numerical simulations to compare to the laboratory results and to identify the relevant mechanisms that are responsible for the emplacement of the instability (chapter 4). The advantage of the numerical simulation is furthermore to avoid the large error on the measurement of the yield stress (cf. fig. 1.19). In chapter 5, I focus on the steady-state characteristics of the plume. Finally, in chapter 6, we shall go back to the Earth. Here I show that the existence of intrusions in the lithosphere or in the mantle, can give us precious constraints on the rheology of the matrix into which those instabilities where emplaced.

2. Setup and Fluid

2.1. Setup and Heating

The setup consists of a plexiglass tank (cf. fig. 2.1) with a ground surface of $20 \times 20\,\mathrm{cm}^2$ which is 50 cm high with a free surface. The heater is placed in the center of the bottom of the tank and consists of a Peltier-element, which is put with the cold side on top of an aluminium plate. On top of the hot side, a copper disk is placed, to uniformly distribute the heat. The heating is embedded into a plexiglass plate, to avoid heat loss towards the sides and to provide clean boundary conditions for the comparison with numerical simulations. Thermocouples measure the temperature below the Peltier-element and inside the copper disk. The Peltier element is operated at constant electrical power. Voltage, current and power are measured every five seconds. The thermal power emitted by the hot side of the Peltier-element is calculated as follows (*Davaille et al. [2013]*)

$$P = S_P I T_h + \frac{1}{2} R_P I^2 - k_P (T_h - T_c) \tag{2.1}$$

where S_p is the Seebeck-coefficient, I the current, T_h is the temperature measured in the copper plate, T_c the temperature measured at the cold side of the Peltier element, R_p is the electrical resistance of the Peltier element and k_P its thermal conductivity. The accuracy of the thermal power is $\approx 10\,\%$ for an uncertainty in temperature of 0.1 K.

Table 2.1.: N: number of semi conductors, G ratio of surface to height of one semi conductor, κ_{sc} thermal conductivity of one semi conductor, h_P is the height of the Peltier element, l_P the length of its sides, h_{Cu} is the height of the copper plate and d_{Cu} its diameter.

N	G	κ_{sc}	h_P	l_P	h_{Cu}	d_{Cu}
-	-	W/mK	mm	mm	mm	mm
34	0.1633	1.33×10^{-2}	1.4	15	3.36 ± 0.05	25.1 ± 0.1

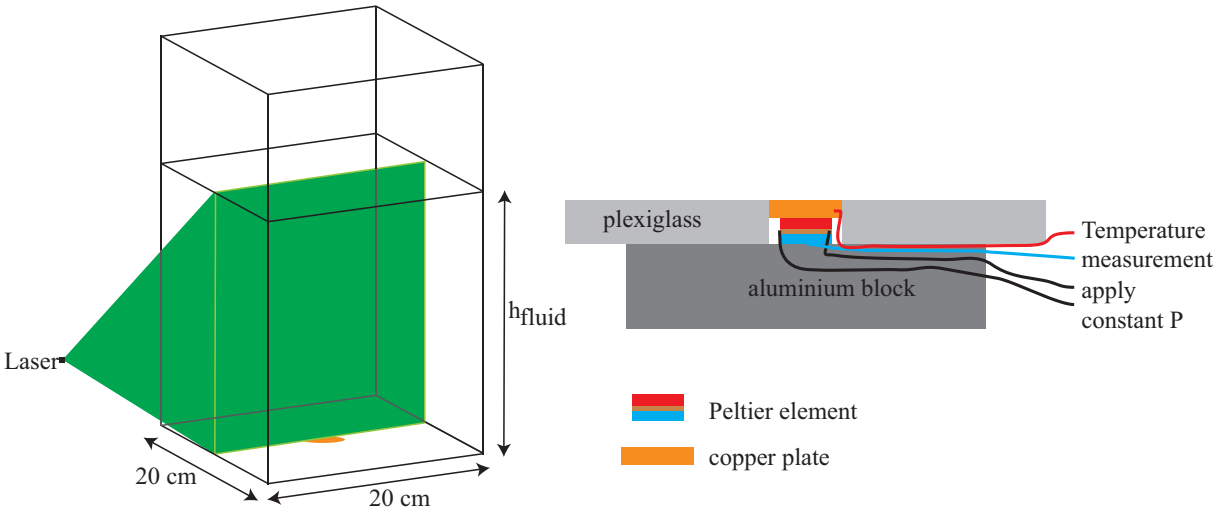

Figure 2.1.: Setup used during the experiments. The total height of the tank is 50 *cm*, the ground surface is $20 \times 20\,\mathrm{cm}^2$. The heater consists of a Peltier element, placed on a 2 cm thick aluminium block. On top of the Peltier element a copper disk is placed to uniformly distribute the heat, both are embedded into a plexiglass plate. Thermocouples measure the temperature below the Peltier element and inside the copper disk. Specifications of the copper plate and the Peltier element are given in table 2.1.

Table 2.2.: Values obtained from calibration of TLC illuminated with a laser of wavelength $\lambda = 532\,\text{nm}$. Series 1 is used for experiments with CBP5-6 and the Rayleigh-Bénard setup described in appendix 2.2.3, Series 2 is used for experiments with CBP8-14.

Series 1	T [°C]	Series 2	T [°C]
BM/24C2W/S40	23.9 ± 0.26	SLN40/R24C2W	23.40 ± 0.27
BM/27C10W/S40	27.1 ± 0.30	SLN40/R27C2W	26.60 ± 0.37
BM/31C2W/S40	31.1 ± 0.26	SLN40/R30C2W	29.60 ± 0.21
BM/35C10W/S40	35.1 ± 0.30	SLN40/R33C2W	32.86 ± 0.25
BM/40C2W/S40	39.9 ± 0.39	SLN40/R37C2W	36.55 ± 0.34

2.2. Data Acquisition

2.2.1. PIV: Particle Image Velocimetry

The fluid is seeded with small spheres (Glass Hollow Spheres 110P8 from LaVision), which reflect the laser light. Images are recorded every Δt. To calculate the velocity field, the PIV (particle image velocimetry) software DaVis 7.2 from LaVision is used. The image is divided with a grid into several windows. In each grid-window, the position of the intensity maximum of a group of particles is compared between two subsequent images. The displacement field (in pixels) can then be calculated via cross correlation and can then be converted into m/s by knowing how many pixels correspond to which distance and knowing Δt. The accuracy in distance is in the sub-millimetre range.

2.2.2. TLC: Thermochromic Liquid Crystals

To visualize the temperature field we use thermochromic-liquid-crystals (TLC) from hallcrest. To protect them, the liquid crystals are encapsulated. They have a diameter of 10 to 40 μm. TLC reflect the light of a certain wavelength at a certain temperature. If illuminated with white light they therefore show different colors, depending on the temperature of the fluid. We are illuminating the setup with a laser with a wavelength of $\lambda = 532\,\text{nm}$. Hence one type of TLC reflects this light at a given temperature and therefore highlights one isotherm. More details on this method are given in *Davaille and Limare [2007]*. The TLCs have been calibrated imposing a stable temperature gradient, the values are given in table 2.2. For convenience, the temperature reflected by each type of TLCs will be referred to as the $[24, 27, 31, 35, 39]\,°$C-isotherm for Series 1 and $[23, 26, 29, 32, 36]\,°$C-isotherm for Series 2.

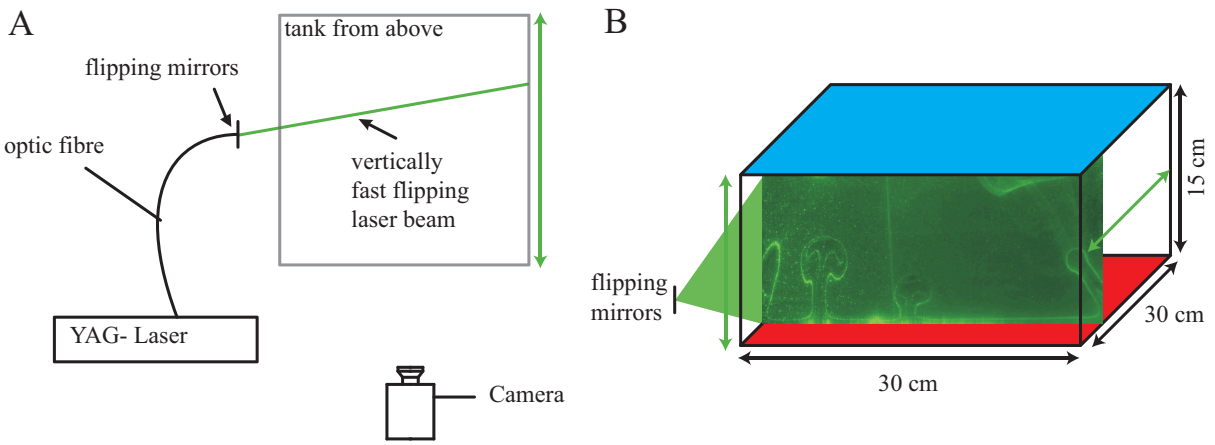

Figure 2.2.: A: setup from above. The laser-beam arrives via an optic fibre on two flipping mirrors: one vertically fast flipping, one slowly horizontally flipping, creating a vertical laser sheet that is horizontally displaced, scanning the tank. Images are recorded with a camera. B: schema of the setup, the box is heated from below and cooled from above. Image results from fast vertically flipping laser beam, images are taken all over the box.

2.2.3. Development of a 3D Isotherm Visualization Method

To get familiar with the experimental techniques I have developped a 3D isotherm visualization method for the Rayleigh-Bénard experiment, at the beginning of my thesis project. Therefore the tank is scanned with a laser sheet. The setup (fig. 2.2) consists of a laser beam directed with an optical fibre onto two mirrors. The vertically fast flipping mirror creates the laser sheet, flipping at frequency $100\,\mathrm{Hz} < f < 1000\,\mathrm{Hz}$). The horizontally slow flipping mirror is then used to the tank. Good results are obtained for 40 images over the 30 cm long box, over two seconds, as the frame rate of the camera (*Image ELite* by LaVision) is limited to $10 - 12$ images per second.

The idea of the developed method is to first isolate the brightest isotherm of each picture (which corresponds to different depths inside the tank) and then to reconstruct a surface of the brightest isotherm. One problem of this method is, that it is important to get rid of strong reflections to avoid to reconstruct those reflections instead of or in addition to the isotherm. Therefore it is important to have a good synchronization of the mirror that moves the laser sheet and the camera, because then it is possible to subtract the first picture and to get rid of reflections on the boundaries of the box. In a next step a median filter is used to get rid of the so called “salt-and-pepper-noise” due to the spherical particles used for PIV. Then a Gaussian filter is applied to smooth the image. Afterwards the gradient is calculated. As the intensity is highest in the middle of an

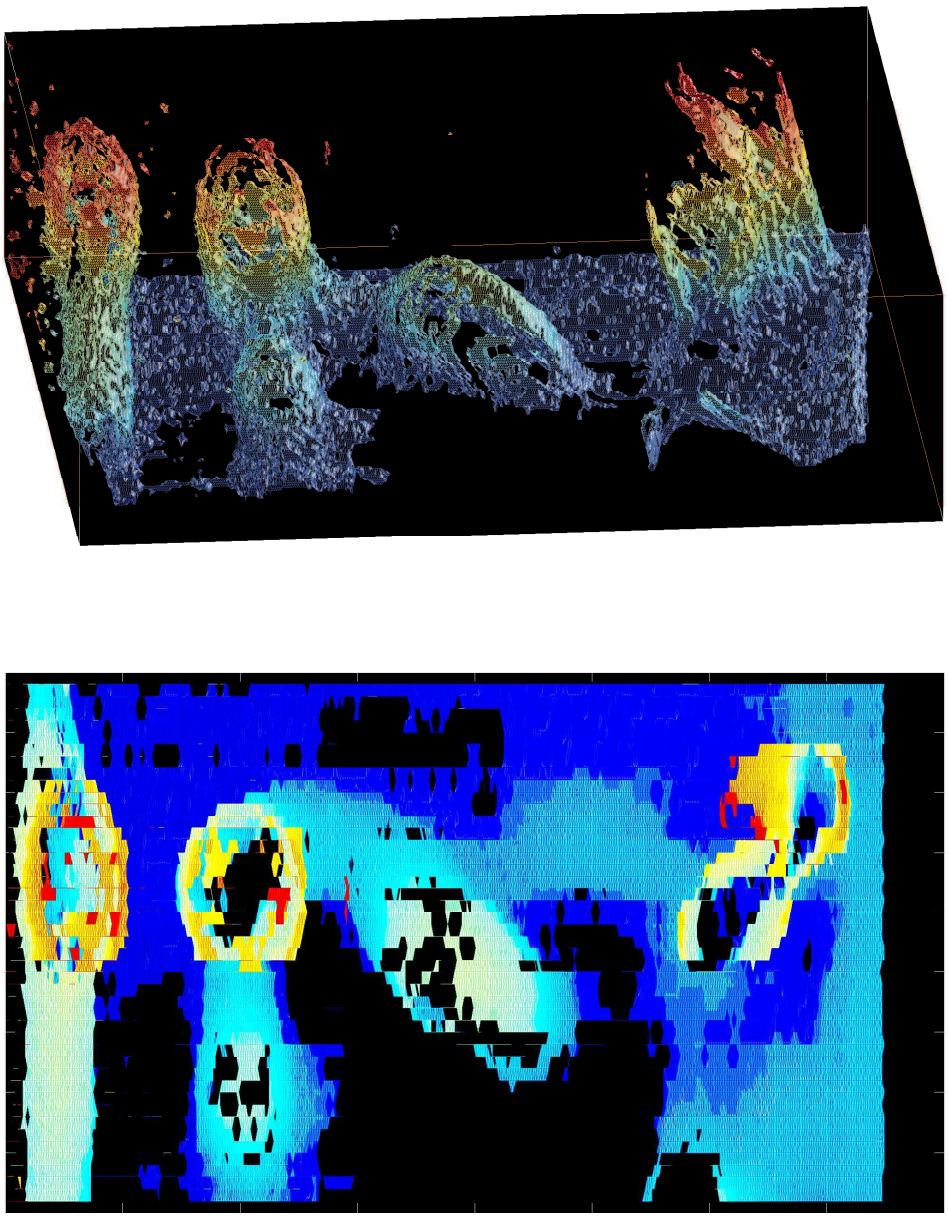

Figure 2.3.: First 3D-picture-results. Dark blue represents the bottom of the box whereas dark red represents a height of 15 cm. *Upper*: view from 45°, *lower*: view from above. 44 pictures were taken for the reconstruction.

isotherm, the gradient is pointing "away" from these points where it is approximately zero. As the gradient is also zero where there is no intensity at all, it is not sufficient to use the gradient as the only criteria to identify an isotherm. Therefore it is used in combination with a threshold-value for the intensity. If the criterion is fulfilled, the program writes a *zero* on a place in a matrix corresponding to the position of the considered point, otherwise it writes a *one*. This procedure is repeated for each picture, then patch and isosurface are used to reconstruct an isosurface of all those values which are *zero*. To get a better idea of the height, this isosurface can then also be color coded, cf. fig. 2.3. The method is summarized in appendix B.1.

2.3. Numerical Simulation

The physical model is based on the assumption of conservation of mass, momentum and energy. The set of equations (1.16-1.18) is discretized using a finite volume method on a staggered grid and solved with an iterative multigrid method, implemented in the code StagYY. Code details and benchmarking for constant viscosity and temperature-dependent viscosity cases are described in detail in *Tackley [1994, 2008]* (*Tackley [1994]* pp. 286-290 for benchmarking results). For the diffusive term, second order finite differences are used, and a second order upwind scheme is used for the advective terms. The convergence criterion is met, if the normalized residuals of the momentum and continuity equations is smaller than 10^{-2}. In the staggered grid method, scalar variables, such as pressure or temperature, are defined at the cell centre, while the velocity is located at the faces of the cells (fig. 2.4). More details on the code and the employed rheological law are given in chapter 4.

2.4. Thermal and Rheological Properties of Carbopol

Carbopol is a powder that consists of micron-size particles. If diluted in water those particles swell. The pH of this solution is (for 0.6 g/l in distilled water) around $pH = 3.5$ and therefore acidic. Adding NaOH to the mixture leads to an extensive swelling of the particles up to 10-1000 times in volume (*Lee et al. [2011], Oppong and de Bruyn [2011]*). The neutralized solution forms a transparent, stable gel ((*Piau [2007]*)) and is therefore ideal for the visualization techniques used in this study.

2.4.1. Flow Test

The rheology of the fluid was determined by using a Physica MCR501-rheometer (Anton Paar, www.anton-paar.com) with a coaxial cylinder geometry (CC27, cf. fig. 2.5). The measuring bob diameter is 26.664 mm, the measuring cup diameter 28.32 mm and

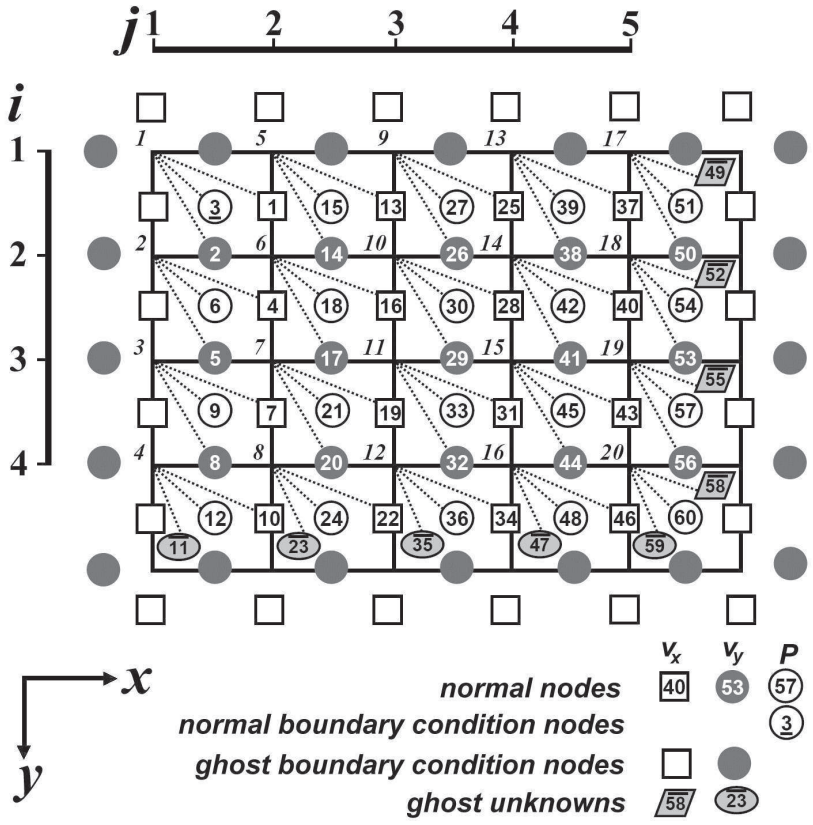

Figure 2.4.: Schematic illustration of a staggered grid, from *Gerya [2010]*. Scalar variables (pressure P) are located at the center of each cell, the velocity is defined at the cell faces.

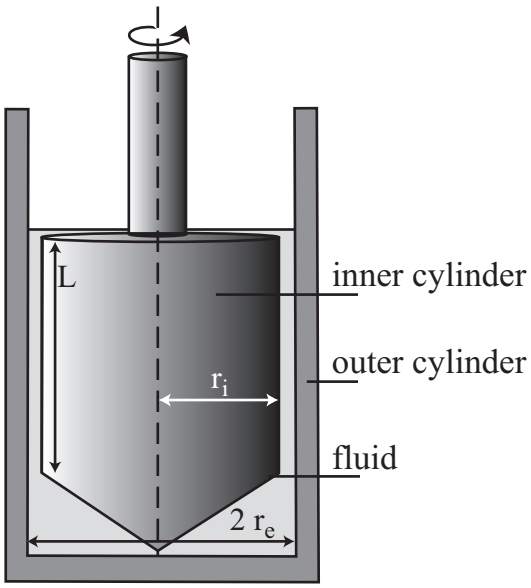

Figure 2.5: Schematic picture of the Couette-geometry used to determine the rheological properties. L is the gap length, d_b the bob diameter and d_c the cup diameter.

the gap length is 40 mm. The geometry is temperature-controlled by a Peltier element and maintained at $T = 20\,°\mathrm{C}$. To prevent evaporation we used a solvent trap. To avoid wall slip effects at the inner cone (Roberts and Barnes [2001], Divoux et al. [2010]), we used very fine sandpaper (i.e. 50 μm average grit size).

2.4.1.1. Measurements with Sandpaper

The sandpaper increases the bob diameter to 27.23 mm, which has to be taken into account. How the stress can be calculated from the torque measured in the rheometer is for example described in *Macosko [1994]*. The stress is calculated as follows

$$\sigma = \frac{1+\delta^2}{2000\,\delta^2}\,\frac{M}{2\pi\,L\,r_i^2\,C_L}, \tag{2.2}$$

where δ is the ratio of the radius of the cup (r_e) and the bob (r_i), M is the torque measured by the rheometer, L is the length of the cone and C_L is a correction factor. The shear rate then is calculated as follows

$$\dot{\gamma} = \pi\,\frac{n_v}{30}\,\frac{1+\delta^2}{\delta^2-1} \tag{2.3}$$

where n_v is the speed measured in 1/min. The other values are $L = 39.999\,\mathrm{mm}$ and $C_L = 1.1$. To validate the applicability of the sandpaper and the corrective calculations, measurements on glycerol have been performed, whose viscosity is $\eta = 1.412\,\mathrm{Pa\,s}$ for pure glycerol (*Segur and Oberstar [1951]*). The measurements (fig. 2.6) show good agreement between the measurements that haven been done without and with the sandpaper and fall on the value of $\eta = 1.412\,\mathrm{Pa\,s}$.

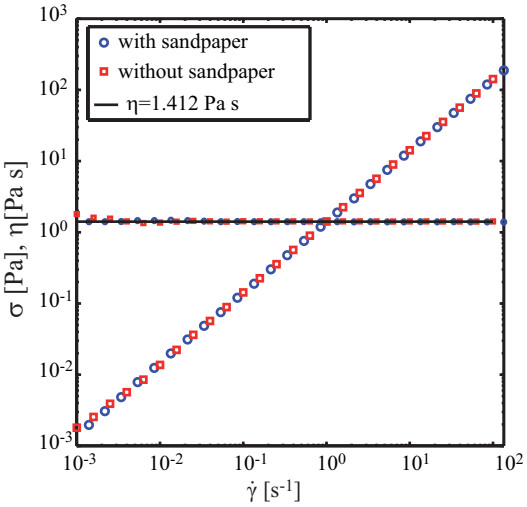

Figure 2.6: Validation of measurements with sandpaper. Small symbols: viscosity, big symbols: stress. Red squares show measurements of Glycerol without sandpaper, blue circles show measurements of Glycerol with sandpaper that were calculated with eqs. 2.2-2.3.

2.4.1.2. Procedure of Determining the Fluid's Rheology During Flow Tests

To verify the repeatability of the rheological measurements we carried out two tests under the same conditions (fig. 2.7). First the fluid was pre-sheared at the lowest shear rate measured in the flow test for a duration of 600 s. We then decreased the shear rate from $100\,\mathrm{s}^{-1}$ to $10^{-4}\,\mathrm{s}^{-1}$ (or $10^{-3}\,\mathrm{s}^{-1}$ respectively), increasing the measurement-time from 15 s at $\dot{\gamma} = 100\,\mathrm{s}^{-1}$ to 3000 s at $\dot{\gamma} = 10^{-4}\,\mathrm{s}^{-1}$, following a logarithmic ramp in order to measure sufficiently long. This is important to avoid transitional effects that can occur when the product of time measured at one shear rate and the shear rate itself becomes smaller than one, $\Delta t_{\mathrm{MP}}\,\dot{\gamma} < 1$, e.g. Mezger and Zorll [2002]. This is the case for $\dot{\gamma} < 10^{-3}\,\mathrm{s}^{-1}$ (fig. 2.7 dashed grey line), and therefore those values have to be neglected. But even then the effective shear on the fluid is low, as the number of revolutions (n_o) at $\dot{\gamma} = 10^{-3}\,\mathrm{s}^{-1}$ is very low, i.e. $n_o = 0.016$. Hence we also show results for a stricter criterion, regarding only values where $n_o > 0.05$. This implies that only values measured at shear rates $\dot{\gamma} > 10^{-2}\,\mathrm{s}^{-1}$ (fig. 2.7 straight grey line) can be considered. Therefore the yield stress is in between $\sigma_0 = 0.07\,\mathrm{Pa}$ and $\sigma_0 = 0.1\,\mathrm{Pa}$ with a total error of 30 %.

The rheology of such a fluid can be described by a Herschel-Bulkley model (e.g. *Piau [2007], Coussot et al. [2009], Divoux et al. [2010]*)

$$\sigma = \sigma_0 + K_\nu\,\dot{\gamma}^n \tag{2.4}$$

where σ is the stress, σ_0 the yield stress, K_ν the consistency, $\dot{\gamma}$ the shear rate and n the shear-thinning parameter. Various measures for the yield stress exist in standard rheology. In this thesis the first definition will be used

- 1) Rotational test: Decreasing the shear rate and measuring the stress in the limit of vanishing shear rate

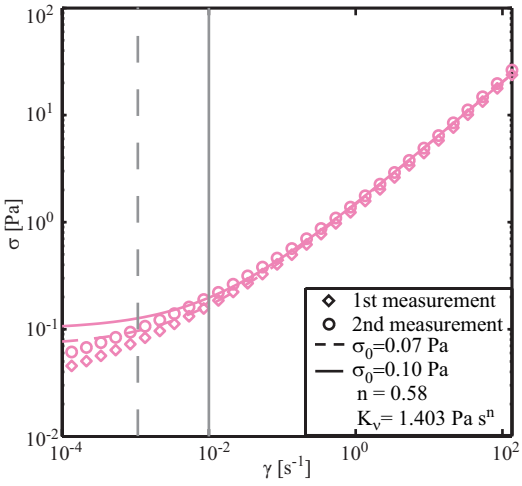

Figure 2.7: Flow test at $T = 20\,^{\circ}\mathrm{C}$ from high to low shear rate values. Symbols indicate two different measurements. Magenta lines refer to fitting Herschel-Bulkley model for ($\sigma_{0min} = 0.07\,\mathrm{Pa}$) and ($\sigma_{0max} = 0.1\,\mathrm{Pa}$) yield stresses. Dashed grey line marks shear rate below which product of measuring time and shear rate becomes smaller than one ($\dot{\gamma} = 10^{-3}$). Solid grey line marks shear rate below which the number of revolutions becomes smaller than $n_o = 0.05$ at ($\dot{\gamma} = 10^{-2}\,\mathrm{s}^{-1}$).

- 2) Amplitude sweep test: sweeping the amplitude from low to high values at constant frequency. The yield stress corresponds to the stress where the storage (elastic) modulus *G'* and the loss (viscous) modulus *G''* cross.

- 3) Rotational test at constant low shear rate: the stress increases through a maximum value and then decreases towards a constant value. The yield stress maybe defined as the value where the increasing stress deviates from a normal development or as the constant value towards which the system evolves.

The definition applied in this thesis will correspond to the first.

We therefore fitted our data with a Herschel-Bulkley model. For the range $\dot{\gamma} > 10^{-3}\,\mathrm{s}^{-1}$ (respecting the measured values as upper and lower limits) the fit results in a yield stress range $\sigma_0 = [0.0700, 0.0715]\,\mathrm{Pa}$ with $n = 0.58$ and $K_\nu = 1.403\,\mathrm{Pa\,s}^{1/\mathrm{n}}$. For the more strict criterion $\dot{\gamma} > 10^{-2}\,\mathrm{s}^{-1}$ we find a yield stress range of $\sigma_0 = [0.0700, 0.1000]\,\mathrm{Pa}$, with n and K_ν as above.

2.4.2. Dependence of Rheology on pH

A detailed study of how the rheology of Carbopol changes with pH and concentration is given by *Gutowski et al. [2012]*. They also provide a quantitative analysis of the influence on the structure (fig. 2.8). The dark region is water, the lighter regions are the Carbopol particles. The images show, that increasing the pH leads to a swelling of the particles.

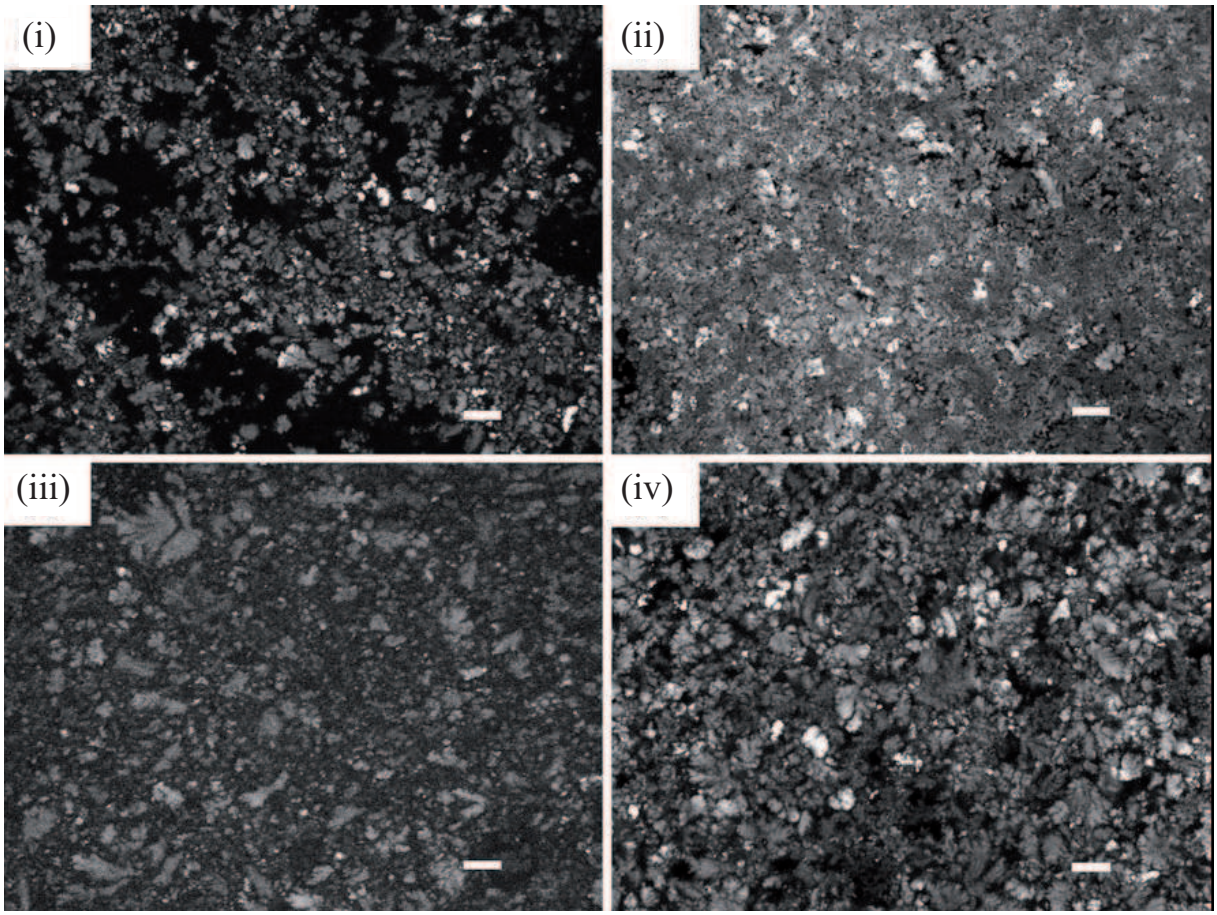

Figure 2.8.: from *Gutowski et al. [2012]*. Confocal images of low pH Carbopol gels dyed with Acridine Orange. The length of the scale bar is 20 μm. (i) 0.05 wt.% pH 3.8 (unmodified) Ultrez 10. (ii) 0.5 wt.% pH 3.5 (unmodified) Ultrez 10. (iii) 0.05 wt.% Ultrez 10 at pH $\approx$ 4. (iv) 0.5 wt.% pH 3.0 (unmodified) ETD 2050.

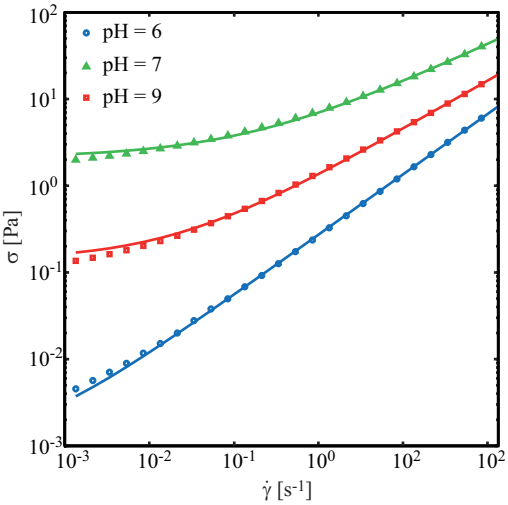

Figure 2.9: Flow test for fluids neutralized to different pH at $T = 20\,°C$ from high to low shear rate values. Blue circles: fluid with $pH = 6$, $\sigma_0 < 0.01$, $K_\nu = 0.2715$, $n = 0.6966$, red triangles: fluid with $pH = 7$, $\sigma_0 = 4.8611$, $K_\nu = 4.8611$, $n = 0.4644$, green squares: fluid with $pH = 9$, $\sigma_0 = 0.1392$, $K_\nu = 1.2254$, $n = 0.5599$.

We have conducted a series of measurements with Carbopol ETD 2623 (Noveon) to test the sensitivity towards changing the pH of the fluid. Fig. 2.9 shows, that the fluid hardly presents any yield stress at $pH = 6$. The yield stress then first increases with increasing pH and decreases again, as also found in *Gutowski et al. [2012]*.

2.4.3. Sweep Test

One possibility to characterize viscous and elastic material properties is an amplitude-sweep test, where the material is deformed with a sinusoidal amplitude at fixed frequency. The procedure is described in details in *Macosko [1994]*. The strain is calculated as follows

$$\gamma = \frac{1}{10}\,\frac{1+\delta^2}{\delta^2-1}\,\Phi \tag{2.5}$$

where Φ is the deflection angle. The stress is calculated as in equation 2.2. The storage (elastic) modulus G' and the loss (viscous) modulus G'' are then calculated as follows

$$G' = \frac{\sigma\, cos(\phi)}{\gamma} \quad \text{and} \quad G'' = \frac{\sigma\, sin(\phi)}{\gamma}, \tag{2.6}$$

where ϕ is the phase angle. Fig. 2.10 shows an amplitude-sweep test performed on Carbopol. G' and G'' have the same order of magnitude, i.e. the material is visco-elastic.

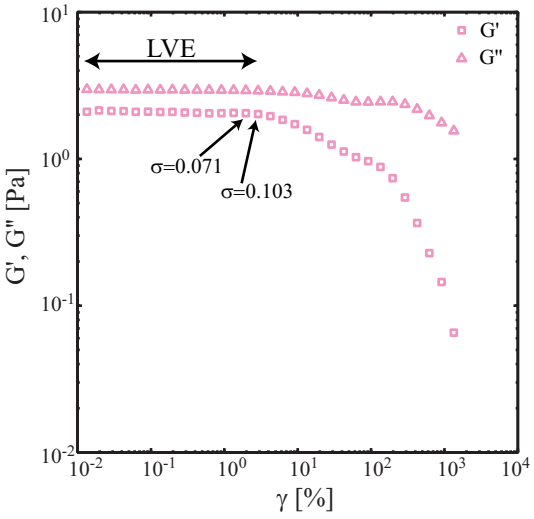

Figure 2.10: Example for an amplitude-sweep test for Carbopol (CBP6). The arrow marked with LVE indicates the linear visco-elastic range. The stress value at the end of the LVE corresponds to the yield stress determined with the flow test fig. 2.7. In the LVE the mean values are $\langle G' \rangle = 2.083\,\mathrm{Pa}$ and $\langle G'' \rangle = 2.948\,\mathrm{Pa}$.

2.4.4. Properties of Fluids used in the Plume Experiments

2.4.4.1. Preparation of Carbopol for Plume-Experiments

The fluid used in the plume experiments is a mixture of Carbopol (ETD2050, Lubrizol), distilled water and pure Glycerol[1]. For the experiments, between 10 and 18 l were prepared in different batches. Each batch contains a mixture of $30 - 50\,\mathrm{Vol.\%}$ Glycerol in water. After mixing, 0.6 g/l Carbopol were added and stirred with a magnetic agitator for two days to hydrate. To guarantee that the fluid is stable and presents a yield stress which is not too big (cf. 2.4.2) each batch was neutralized to a pH $= 7.5 \pm 0.2$ with a NaOH solution (5 M), using a pH-meter ISFET (IQ Scientific Instruments Inc., www.phmeters.com) whose pH range is between 0.00 and 14.00 with an accuracy of 0.01. Once the fluid reaches a certain pH-value (pH $\cong$ 6) a significant yield stress appears (cf. fig. 2.9). This causes NaOH drops to stay on top of the fluid and homogeneous mixing becomes difficult. We therefore mixed the fluid carefully by hand, in addition to the magnetic agitator, to be sure to measure a pH, which is representative for the whole fluid. Bubbles due to mixing of the fluid were removed by using an ultrasound bath. The ultrasound causes the bubbles to merge together, hence they become buoyant enough to rise. After a few days we mixed all Carbopol batches, added TLCs and particles for PIV and finally poured the mixture into the tank.

[1] A plume may only form, if the buoyancy induced stress is high enough compared to the yield stress (cf. *Davaille et al. [2013]*, *Darbouli et al. [2013]*). To avoid the difficulties in measuring very small yield stresses, we add glycerol to enhance the thermal expansivity.

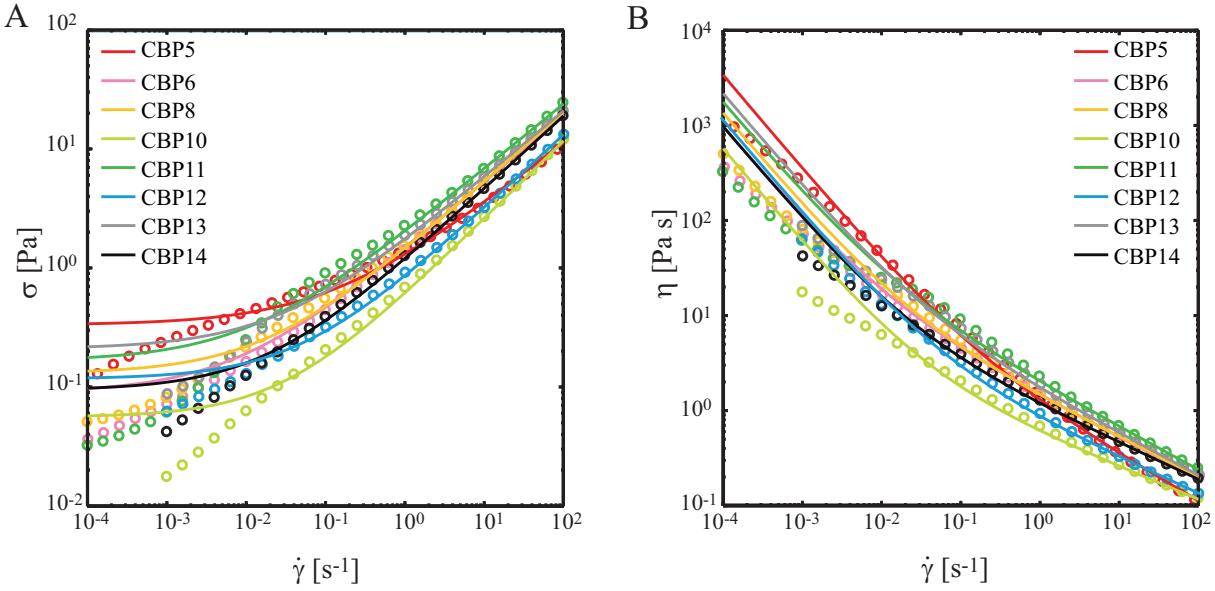

Figure 2.11.: A: stress and B: viscosity for measurements and fits of the fluids used in this study, the values are listed in table 2.3.

2.4.4.2. Flow Test Tesults for Carbopol used in the Plume Experiments

The rheological properties have been determined following the procedure in section 2.4.1.2. The glycerol-water ratio has been 50/50 ($Vol\%$) for all fluids, except CBP5 (33/67) and CBP8 (55/45). CBP10 has been neutralized to a higher pH ($pH = 9 \pm 0.2$). The results from the flow test and the corresponding fits are shown in fig. 2.11, whereby the parameters used for the fits are summarized in table 2.3. The yield stress of the different batches changes over almost one order of magnitude between $\sigma_0 = 0.05596\,\mathrm{Pa}$ and $\sigma_0 = 0.3337\,\mathrm{Pa}$. Besides the different glycerol-water ratios and pH, different effective rheologies maybe due to the preparation procedure. Due to the magnetic agitator, some Carbopol may stick to the wall of the beaker and not go into the fluid, therefore lowering the effective concentration. Some measurements present strong shear banding, when the stress values do not follow the yield stress plateau, but form a "hump" instead (cf. fig. 2.11 (i) CBP8, between $\dot{\gamma} = 10^{-2}\,\mathrm{s}^{-1}$ and $\dot{\gamma} = 10^{0}\,\mathrm{s}^{-1}$). The shear banding-effect is largely discussed in literature (e.g. *Coussot et al. [2009, 2008], Divoux et al. [2010]*) and occurs below a critical deformation (fig. 2.12) where the transition from the solid towards the liquid regime occurs (*Coussot et al. [2009]*).

2.4.4.3. Amplitude Sweep Test Results for Carbopol used in Plume Experiments

For some samples, an amplitude sweep test has been performed. The measurements are shown in fig. 2.13 and the average values for the visco-elastic properties in the linear

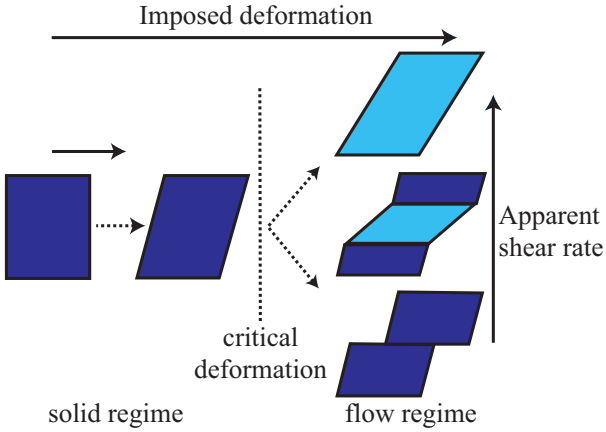

Figure 2.12: Deformation of a sample showing shear banding, modified after *Coussot et al. [2009]*. In the solid regime deformation is uniform. In the flow regime an apparent shear rate is measured, while "bands" form inside the sample, that are sheared at different shear rate.

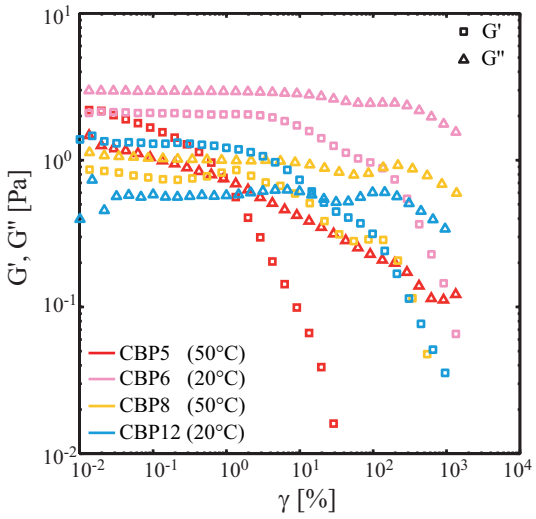

Figure 2.13: Visco-elastic properties of some Carbopol solutions, obtained from amplitude-sweep test. The mean values in the LVE are summarized in table 2.3.

visco-elastic range (LVE) are summarized in table 2.3. Generally storage and loss modulus are of the same order of magnitude. While for CBP5 and CBP12 the storage modulus is higher than the loss modulus, it is the other way round for CBP6 and CBP8.

2.4.4.4. Thermal Properties of Fluids used in the Plume Experiments

The fluid properties are summarized in table 2.4. The density has been determined using a DMA 4100 densimeter (Anton Paar, www.anton-paar.com) with an accuracy of $0.001\,\mathrm{g/cm^3}$. cf. fig. 2.14. The thermal expansivity α has been determined from the slope of the curve of the density as a function of temperature within the linear range between 20 °C and 40 °C. Thermal conductivity k and heat capacity C_p have been determined from the properties of water and Glycerol.

Table 2.3.: Thermal and rheological properties of different Carbopol mixtures. Yield stress consistency and shear thinning exponent have been measured at $T = 20\,^{\circ}\mathrm{C}$, storage and loss modulus at the indicated temperatures.

Name	σ_0 [Pa]	K_ν [Pa s^n]	n [-]	$\langle G' \rangle$ [Pa]	$\langle G'' \rangle$ [Pa]
CBP5	0.33	0.980	0.53	2.198 (50 °C)	1.475 (50 °C)
CBP6	0.09	1.403	0.58	2.083 (20 °C)	2.948 (20 °C)
CBP8	0.13	1.350	0.59	0.790 (50 °C)	1.035 (50 °C)
CBP10	0.06	0.565	0.66	-	-
CBP11	0.17	1.896	0.55	-	-
CBP12	0.12	0.622	0.75	1.300 (20 °C)	0.567 (20 °C)
CBP13	0.21	1.555	0.56	-	-
CBP14	0.09	1.114	0.62	-	-

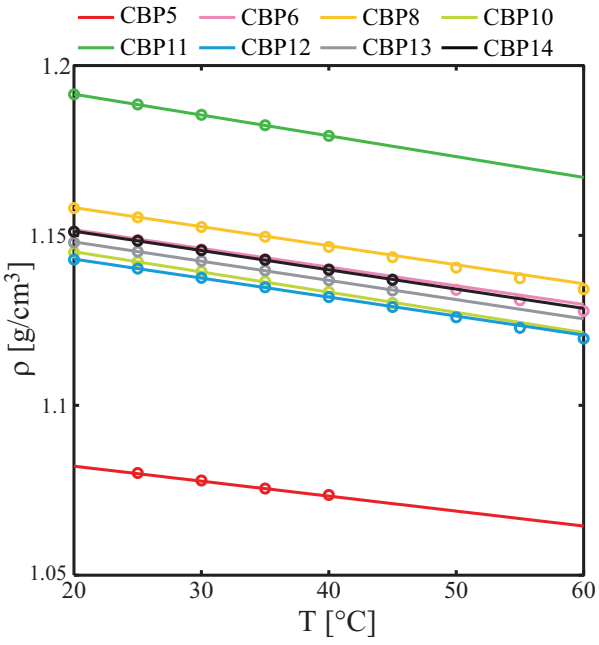

Figure 2.14: Density of the different fluids as a function of temperature.

Table 2.4.: Thermal properties of different Carbopol mixtures.

Name	$\rho_0\,[\mathrm{kg/m^3}]$	$\alpha\,[10^{-4}\,\mathrm{K^{-1}}]$	$C_p\,[\mathrm{J/kg\,K}]$	$k\,[\mathrm{W/m\,K}]$
CBP5	1082	4.07	3678	0.4984
CBP6	1151	4.78	3286	0.435
CBP8	1158	4.84	3196	0.4205
CBP10	1145	5.19	3286	0.435
CBP11	1192	5.14	3286	0.435
CBP12	1143	4.88	3286	0.435
CBP13	1148	4.93	3286	0.435
CBP14	1151	4.96	3286	0.435

3. Regimes, Onset and Morphology

To complete the study started by B. Gueslin and A. Davaille (*Davaille et al. [2013]*), I have carried out a number of new experiments. In these experiments I focussed on the long-time behaviour of the thermal instability. I have varied the height of the fluid and extended the observation time (table 3.1). To better understand certain aspects, I have complemented the experiments with numerical simulations and a detailed parameter study (chapter 4).

3.1. Regimes and Onset - Influence of the Source Geometry

In *Davaille et al. [2013]* (for details see Appendix A.1), we have shown, that the development of a plume depends on whether the thermally induced stress σ_{th} is sufficiently high to overcome the yield stress σ_0 of the fluid. Thereby the thermally induced stress is due to the stress acting on the surface of the hot pocket forming around the heater and is defined as

$$\sigma_{th} = \frac{\alpha \rho g P}{k}, \tag{3.1}$$

where ρ is the density at room temperature. The ratio of σ_{th} and the yield stress is called the yield parameter $Y_0 = \sigma_{th}/\sigma_0$. For experiments with the same fluid, but operated at different power P, three regimes are distinguished by two critical values of the yield parameter. In *Davaille et al. [2013]* we found, that at $Y_0 < Y_{c1} = 120 \pm 15$ the fluid does not move at all. For $Y_{c1} < Y_0 < Y_{c2} = 260$ a small cell develops, whose convective motion is confined around the heater. Only for $Y_0 > Y_{c2} = 260$ a plume rises through the fluid. Fig. 3.2A shows the regime diagram for the experiments from *Davaille et al. [2013]* and this study, where circles stand for the regime with no motion, triangles for the cell and squares for the plume regime. The two studies clearly do not show the same trend (fig. 3.2A and B). There is a systematic shift for the two boundaries Y_{c1} and Y_{c2}. This is also observed for the onset time. As the fluid employed is the same, this has to be due to the different geometries of the heat sources. The difference could be due to the different mechanical boundary condition. While they are rigid in this study, they are a mixture of rigid and free-slip in *Davaille et al. [2013]*. But this effect should make it easier for the instabilities observed in *Davaille et al. [2013]* to evolve, as shown by *Darbouli et al. [2013]*.

Table 3.1.: Summary of experiments added by this study to previously existing experiments *Davaille et al. [2013]*. Onset times in brackets indicate longest time waited during the experiment.

Experiment	Fluid	Power [W]	Type	Onset time s	h_{fluid} [cm]
20110221	CBP5	3.30	nothing	($>$ 3 days)	36.2
20110223	CBP5	3.50	nothing	($>$ 3 days)	24.2
20110223	CBP5	3.60	nothing	($>$ 3 days)	24.2
20110404	CBP6	1.85	plume	7194	39.2
20110407	CBP6	1.67	plume	10182	39.2
20110411	CBP6	1.50	plume	16836	39.2
20110413	CBP6	1.89	plume	2855	28.4
20110426	CBP6	1.45	plume	12114	28.4
20110429	CBP6	2.02	plume	2775	18.6
20110502	CBP6	1.68	plume	4385	18.6
20110504	CBP6	1.55	plume	12114	18.6
20110812	CBP8	2.40	plume	2775	22.8
20110814	CBP8	2.40	plume	4384	22.8
20110816	CBP8	1.90	plume	5209	22.8
20110818	CBP8	1.92	plume	4655	22.8
20120515	CBP11	1.70	plume	60960	24.0
20120520	CBP11	1.82	plume	12480	23.4
20120521	CBP11	2.08	plume	1740	23.4
20120524	CBP11	2.10	plume	1680	23.4
20120526	CBP11	2.10	plume	1680	13.3
20120527	CBP11	2.18	plume	1320	6.5
20120529	CBP11	2.15	plume	1320	7.2
20120703	CBP12	1.84	plume	432000	35.2
20120709	CBP12	2.08	plume	129600	35.2
20120715	CBP12	2.08	plume	157200	35.2
20120721	CBP13	1.83	cell	(270000)	40.2
20120727	CBP13	2.26	cell	(1080000)	40.2
201208101	CBP14	2.35	plume	1120	31.8
201208102	CBP14	2.31	plume	1105	31.8
20120811	CBP14	2.02	plume	1751	20.0
20120812	CBP14	2.02	plume	1665	20.0

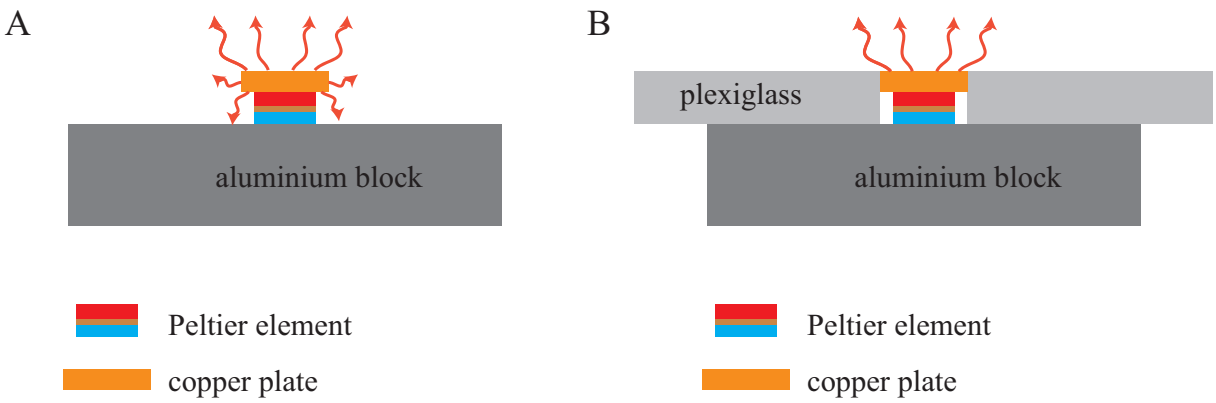

Figure 3.1.: A: heating as employed in *Davaille et al. [2013]*, heat is distributed into several directions. B: heating as employed in this study, the copperplate is insulated by plexiglass, heat only escapes at the top of the copper plate.

However the opposite is observed here. Another reason could be the power available by the plume. While *Davaille et al. [2013]* use a Peltier element with a copper plate on its top, in this study we insulate the copper plate towards the sides with a plexiglas plate, for easier comparison with numerical simulations. Therefore the calculated thermal power is distributed in different ways. While in this study heat can only escape through the top of the copper plate, in *Davaille et al. [2013]* heat also goes trough the side walls of the copper plate. As we have no measure for the heat distribution below the copper plate (where the Peltier element is cooling and heating the fluid), we assume that the biggest heat loss occurs at the sides. To test this assumption simple geometrical analysis gives a correction for the thermal power as:

$$P_{Plume} = P\frac{\pi r_{Cu}^2}{\pi r_{Cu}^2 + 2\pi r_{Cu} d_{Cu}}, \tag{3.2}$$

where r_{Cu} and d_{Cu} are the radius and the height of the copper plate. The results are shown in fig. 3.2C and D. Applying the correction the data collapses very well. The critical yield parameters are changed to $Y_{c2} = 150 \pm 10$ and $Y_{c1} = 100 \pm 10$.

3.2. Evolution and Morphology

In *Davaille et al. [2013]* we show that the thermal instability evolving in Carbopol does not have the classical mushroom-like shape as encountered for less viscous hot plumes in Newtonian fluids, but more a finger-like shape (fig. 3.3A). Furthermore we can see that deformation is very localized to the thermal instability. When increasing the height of the fluid, another interesting aspect may be observed. As plume rises, it stops midway

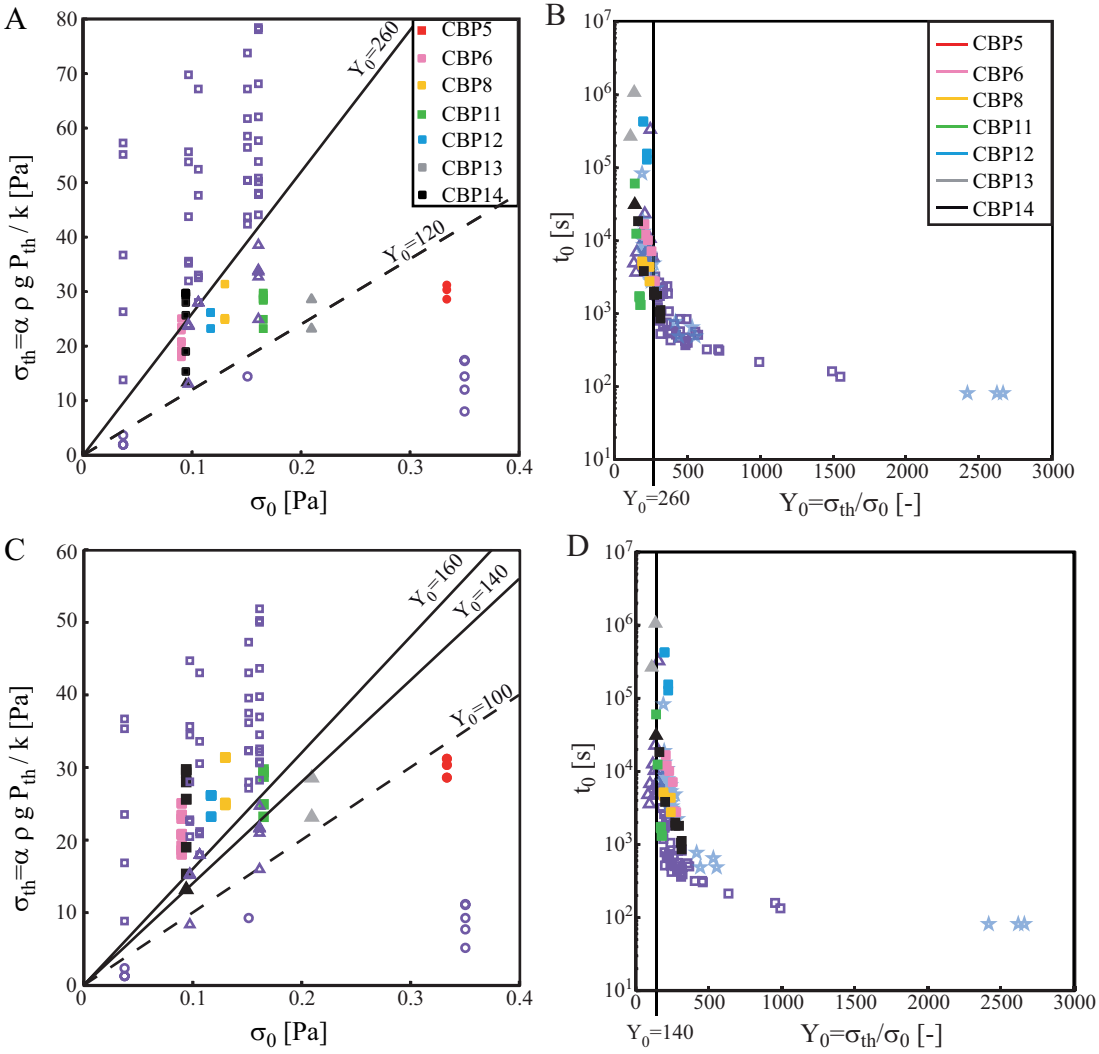

Figure 3.2.: Regime diagram (A) and onset time (B) calculated with total thermal power P emitted from the copper plate. C and D show the same plots, where the thermal power of the experiments from *Davaille et al. [2013]* have been corrected to compensate for the heat loss at the sides of the copper disk. Filled symbols: experiments with CBP6-14, empty violet symbols: experiments from *Davaille et al. [2013]*, blue stars: numerical simulations from *Massmeyer et al. [2013]*. Triangles are cells observed for the corresponding fluid and given yield parameter.

in the tank (fig. 3.3B). While the material inside the instability continues to convect, the material above is not moving, i.e. an unyielded region persists at the top of the box. To better understand why the plume stops at a given height and what is the role of the rheological parameters, I performed numerical simulations, systematically varying the rheology of the fluid.

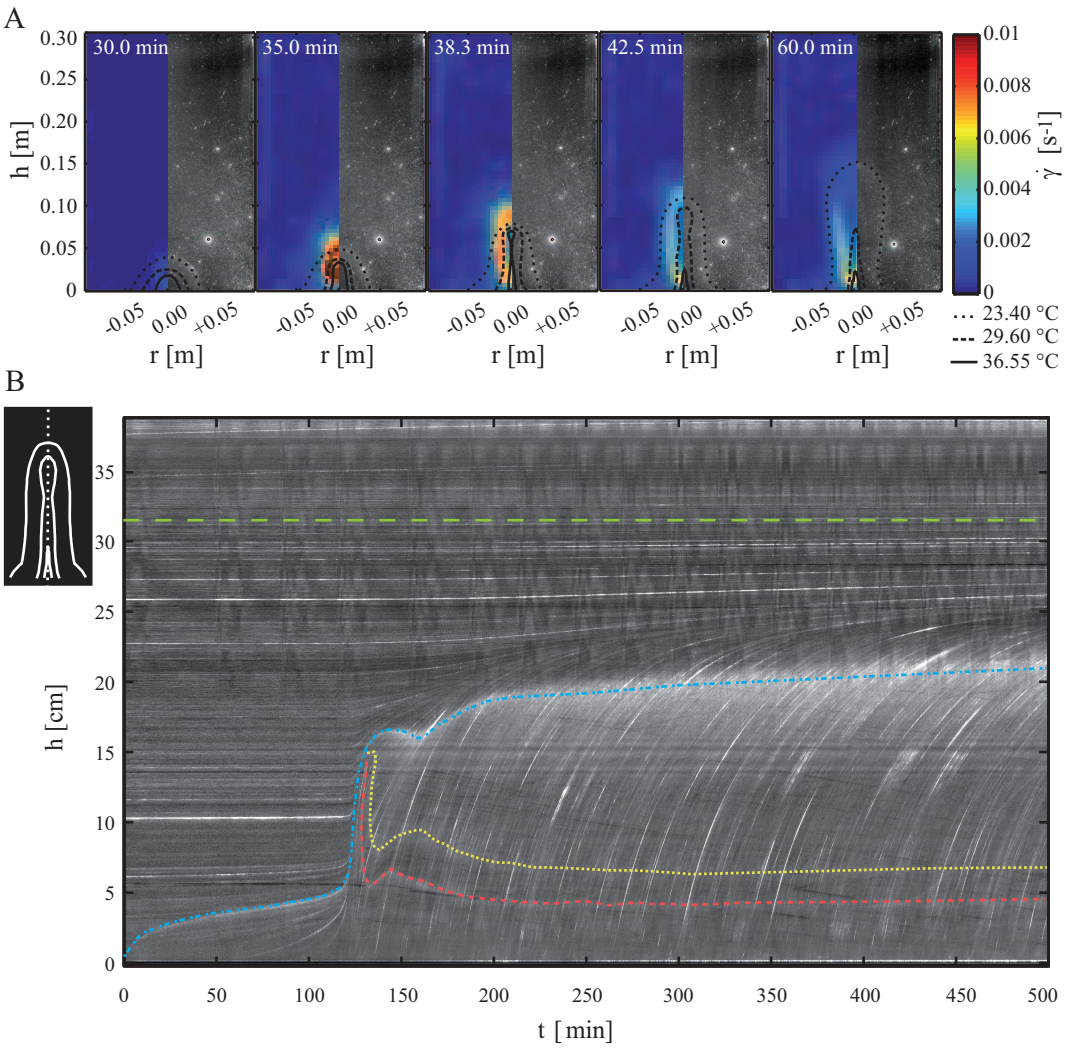

Figure 3.3.: A: Shear rate (color code) and raw image for experiment 20120811 in CBP14. B: Spatiotemporal evolution of a vertical pixel-line at the plume axis (as illustrated by sketch) for experiment 20110404 in CBP6. Colored lines highlight isotherms at 23.9 °C (blue), 31.1 °C (yellow) and 39.9 °C (red). Green line indicates unyielded region.

4. Numerical Simulation of Thermal Plumes in a Herschel-Bulkley Fluid[1]

Abstract

We present a three dimensional numerical study of thermal plumes, developing from a localized heat source in a yield stress and shear thinning fluid. We assume that the fluid viscosity follows a Herschel-Bulkley law with a low shear rate viscosity plateau. Comparison of the plume onset time and morphology observed in the numerical study and in laboratory experiments with Carbopol shows good agreement. An extensive parameter study allows us to identify two local non-dimensional parameters that determine whether a plume rises through the fluid. The first parameter is the Bingham number, Bi, which compares the yield stress to the viscous stress. The second parameter, the yield number Ψ, compares the stress induced by the buoyancy of an equivalent hot sphere to the yield stress. We find that a plume develops only if $\Psi > \Psi_c = 5 \pm 1.2$ and $Bi < Bi_c = 1$. As the plume rises it loses its buoyancy due to heat diffusion. So the upward progression of the plume halts as soon as $\Psi < \Psi_c$ or $Bi > 1$. Hot fluid continues to rise from the bottom of the tank but spreads under an unyielded, high viscosity region at the top of the box.

4.1. Introduction

Thermal convection and instabilities in yield stress fluids occur in many different fields, from engineering (food- or glass production, *Hunt [1991]*, *Steffe [1996]*) to geoscience (formation of dikes and diapirs in the lithosphere or convection in icy satellites (*Solomatov and Barr [2006]*). Despite its huge importance it is still not very well understood.

The theoretical difficulty in studying such systems is caused by an infinite viscosity as the shear rate approaches zero. Therefore an instability cannot grow from a conductive profile exposed to an infinitesimal perturbation (*Solomatov and Barr [2006]*, *Zhang et al. [2006]*, *Balmforth and Rust [2009]*). Former studies on thermal instabilities in Rayleigh-Bénard convection in a yield stress fluid considered either a Bingham fluid (*Zhang et al.*

[1]This chapter has been published in *Journal of Non-Newtonian Fluid Mechanics*, *Massmeyer et al. [2013]*.

[2006], *Vikhansky [2009, 2010, 2011]*, *Turan et al. [2010, 2012]*) or a purely shear thinning fluid (*Barr et al. [2004]*, *Solomatov and Barr [2006]*). However, fluids exhibiting a yield stress as well as shear thinning behaviour have not been studied extensively. *Balmforth and Rust [2009]* investigated the stability of a weakly non-linear fluid concluding that shear thinning favors an early onset of convection whereas a yield stress suppresses convection. The same authors tested their numerical predictions experimentally on Carbopol solutions in a Rayleigh-Bénard setup and found that fluids with a high Carbopol concentration, i.e. high yield stress, start to convect only if exposed to finite perturbations.

In a recent study *Davaille et al. [2013]* investigated the development of a thermal plume in Carbopol rising from a localized heat source. The Carbopol rheology can be described by a Herschel-Bulkley model (*Piau [2007]*, *Coussot et al. [2009]*, *Oppong and de Bruyn [2011]*, *Divoux et al. [2011]*). The experiments showed that thermal instabilities in a yield stress fluid behave very differently from those in Newtonian liquids.

A key parameter is the yield parameter, Y_0, which compares the thermally induced stresses to the yield stress and is therefore written as

$$Y_0 = \frac{\alpha \rho g P}{k \sigma_0}, \tag{4.1}$$

where α is the thermal expansivity, ρ is the density of the fluid at ambient temperature, g the acceleration due to gravity, P the thermal power supplied by the heat source, k the thermal conductivity and σ_0 the yield stress of the fluid. Depending on the yield parameter Y_0, the system evolves into one of three regimes, which are seperated by two critical yield parameters, Y_{c1} and Y_{c2} (cf. *Davaille et al. [2013]*). For $Y_0 < Y_{c1}$ only elastic deformation occurs, while for $Y_{c1} < Y_0 < Y_{c2}$ a small cell slowly convects around the heater. Only a high yield parameter ($Y_0 > Y_{c2}$) allows the cell to evolve into a plume. This yield parameter is not to be mistaken for the yield number, Ψ, which is applicable to problems involving rising bubbles (*Dubash and Frigaard [2004, 2007]*) or sinking spheres (*Beris et al. [1985]*, *Tabuteau et al. [2007]*) in a yield stress fluid. The yield number is defined as

$$\Psi = \frac{\Delta\rho \, g \, 2 \, r_{eq}}{3 \, \sigma_0}. \tag{4.2}$$

For bubbles and spheres, $\Delta\rho$ is the density difference between the object and the fluid and r_{eq} is the radius of the object. Bubbles or spheres move if $\Psi > \Psi_c = 6.85$ (*Beris et al. [1985]*, *Dubash and Frigaard [2004, 2007]*, *Tabuteau et al. [2007]*). For a thermal instability, $\Delta\rho = \alpha \rho \Delta T$ and r_{eq} corresponds to the radius of a sphere with a volume equivalent to the volume of the hot pocket that forms around the heater (*Davaille et al. [2013]*). Therefore for a thermal instability, although Y_0 is constant, Ψ evolves with time as the thermal boundary layer grows. It has been observed experimentally that the plume develops when $\Psi > 8.8 \pm 0.7$ (*Davaille et al. [2013]*).

The onset time t_0 of this plume, i.e. the time at which the plume starts to rise, depends

on the yield parameter and increases with decreasing yield parameter. As Y_0 tends to Y_{c2}, the onset time goes to infinity. The shape of the thermal instability looks like a finger, unlike in a Newtonian fluid, where hot, less viscous plumes have a mushroom shape with a big head on a thin stem (*Davaille et al. [2011]*). Most deformation is localized to the edges of the thermal anomaly and is orders of magnitude smaller within the thermal anomaly. This produces a pseudo-plug area on the plume axis. The evolution in time changes, depending on the rheological parameters of the fluid. For small consistencies, K_ν, the plume can show an episodic behaviour whereas it rises continously for high K_ν.

In this study we use numerical simulations to investigate the extent to which a purely viscous fluid description, using a regularized Herschel-Bulkley model, is able to describe the evolution from the cell to the plume instability as well as the instability itself. We therefore systematically vary rheological and thermal parameters, as well as the applied thermal history of the heated patch. To confirm the adequacy of the model, we compare the morphology, the evolution in time and the dependence of the onset time on the yield parameter, Y_0, observed in our numerical model to laboratory results. This validation allows us to study a well defined parameter range, avoiding the uncertainties due to the difficulty in accurately measuring the rheological parameters in the laboratory. The advantage of numerical simulations is that they allow us to test how each rheological parameter, yield stress σ_0, consistency K_ν and shear thinning exponent n, influence the evolution of the plume instability. We therefore varied these parameters systematically. Access to the full three dimensional fields allows us to find the key parameters that characterize the dynamics of the thermal instability.

4.2. The Model

4.2.1. Governing Equations

In this study, we consider the fluid to be incompressible and in the Boussinesq approximation. Furthermore we neglect viscous dissipation (*Gebhart [1962]*). The fluid can be described by the simplified equations for conservation of mass

$$\nabla \cdot \underline{v} = 0 \tag{4.3}$$

momentum

$$\frac{D\underline{v}}{Dt} = -\frac{1}{\rho_0}\nabla p + \alpha\,\Delta T\, g\,\underline{e}_z + \nabla \cdot \underline{\underline{\sigma}} \tag{4.4}$$

and energy

$$\frac{DT}{Dt} = \kappa \nabla^2 T \tag{4.5}$$

where $\underline{v}$ is the velocity, $D/Dt = (\partial/\partial t + \underline{v} \cdot \nabla)$ the material derivative, ρ_0 is the density of the ambient fluid, p the pressure, α the thermal expansivity, ΔT the temperature difference between heater and ambient fluid, g the gravity acceleration, $\underline{\underline{\sigma}}$ the stress tensor, T the temperature and κ the thermal diffusivity.

4.2.2. The Model Rheology

The viscosity of Carbopol depends mainly on the shear rate, but also on temperature. The shear rate dependence can be described with a Herschel-Bulkley model (*Piau [2007]*, *Coussot et al. [2009]*, *Divoux et al. [2010]*), which implies infinite viscosity as the shear rate approaches zero. To avoid this difficulty in the numerical simulations we apply a viscosity truncation. Different models exist for a regularized Herschel-Bulkley model (e.g. *Alexandrou et al. [2001]*, *Zhu et al. [2005]*). We choose the model of *de Souza Mendes and Dutra [2004]* due to its convenience for curve-fitting of the rheology measured in the laboratory. This allows for an easier comparison of simulations and experiments. The adequateness of this model to describe the flow of a Carbopol solution through an axi-symmetric expansion has been demonstrated in *de Souza Mendes et al. [2007]*. In a tensorial representation it is written as

$$\underline{\underline{\sigma}} = \left(1 - exp\left(\frac{-\eta_0\,\dot{\gamma}}{\sigma_0}\right)\right)\left(\sigma_0 + K_{\nu T}\,\dot{\gamma}^n\right)\underline{\underline{\dot{\gamma}}}\,\dot{\gamma}^{-1}\,, \tag{4.6}$$

where the expression in the first bracket is the regularizationterm and the expression in the second bracket describes the Herschel-Bulkley model. The yield stress is given by σ_0, K_ν is the consistency, n the shear thinning exponent and $\dot{\gamma}$ the magnitude of the strain rate $\underline{\underline{\dot{\gamma}}}$. η_0 represents the upper viscosity cut-off and is chosen to be $\eta_0 = 10^8\,\mathrm{Pa\,s}$ in all the calculations. In section 4.3.2.1 we show that the dynamics of the plume is mostly independent of the cut-off value. To avoid too large viscosity contrasts, our numerical code uses an additional lower cut-off for the viscosity. However, we made sure that this lower value is never reached, so that it does not influence the dynamics. The value was set to $\eta_{min} = 0.01\,\mathrm{Pa\,s}$ for $K_\nu \leq 0.1403\,\mathrm{Pa\,s^n}$ and to $\eta_{min} = 0.1\,\mathrm{Pa\,s}$ for the other cases.

The laboratory measurements showed that σ_0 and n do not depend on the temperature. However the consistency $K_{\nu T}$ varies with temperature, following an Arrhenius-type law

$$K_{\nu T} = K_\nu\, A\, e^{B\,(T-273.15)}, \tag{4.7}$$

where $A = 1.6927$, $B = -0.0257\,\mathrm{K^{-1}}$ and where K_ν is the consistency at room temperature $T = 293.15\,\mathrm{K}$ (for details see Appendix A).

4.2.3. The Numerical Model and Boundary Conditions

We solve the set of equations (4.3) - (4.5) using a finite volume discretization on a staggered grid, implemented in the code StagYY. Code details and benchmarking for

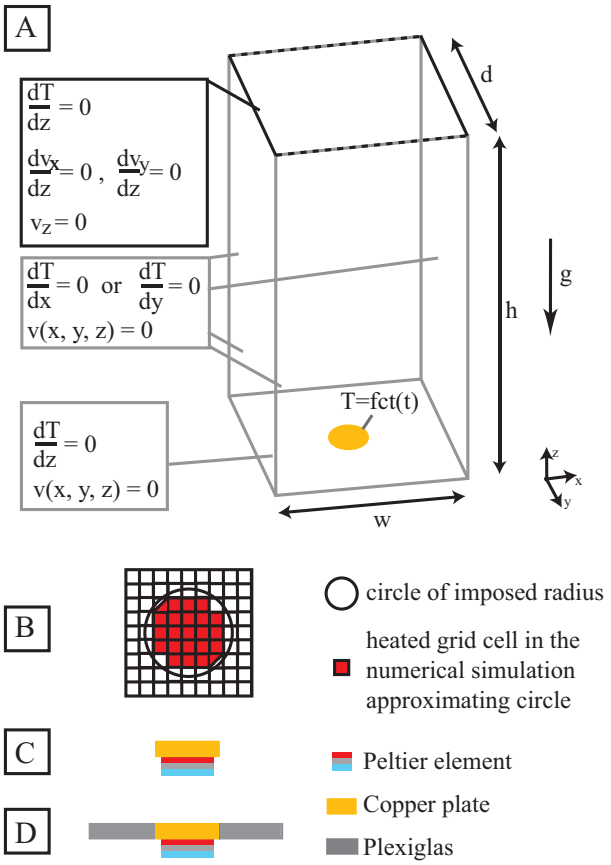

Figure 4.1: A: Schematic illustration of the numerical domain. The calculations are run in a box of $w \times d \times h = 20\,\text{cm} \times 20\,\text{cm} \times 40\,\text{cm}$ with a resolution of $n_x \times n_y \times n_z = 64 \times 64 \times 128$. Top boundary: free-slip, and kept at ambient temperature T_0, side walls and bottom plate: rigid with zero heat flux. Patch in the center of the bottom of the box follows a prescribed temperature evolution. B: schematic of the approximation of the circular heated patch in the numerical simulation. While in the simulations the heated patch is inside the bottom boundary, in the laboratory experiments it is either; C: bottom mounted *Davaille et al. [2013]* or D: flush mounted by embedding the copper disk into a Plexiglas plate.

constant viscosity and temperature-dependent viscosity cases are described in detail in *Tackley [1994]* (pp. 286-290 for benchmarking results) and more briefly in *Tackley [1993, 1996]*. For the diffusive term, second order finite differences are used, and a second order upwind scheme is used for the advective terms. The convergence criterion is met, if the normalized residuals of the momentum and continuity equations is smaller than 10^{-2}.

Even though most of the characteristics observed for the plume in the laboratory are axi-symmetric, the tank in the laboratory is not. We need to use straight walls in order to avoid optical distortions during the visualization. To ensure the same boundary conditions as in the laboratory, we use a three-dimensional Cartesian box (fig. 4.1). The box is 20 cm long and wide and 40 cm high with a resolution of $64 \times 64 \times 128$ grid points. We verified that higher resolutions give the same results. The boundary conditions are described by a no-slip and zero-flux condition for the bottom and sidewalls. The top boundary is free-slip and kept at ambient temperature. To compare with the experiments, for which the heating power is constant, we prescribed the temperature history of the heater measured in the laboratory experiments. We calculate the thermal power P, defined as the surface integral of the heat-flux

$$P = \int Q \, dA, \tag{4.8}$$

which is needed for comparison with the laboratory experiments (e.g. *Davaille et al. [2013]*), where Q denotes the heat flux and dA the surface through which the heat flux is measured. For the numerical simulations the thermal power is constant within 5 % through time, prior to the onset, and increases when the plume rises, as the heat flux is increased. We generally refer to the minimum value, when dealing with the thermal power P.

Due to the numerical grid (fig. 4.1 B) the heated surface is smaller than the surface of an equivalent circle with the same radius. With the resolution $64 \times 64 \times 128$ and a radius of $r = 1.25$ cm this implies a heated surface of $3.93\,\text{cm}^2$ instead of the surface of the circle $4.91\,\text{cm}^2$. The smaller surface of the disk results in a smaller heat flux and therefore a smaller thermal power P. However, *Davaille et al. [2013]* showed that the system depends strongly on the yield parameter Y_0 (equation 4.1), therefore a smaller P can be adjusted with a higher σ_0 or α.

4.2.4. The Laboratory Experiments

The setup of the laboratory experiments and the procedure by which the fluid is prepared is described in *Davaille et al. [2013]*. The heater consists of a Peltier element underneath a copper disk. In the first set of experiments (*Davaille et al. [2013]*) the heater was placed on top of the tank bottom (fig. 4.1 C). In addition, we performed a series of experiments with a flush mounted heater (fig. 4.1 D), in order to mimic the boundary conditions in the numerical simulations. Additionally in the new series we also studied the influence of higher fluid depths, up to $h = 39.2$ cm.

4.3. Validation of the Purely Viscous Description

4.3.1. Input and Output Parameters

In this study we systematically vary the thermal and rheological parameters (values listed in table 4.1) to evaluate the effect on the dynamics of the plume. Here we will briefly demonstrate the general evolution of a plume and how we evaluate the diagnostic parameters (listed in table 4.1).

Fig. 4.2 shows the typical evolution of the thermal instability. Upon heating, a hot pocket of fluid forms by heat conduction around the heater. Very slow motions are recorded in this hot pocket. After approximately one hour, a plume develops. The shape of the isotherm (fig. 4.2 A) resembles a finger.

From equation 4.6, we can calculate an effective viscosity

$$\eta = \underline{\underline{\sigma}}\,\underline{\underline{\dot{\gamma}}}^{-1} = \left(1 - exp\left(\frac{-\eta_0\,\dot{\gamma}}{\sigma_0}\right)\right)\left(\sigma_0 + K_\nu\,\dot{\gamma}^n\right)\dot{\gamma}^{-1}\,. \tag{4.9}$$

fig. 4.2 B shows that there remains an unyielded region (i.e. where the viscosity value remains at the cut-off value) at the top of the box during the whole simulation. This means that the plume has stopped rising. In the systematic study below, we shall use two diagnostic variables to characterize the plume evolution: the onset time t_0 (fig. 4.2 C), and the height where the plume stops h_y (fig. 4.2 D).

- Onset time: Lower viscosity regions form already at an early stage of the plume (fig. 4.2 B and C a)), due to a slowly convecting cell around the heater. The spatiotemporal evolution (fig. 4.2 C) shows that at $t = 62.33\,\text{min}$ (fig. 4.2 b)) this cell grows very fast. The time when the small cell evolves into a plume is referred to as the onset time t_0. Several methods to determine the onset time all give similar results within an error of 3 % (*Davaille et al. [2013]*). We will show how the transition from the cell to the plume takes place and provides a precise criterion for the determination of the onset time in section 4.5.1.

- Height where the plume stops: The spatiotemporal evolution of the viscosity on the plume axis (fig. 4.2 C) shows that even after the onset of the plume, high viscosity regions persist at the top of the box. This means that not the whole fluid is convecting, but only a part of it. To define the height where the plume stops we plot a profile of the viscosity on the plume axis (fig. 4.2 D). The viscosity shows a local minimum at the head of the plume. This local viscosity minimum corresponds to the point where the radial derivative of the radial velocity (dv_r/dr) becomes maximum. Hence, it marks the location of a stagnation point in the moving plume reference frame, and therefore the position of the top of the plume head (*Davaille et al. [2011]*). So, we define the maximum height that a plume reaches, or height

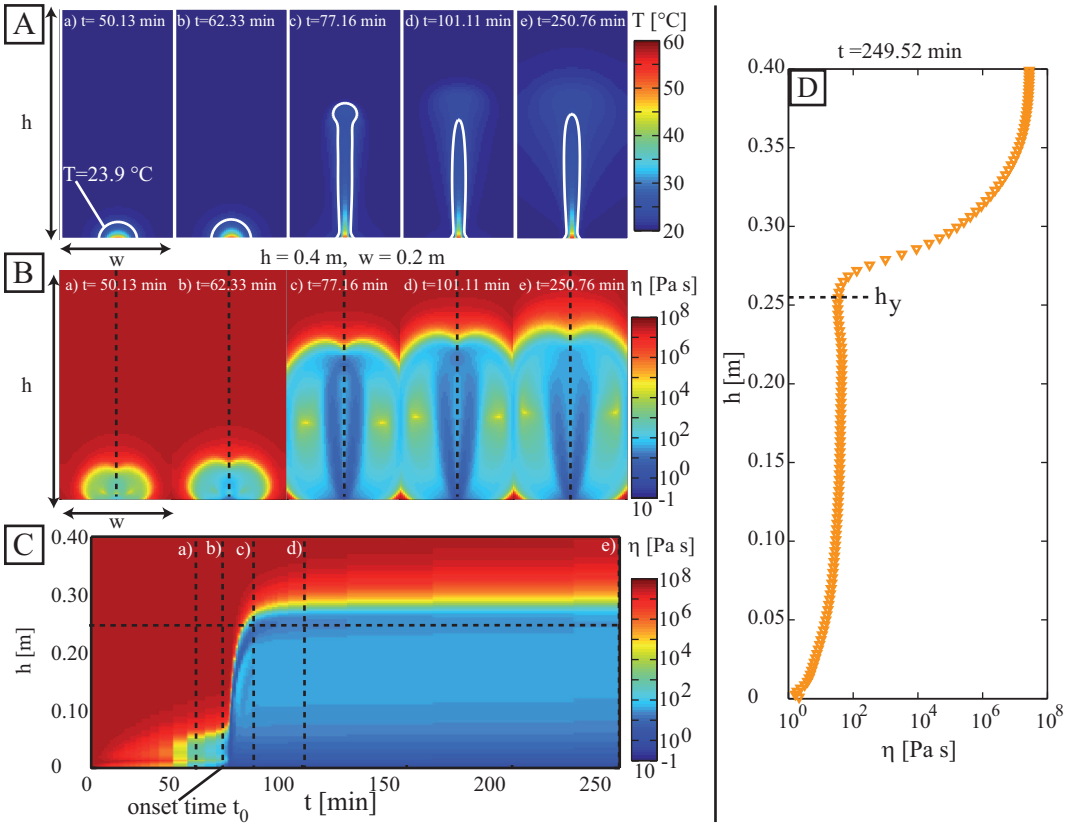

Figure 4.2.: Definition of output parameters. A: snapshots of the temperature field in the axis plane for different time steps marked in C. White lines mark the isotherm at $T = 23.9\,°C$. B: snapshots of the viscosity field on the plane through the plume axis. C: spatiotemporal evolution of a vertical line on the plume axis for the viscosity, vertical dotted lines in B and C correspond to each other. D: viscosity profile at $t = 249.52\,\text{min}$, h_y marks the height where the plume stops, corresponding to a local minimum in the viscosity, which marks the stagnation point.

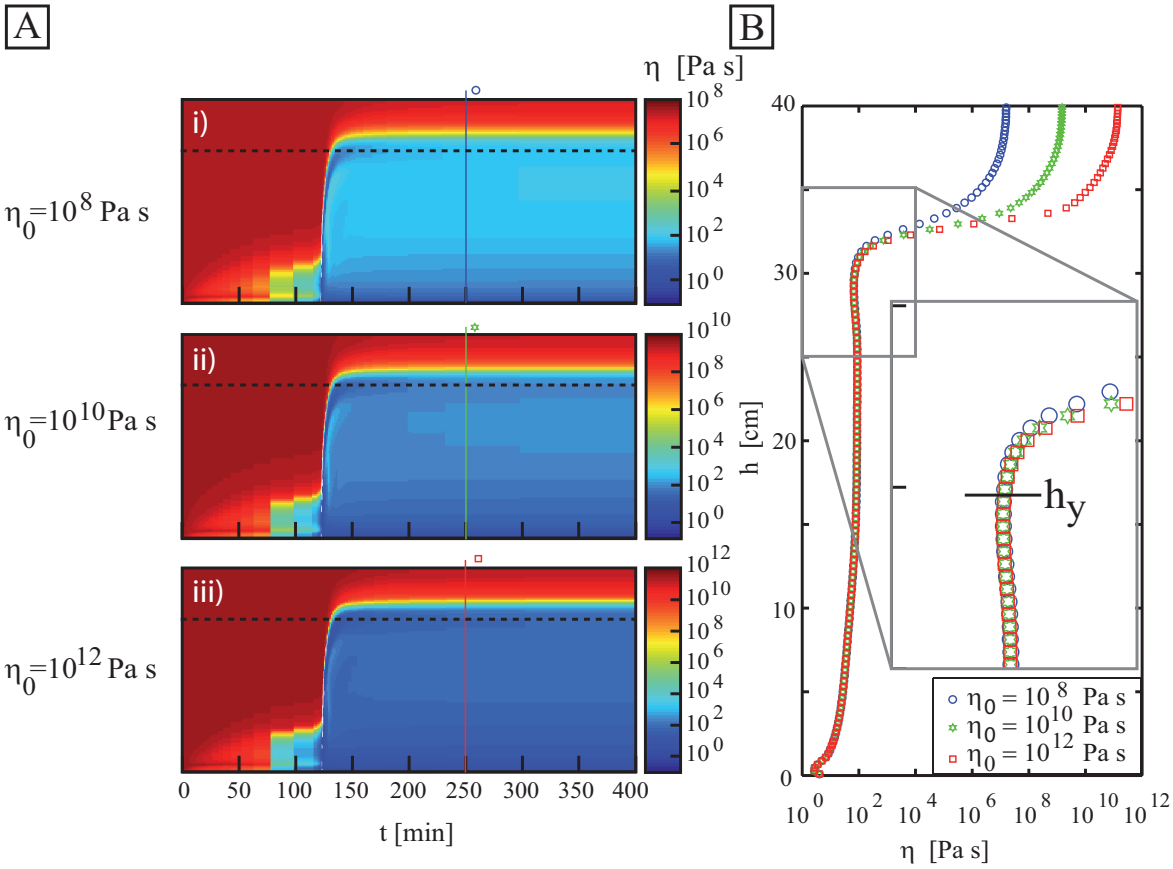

Figure 4.3.: A: Spatiotemporal evolution of the viscosity at the plume axis for three different viscosity cut-offs η_0. B: vertical viscosity profile at $t = 250$ min for the different cut-off values $\eta_0 = 10^8$ Pa s (blue circles), $\eta_0 = 10^{10}$ Pa s (green stars), $\eta_0 = 10^{12}$ Pa s (red squares). The height h_y in B is marked in A by the horizontal black dashed lines, corresponding to a local minimum viscosity.

where the plume stops, h_y, as the maximum height of the stagnation point. This height only varies very gently through time, once a quasi stationary state is reached. This is assured for all calculations 50 min after the onset of the plume, when the height changes become negligibly small ($<$ 1mm over 50 min). We always measure this height at the end of each calculation.

4.3.2. Influence of the Model Simplifications

4.3.2.1. Effects of the Viscosity Cut-Off η_0

We tested the influence of different η_0 on the plume dynamics, $\eta_0 = [10^8, 10^{10}, 10^{12}]$ Pa s. The choice of η_0 neither affects the onset time, nor the dynamic behaviour (fig. 4.3 A).

Table 4.1.: Shear thinning exponent n, consistency K_ν, yield stress σ_0, thermal expansivity α, onset time t_0, the thermal power P, height reached by viscosity minimum at plume head at for all numerical simulations h_y and respective yield parameter Y_0. Onset-time marked with * indicate that no plume develops even after that time.

#	σ_0 [Pa]	K_ν [Pa s^n]	n [−]	α [10^{-4}/K]	t_0 [min]	P [W]	h_y [cm]	Y_0 [−]	#	σ_0 [Pa]	K_ν [Pa s^n]	n [−]	α [10^{-4}/K]	t_0 [min]	P [W]	h_y [cm]	Y_0 [−]
1	0.0100	0.140	0.58	6.00	1.3550	1.709	-	2666.26	29	0.0630	1.403	0.58	4.78	77.2340	1.157	26.85	228.26
2	0.0100	1.000	0.58	4.78	2.3712	1.539	40.00	1912.83	30	0.0650	1.000	0.58	4.78	82.6539	1.16	30.63	221.81
3	0.0100	1.000	0.58	4.78	3.0487	1.215	40.00	1510.13	31	0.0650	1.000	0.50	4.78	108.3985	1.148	28.92	219.51
4	0.0100	1.403	0.58	6.00	1.3550	1.552	40.00	2421.31	32	0.0650	1.000	0.70	4.78	67.7491	1.18	37.22	225.64
5	0.0100	1.403	0.90	6.00	1.3550	1.682	40.00	2624.13	33	0.0650	1.403	0.58	4.78	90.7838	1.157	28.23	221.24
6	0.0200	1.000	0.58	4.78	5.7587	1.463	40.00	909.18	34	0.0650	1.403	0.50	4.78	131.4332	1.139	27.20	217.80
7	0.0200	1.403	0.58	4.78	5.4199	1.429	40.00	888.05	35	0.0650	1.403	0.70	4.78	71.8140	1.172	31.63	224.11
8	0.0200	1.403	0.58	6.00	4.4037	1.481	40.00	1155.28	36	0.0650	2.000	0.58	4.78	105.6886	1.15	26.16	219.90
9	0.0250	1.403	0.58	4.78	6.7749	1.449	31.63	720.39	37	0.0650	2.000	0.50	4.78	181.5675	1.122	26.16	214.54
10	0.0300	1.403	0.58	4.78	10.1624	1.380	27.85	571.74	38	0.0650	2.000	0.70	4.78	75.8790	1.165	28.92	222.77
11	0.0350	1.403	0.58	4.78	13.5498	1.341	24.95	476.21	39	0.0670	0.140	0.58	4.78	82.6539	1.158	40.00	214.82
12	0.0400	0.140	0.58	4.78	12.8723	1.346	-	418.28	40	0.0670	1.000	0.58	4.78	98.9137	1.148	32.62	212.96
13	0.0400	0.140	0.58	6.00	8.1299	1.426	-	556.18	41	0.0670	1.403	0.90	6.00	81.2989	1.156	40.00	269.18
14	0.0400	1.000	0.58	4.78	16.9373	1.317	23.9	409.255	42	0.0670	1.403	0.58	6.00	37.2620	1.227	23.5	285.71
15	0.0400	1.403	0.58	4.78	16.9373	1.308	22.67	406.43	43	0.0670	1.403	0.58	4.78	108.3985	1.145	29.61	212.41
16	0.0400	1.403	0.58	6.00	10.8399	1.367	27.2	533.17	44	0.0670	2.000	0.58	4.78	126.0133	1.144	27.54	212.22
17	0.0400	1.403	0.90	4.78	8.1299	1.427	40.00	443.41	45	0.0670	14.000	0.58	4.78	1400*	1.025	0	190.15
18	0.0500	1.000	0.58	4.78	30.4871	1.28	23.37	318.18	46	0.0675	1.403	0.58	4.78	113.8185	1.156	30.29	212.86
19	0.0500	1.403	0.58	4.78	33.8745	1.263	21.8	313.96	47	0.0680	1.403	0.58	4.78	120.5934	1.140	30.96	208.37
20	0.0600	1.000	0.58	4.78	55.5542	1.196	27.20	247.75	48	0.0700	1.000	0.58	4.78	131.4332	1.157	36.00	205.43
21	0.0600	1.000	0.50	4.78	73.1690	1.183	25.81	245.06	49	0.0700	1.000	0.50	4.78	170.7277	1.123	33.59	199.40
22	0.0600	1.000	0.70	4.78	46.0694	1.215	30.29	251.69	50	0.0700	1.000	0.70	4.78	113.8185	1.215	40.00	215.73
23	0.0600	1.403	0.58	4.78	62.3292	1.183	25.11	245.06	51	0.0700	1.403	0.58	4.78	146.3380	1.14	32.95	202.42
24	0.0600	1.403	0.50	4.78	89.4288	1.163	24.07	240.92	52	0.0700	1.403	0.50	4.78	222.0000	1.111	31.63	197.27
25	0.0600	1.403	0.70	4.78	48.7793	1.198	27.89	248.17	53	0.0700	1.403	0.70	4.78	117.8834	1.137	40.00	201.88
26	0.0600	2.000	0.58	4.78	73.1690	1.173	23.37	242.99	54	0.0700	2.000	0.58	4.78	166.6627	1.138	30.29	202.06
27	0.0600	2.000	0.50	4.78	108.3985	1.146	23.37	237.39	55	0.0700	2.000	0.50	4.78	319.7757	1.103	30.63	195.85
28	0.0600	2.000	0.70	4.78	51.4893	1.195	26.16	247.55	56	0.0700	2.000	0.70	4.78	121.9483	1.145	34.22	203.30

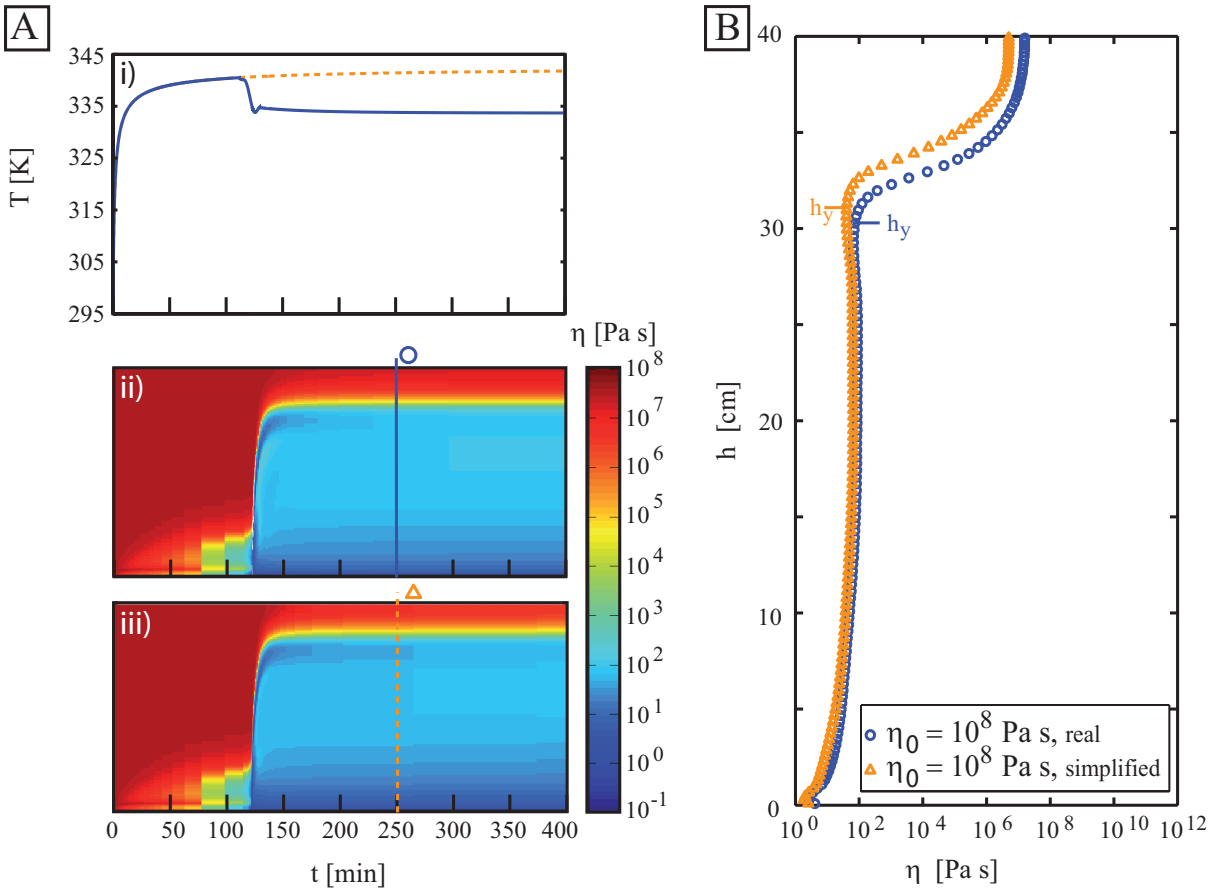

Figure 4.4.: Effect of real A: i) real solid blue and generalized dashed orange thermal history on the evolution of the plume. Spatiotemporal evolution for the viscosity of a vertical line at the plume axis ii) laboratory and iii) generalized temperature history of the heated patch. B: cross section of Aii) (blue circles) and Aiii) (orange triangles) at $t = 250\,\text{min}$.

The viscosity profile inside the plume remains the same (fig. 4.3 B), and only the unyielded structure above the plume ($h > h_y$) is influenced by the cut-off value. However the height where the plume stops, h_y, does not change for different cut-off values (see close up fig. 4.3). This shows that the regularization has no significant influence on the plume's behaviour. Given this result, all simulations were run with the same viscosity cut-off value of $\eta_0 = 10^8\,\text{Pa s}$.

4.3.2.2. Dependence on the Thermal History

The laboratory experiments (*Davaille et al. [2013]*) have a constant heating power, which leads to a temperature drop in the copper plate when heat is suddenly taken away by the plume lift off (fig. 4.4 A i) solid blue line). However, in the present paper we intend to vary the rheological parameters. An increase in the yield stress will then lead to an increase in the onset time. If the onset time lies beyond the onset time of the laboratory experiments, a temperature drop in the heated patch would influence (delay or suppress) the onset time or might affect the dynamics of a plume that starts before the laboratory plume. Therefore we generalize the heating history by smooth prolongation of the thermal history curve prior to the onset (cf. fig. 4.4 A i) dashed orange line). In the case of the real temperature history the unyielded region is slightly larger, i.e. h_y is smaller, than for the generalized heating. As the supply of heat drops slightly in the laboratory case, the plume is less buoyant and rises less high. However, the difference is rather small, 3% of the absolute value (cf. cross section at 250 min fig. 4.4 B). Keeping this in mind we will use in most of the runs the simplified heating history as shown by the dashed orange line in fig. 4.4 A i).

4.3.3. Comparison with Laboratory Experiments

The uncertainties of the laboratory experiments, e.g. an error of 30 % (*Davaille et al. [2013]*) on the yield stress, make it difficult to match the exact conditions and to reproduce a series of experiments. As we will show in detail later, the system is very sensitive to small changes, not only in yield stress, but also in shear thinning exponent or in consistency. However, we will show here that the basic characteristics of laboratory experiments, e.g. a finger-like instability and a strong dependence of the onset time on the yield parameter Y_0 (*Davaille et al. [2013]*), are well captured by our numerical model. Furthermore, in a new set of laboratory experiments with a larger fluid height, we observe the persistance of unyielded regions even after the plume is established. *Davaille et al. [2013]* had not been able to observe this phenomenon, due to the smaller fluid height. This will allow us to examine in more detail how each rheological property affects the dynamics of the system.

4.3.3.1. Onset and Evolution

Fig. 4.5 shows the dependence of the onset time on the yield parameter Y_0, for the numerical simulations, the flush mounted experiments and the bottom mounted experiments (*Davaille et al. [2013]*). The onset-time of the plume strongly depends on the yield parameter Y_0. The numerical simulations show a good agreement with the results obtained with the modified setup, where the heating is flush mounted. The critical value for the flush mounted experiments and for the numerical simulations is $Y_c \approx 165 \pm 25$.

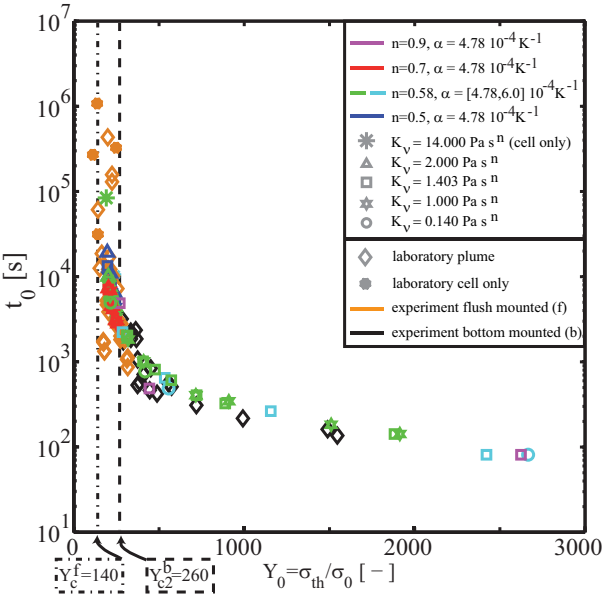

Figure 4.5: Onset time dependence on the non-dimensional yield parameter Y_0 which compares the buoyancy induced thermal stress to the yield stress. Diamonds are plumes obtained from laboratory experiments including those of *Davaille et al. [2013]* (black) and those obtained with the flush mounted heater (orange). Orange octagons: laboratory experiments that exhibit only a cell until the depicted time. All other symbols: Numerical simulations, colours indicate different n, while different symbols indicate different K_ν.

The dash-dotted line in Fig. 4.5 marks the lower limit at $Y_0 = 140$, and the error can be explained with the uncertainties in the laboratory measurements (10 % on the thermal Power P and 30 % on the yield stress σ_0). However, the critical value for the flush mounted experiments is well below the value for the bottom mounted heating determined by *Davaille et al. [2013]* of $Y_{c2} = 260$. We attribute this discrepancy to the different heater shapes, which will change the local stress distribution. The plot suggests that n and K_ν also influence the onset time, however this will be discussed later. Globally, the plot shows that the onset time approaches two asymptotical values, depending on the yield stress. For low yield parameter, i.e. when the yield stress is important compared to the thermally induced stresses, the onset time is increasing rapidly with decreasing Y_0. On the other end, for high yield parameter, i.e. low yield stresses, the onset time approaches a finite limit. This is to be expected as the system turns towards the purely shear thinning or Newtonian case.

In Fig. 4.6 the typical spatiotemporal evolutions of a plume for both laboratory and numerical simulations, are compared. Fig. 4.6 A presents the time evolution of the heated patch for experiment (black) and simulation (grey), in the case where we used the real temperature history. Fig. 4.6 C shows a typical snapshot of the plume in the laboratory experiments. The white broad lines outlined in colour are isotherms (blue dash dotted: 23.9 °C, yellow dotted: 31.1 °C, red dashed: 39.9 °C) and thin white lines correspond to particle trajectories. Therefore a horizontal line indicates a particle at rest and white streaks upwards and towards the right are particles moving upwards along the axis. Fig. 4.6 D shows the vertical viscosity profile on the plume axis for the numerical simulations where the viscosity increases from dark blue to dark red. Black lines indicate the position

of the same isotherms as visualized in the laboratory, where temperature is increasing from inside (bottom) to outside (top).

The thermal power in the laboratory is $P = 1.85 \pm 0.185\,\mathrm{W}$, the yield stress is determined to be $\sigma_0 = 0.09 \pm 0.015\,\mathrm{Pa}$, the consistency $K_\nu = 1.403 \pm 0.2\,\mathrm{Pa\,s^n}$ and the shear thinning exponent is determined to be $n = 0.58 \pm 0.01$. The measurements have been done using a Physica MCR501-rheometer (Anton Paar, www.anton-paar.com) with a coaxial cylinder geometry (CC27).

We find a good agreement of the onset-time derived from the numerical simulation and the laboratory experiment ($t_0 = 119.9\,\mathrm{min}$ in the laboratory, $t_0 = 120.59\,\mathrm{min}$ in the simulations, $t = 120\,\mathrm{min}$ indicated by the green dashed line) with the parameter-combination $P = 1.14\,\mathrm{W}$, $\sigma_0 = 0.068\,\mathrm{Pa}$, $K_\nu = 1.403\,\mathrm{Pa\,s^n}$ and $n = 0.58$. The thermal properties are the same with small errors on the values for the experiments. The thermal expansivity is $\alpha = 4.78 \pm 0.01\,\mathrm{K^{-1}}$ and the thermal conductivity is $k = 0.435 \pm 0.02\,\mathrm{W\,/\,m\,K}$. Therefore we can calculate the yield parameter for the laboratory experiments $Y_0 = 266.86 \pm 71.09$ and for the numerical simulations $Y_0 = 208.36$. The value for the simulations is well within the error range of the laboratory experiments, explaining the good agreement of the onset times.

However, a match of both onset times does not necessarily imply an identical behaviour of the developping instability (fig. 4.6). This is most evident for the isotherms, which, for the simulations, propagate much higher at the onset than in the experiment. There are also similarities: the upper part of the box remains unyielded through time, as indicated by the green arrows. In the experiments this can be seen by following the particles in the upper part of the box. They describe a horizontal line, i.e. the particles are not moving (fig. 4.6 B). In the numerical simulations the very high viscosity (dark red regions in the figure) indicates that shear rate vanishes and that the fluid is not moving. The maximum shear rate at the plume head is represented by the low viscosity in this region as highlighted by the horizontal black dashed line. Above this line viscosity increases rapidly.

4.3.3.2. The Plume Morphology

Fig. 4.7 shows that small shear rates are already present before the plume evolves, while the isotherms (black lines) still have a circular shape. A small cell is convecting around the heater and as the shear rate increases, this cell evolves into a plume. This plume then exhibits locally very strong deformation, which is localized on the edges of the thermal anomaly. The deformation is much weaker inside (difference of two orders of magnitude). Above the plume, the fluid exhibits unyielded regions. The inner structure of the thermal anomaly develops as a plume with a small head (A ii) and B iii)) whereas the outer isotherm looks more like a finger. Once the small head is lost, only the stem remains midway in the tank.

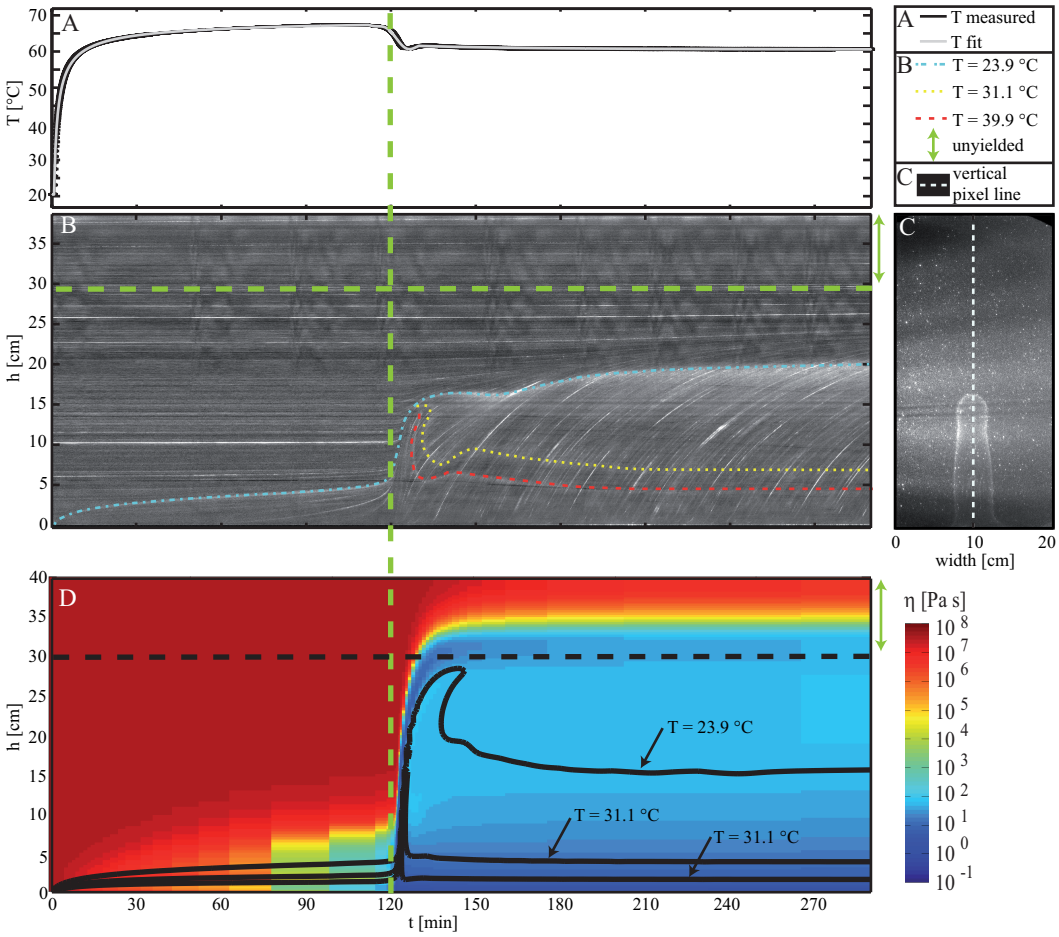

Figure 4.6.: A: Evolution of the heating for the laboratory experiments (black line) and the numerical simulation (grey line) through time. B: Spatiotemporal evolution of a vertical pixel line (vertical white dashed line in C) through time. White lines show particles, coloured lines highlight the isotherms at 23.9 °C (blue dash dotted), 31.1 °C (yellow dotted) and 39.9 °C (red dashed). C: Snapshot from a laboratory experiment at $t = 146$ min, the white dashed line marks plume axis. D: Spatiotemporal evolution of the viscosity at the plume axis (background colour) and isotherms (black lines). The vertical green dashed line indicates the onset time, which is about the same (laboratory experiment: $t_0 = 119.9$ min, numerical simulation $t_0 = 120.59$ min) for simulation and experiment. The horizontal green line marks the unyielded region for the laboratory experiment; the width of this region for experiment and simulation is given by the green arrows.

The instability in the simulations develops just like the instability in the experiments. The dependence of the onset time on the yield parameter is the same as in the laboratory experiments. The thermal anomaly looks like a finger and the instability exhibits strong

deformation at the edges of the thermal anomaly and a pseudo-plug flow inside the thermal instability, as observed in the laboratory. Therefore we conclude that the purely viscous regularized Herschel-Bulkley model is a sufficient description of the fluid and suitable for studying numerically the development of thermal plumes in Herschel-Bulkley fluids like Carbopol.

4.4. Effects of Rheological Parameters on the Dynamics

The laboratory experiments of *Davaille et al. [2013]* show a strong dependence of the onset time and evolution of the plume on the yield stress. A closer look at different flow curves (fig. 4.8) reveals that a change of the shear thinning exponent (fig. 4.8 A) and/or the consistency (fig. 4.8 B) might also affect the system, as those changes affect the effective viscosity. The flattening of the viscosity curve (fig. 4.8 A and B i)) and the deviation from the stress plateau (fig. 4.8 A and B ii)) for shear rates $\dot{\gamma} < 10^{-8}\,\mathrm{s}^{-1}$ are due to the viscosity cut-off η_0. The uncertainties on the determination of the rheological parameters make it difficult to study the effect of small changes in the laboratory. We therefore examine numerically how small changes for all rheological parameters (σ_0, K_ν and n) influence the development of the plume.

In order to investigate the effect of the yield stress on the plume's dynamics we varied σ_0 between 0.01 Pa and 0.07 Pa for constant $K_\nu = 1.403\,\mathrm{Pa\,s^n}$ and $n = 0.58$. With increasing yield stress (fig. 4.9 A) from i) $\sigma_0 = 0.035\,\mathrm{Pa}$ over ii) $\sigma_0 = 0.04\,\mathrm{Pa}$ to iii) $\sigma_0 = 0.06\,\mathrm{Pa}$, the onset time increases, as the yield parameter diminishes. At a given power P it then becomes increasingly difficult for the hot pocket to overcome the yield stress and to penetrate the surrounding fluid. Increasing the yield stress from $\sigma_0 = 0.035\,\mathrm{Pa}$ to $\sigma_0 = 0.04\,\mathrm{Pa}$ induces a decrease of h_y. As the plume cools down on its way up by heat diffusion (cf. fig. 4.10 isotherms), its thermal buoyancy decreases until it cannot anymore overcome the yield stress. h_y should therefore depend on the initial buoyancy and the yield stress. At a given P, we expect h_y to decrease with increasing σ_0, as is observed. However, a further increase of the yield stress yields again a higher h_y, which may appear surprising at first. Yet this could be explained by the strong increase of the onset time when approaching the critical yield parameter, which allows the plume to accumulate more buoyancy before rising.

The increase of height h_y with increasing yield stress can also be observed in the laboratory experiments. In terms of the yield parameter Y_0 an increase in the yield stress is comparable to a decrease of the thermal power P. Fig. 4.10 shows the spatiotemporal evolution of the pixel line on the plume axis for two laboratory experiments with the same fluid, but with different thermal power P. The experiments show that, like in the numerical simulation, a decrease in Y_0 (obtained by decreasing P in the experiments and increasing σ_0 in the simulations) leads to an increase of h_y.

We furthermore tested numerically that we obtain the same behaviour by applying a

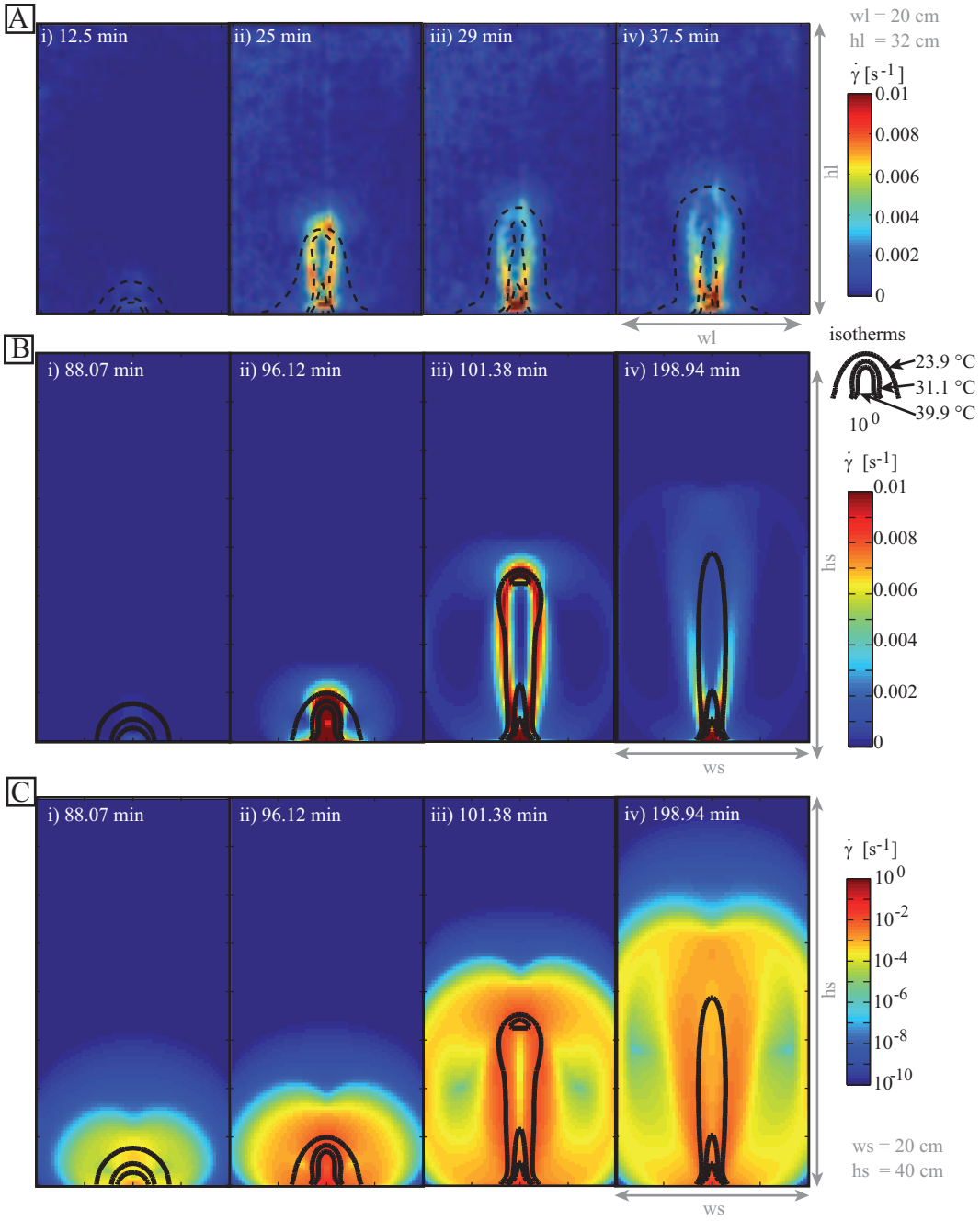

Figure 4.7.: Morphology of the deformation (background colour) and the temperature field as indicated by the isotherms (black lines, temperature increases from the inside to the outside, isotherms at 39.9 °C, 31.1 °C and 23.9 °C). A: Laboratory experiment, B: Numerical simulation. A and B are shown for the same shear rate range (colourbar at the side); C: Numerical simulation for a larger shear rate.

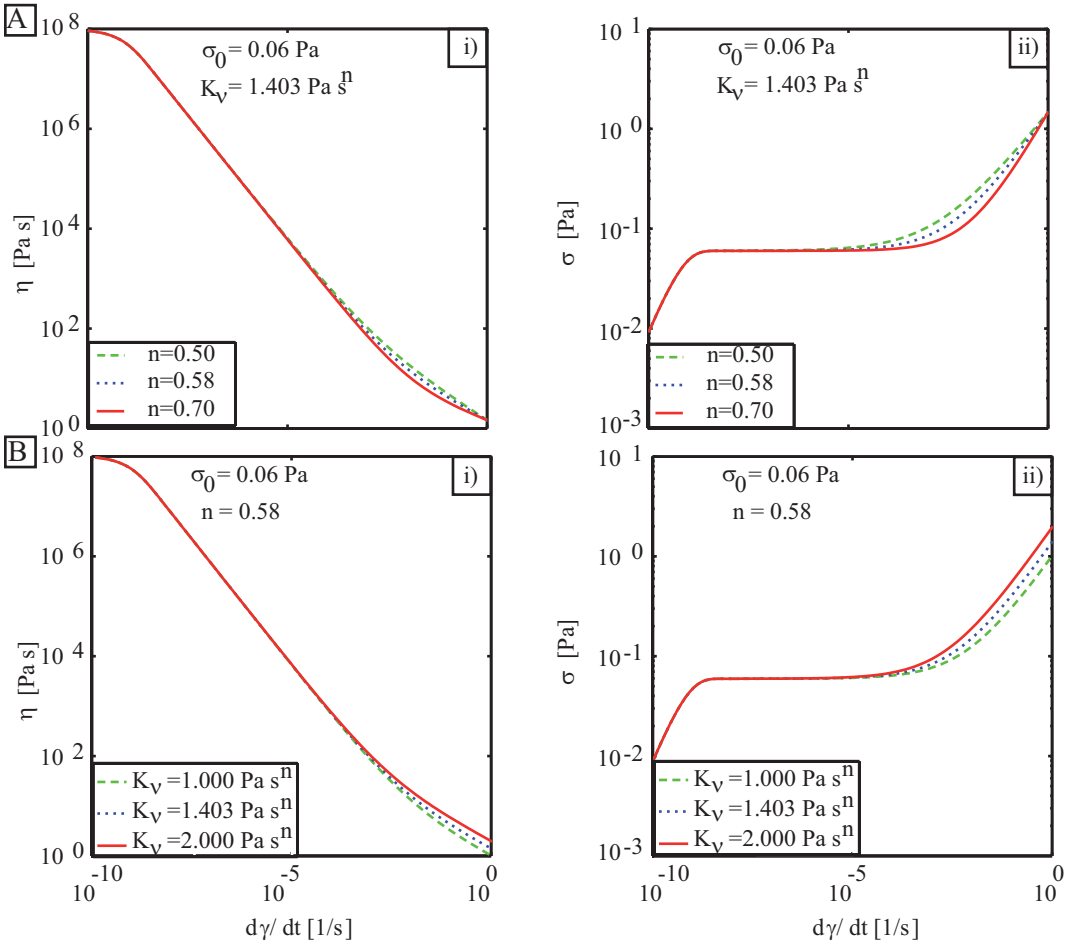

Figure 4.8.: Flow curves for different parameter combinations, i) viscosity versus shear rate and ii) stress versus shear rate. A: constant $\sigma_0 = 0.06\,\mathrm{Pa}$ and $K_\nu = 1.403\,\mathrm{Pa\,s^n}$ and varying shear thinning exponent $n = [0.50, 0.58, 0.70]$. B: constant $\sigma_0 = 0.06\,\mathrm{Pa}$ and $n = 0.58$ and varying consistency $K_\nu = [1.000, 1.403, 2.000]\,\mathrm{Pa\,s^n}$.

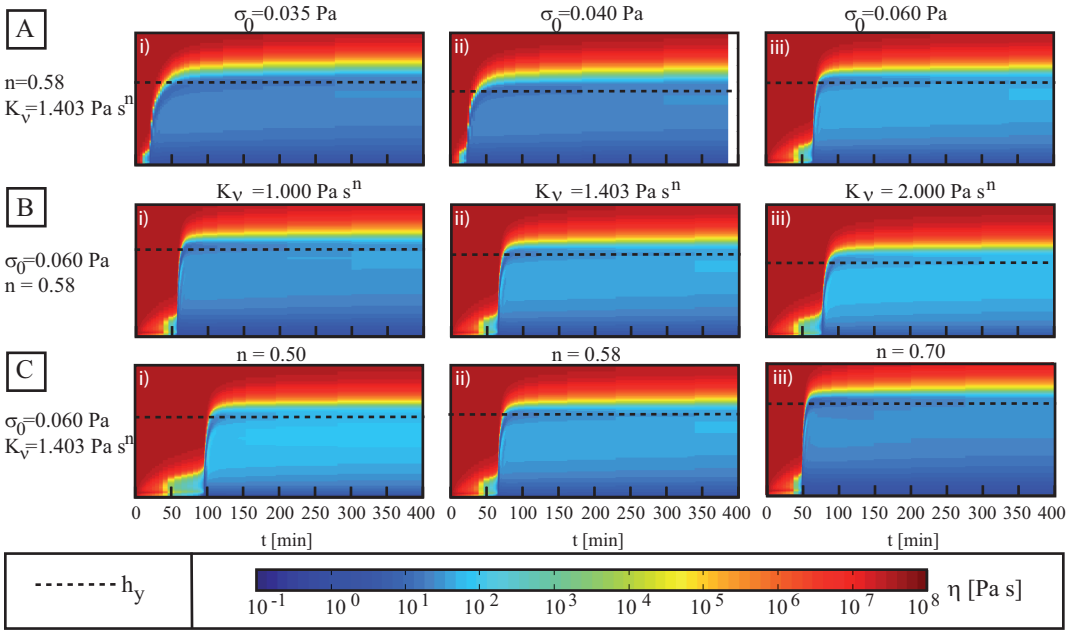

Figure 4.9.: Spatiotemporal evolution for the viscosity of a vertical line at the plume axis through time for A: increasing yield stress at constant $K_\nu = 1.403\,\mathrm{Pa\,s^n}$ and $n = 0.50$ B: increasing consistency at constant $\sigma_0 = 0.060\,\mathrm{Pa}$ and $n = 0.58$ and C: increasing shear thinning exponent at constant $\sigma_0 = 0.060\,\mathrm{Pa}$ and $K_\nu = 1.403\,\mathrm{Pa\,s^n}$. Horizontal black dashed lines mark h_y.

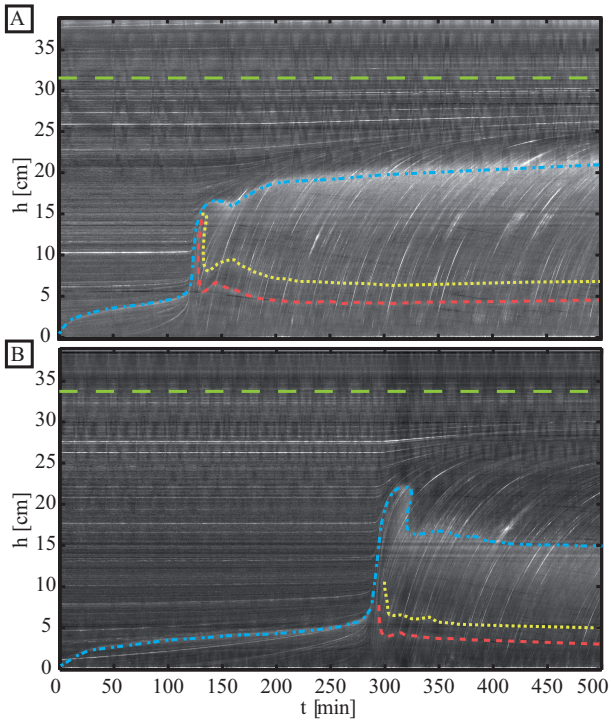

Figure 4.10: Spatiotemporal evolution of a vertical pixel-line at the plume axis for two laboratory experiments in the same fluid, with different thermal power applied. A: $P = 1.85\,\mathrm{W}$, B: $P = 1.50\,\mathrm{W}$. Coloured lines highlight isotherms, colour and linestyle convention as in fig. 4.6 B. Green lines indicate the transition to unyielded region.

constant temperature. So, whatever the details of the heater history are (constant power in the laboratory experiments or simplified temperature history in the simulations or constant temperature) h_y is not a monotonous function of Y_0, but with increasing Y_0, h_y first decreases and then increases again.

The effect of the increase of the consistency is depicted in fig. 4.9 B and increases from i) $K_\nu = 1.0\,\mathrm{Pa\,s^n}$ to iii) $K_\nu = 2.0\,\mathrm{Pa\,s^n}$ at $\sigma_0 = 0.06\,\mathrm{Pa}$ and $n = 0.58$. The flow curve for the viscosity (fig. 4.8 B i)) shows that a fluid with a high consistency exhibits higher viscosities at constant shear rate. As a result, we observe that the onset time changes only slightly (compared to the effect of a change in the yield stress), as the consistency increases. On the other hand h_y decreases with increasing K_ν by roughly 15 % from $K_\nu = 1.0\,\mathrm{Pa\,s^n}$ to $K_\nu = 2.0\,\mathrm{Pa\,s^n}$. Inside the instability the viscosity increases with increasing K_ν. With constant $\sigma_0 = 0.06\,\mathrm{Pa}$ and $K_\nu = 1.403\,\mathrm{Pa\,s^n}$ an increase of the shear thinning exponent induces lower viscosities for a given shear rate, fig. 4.8 A i). Therefore, the onset time decreases (fig. 4.9 C) when n increases from i) $n = 0.5$ to iii) $n = 0.7$. Furthermore this decrease in the effective viscosity also results in higher h_y.

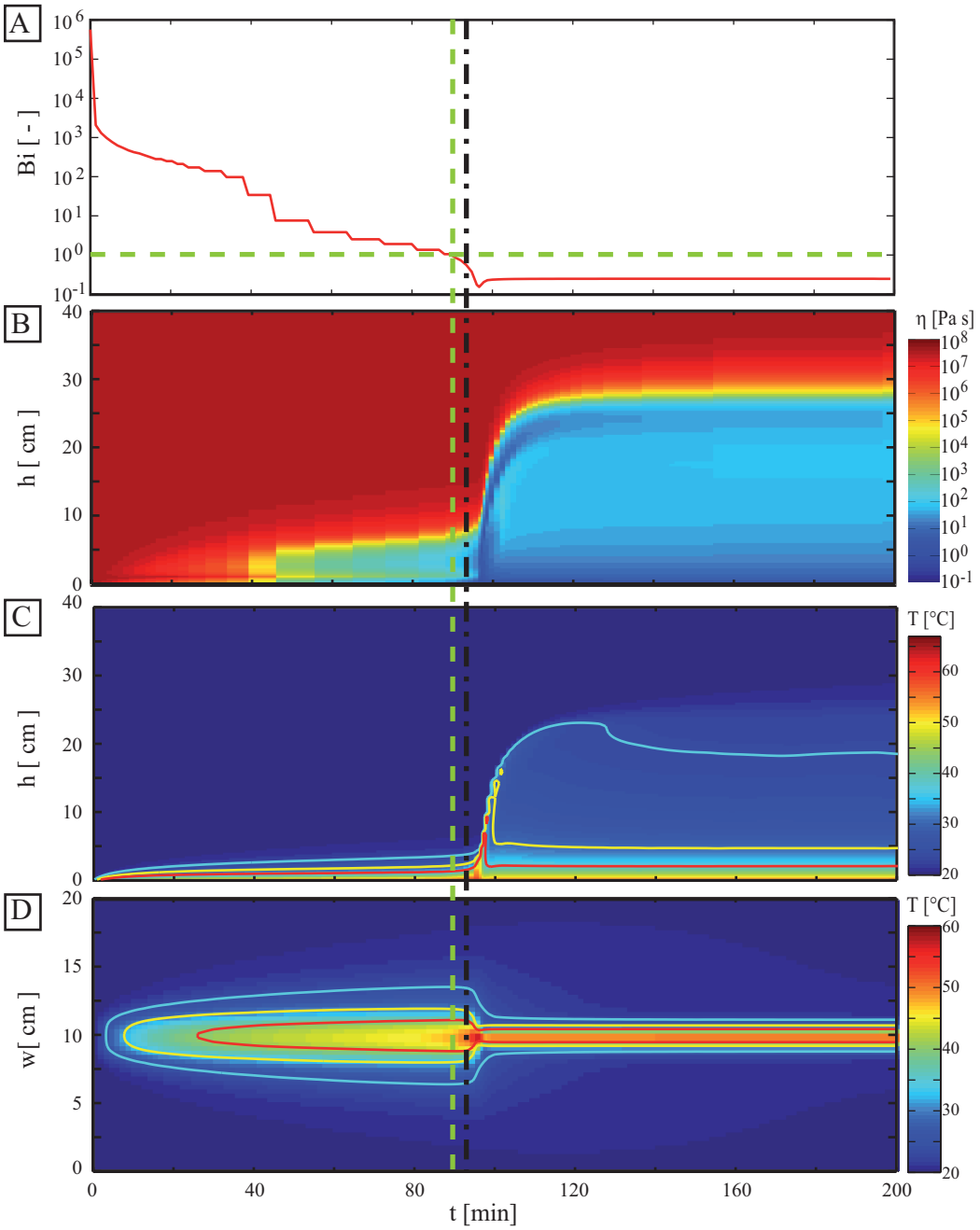

Figure 4.11.: Different temporal evolutions for simulation 24, cf. table 4.1. A: evolution of the Bingham number $Bi = \frac{\sigma_0}{K_\nu \dot{\gamma}_{max}^n}$ where $\dot{\gamma}_{max}$ is the maximum shear rate evaluated at each time step. The vertical green line marks $Bi = 1$. B: Spatiotemporal evolution of the viscosity at the plume axis. C: Spatiotemporal evolution of the temperature at the plume axis. Red, yellow and blue lines indicate isotherms at $T = 39.9\,°\mathrm{C}$, $T = 31.1\,°\mathrm{C}$ and $T = 23.9\,°\mathrm{C}$ respectively. D: Spatiotemporal evolution of the temperature of a horizontal line through the thermal boundary layer and the plume axis. The vertical green line indicates when the Bingham number in A becomes one, the vertical black dash-dotted line indicates when the $T = 39.9\,°\mathrm{C}$-isotherm in D starts to deform.

4.5. Discussion

4.5.1. The Onset of the Plume

As we saw in the previous section, the onset time does not only depend on the yield parameter, but also on the consistency and the shear thinning exponent. A parameter comparing the yield stress to the viscous stresses is the Bingham number, which is for a Herschel-Bulkley fluid defined as

$$Bi = \frac{\sigma_0}{K_\nu \dot{\gamma}^n}. \tag{4.10}$$

We calculate this parameter using the maximum shear rate at each time step and then track the evolution of Bi (fig. 4.11 A). Fig. 4.11 B shows the evolution of the viscosity on the plume axis. A comparison of both plots shows that the Bingham number value becomes $Bi = 1$ right prior to the take off of the plume. We can furthermore compare this to the evolution of the temperature field; Fig. 4.11 C shows the temporal evolution of a vertical pixel line at the plume axis and Fig. 4.11 D a horizontal pixel-line cutting the thermal boundary layer through the plume axis. The grey dotted line indicates the onset time as determined in the laboratory experiments (*Davaille et al. [2013]*), where the necking of the isotherms as seen in fig. 4.11 D has been used as a criterion for the onset. The state at which $Bi = 1$ occurs slightly before the onset as determined by the deformation of the isotherms in (fig. 4.11 D). However, when we plot the onset time as determined from the isotherms versus the onset time determined by the criterion $Bi = 1$ for different rheologies (fig. 4.13) the data collapse on a straight line of slope one. Therefore, the Bingham number criterion is suitable to determine the onset time. Additionally, this method provides a more accurate determination of the onset time, since the other methods depend on the choice of the isotherm (cf. fig. 4.11 D: the inner (red) isotherm deforms earlier than the outer (blue) isotherm).

$Bi = 1$ at onset gives a characteristic scale for the shear rate that has to be overcome to generate a plume. This critical shear rate is then written as

$$\dot{\gamma}_{cr} = \left(\frac{\sigma_0}{K_\nu}\right)^{1/n}. \tag{4.11}$$

This further implies that at onset the local stresses fulfill the following criterion

$$\sigma = \sigma_0 + K_\nu \left(\left(\frac{\sigma_0}{K_\nu}\right)^{1/n}\right)^n = 2\,\sigma_0. \tag{4.12}$$

The experiments of *Davaille et al. [2013]* indicate that the critical yield number Ψ as defined for bubbles to rise (*Dubash and Frigaard [2004, 2007]*) or spheres to sink (*Beris et al. [1985]*, *Tabuteau et al. [2007]*) in a yield stress fluid is also applicable for the onset

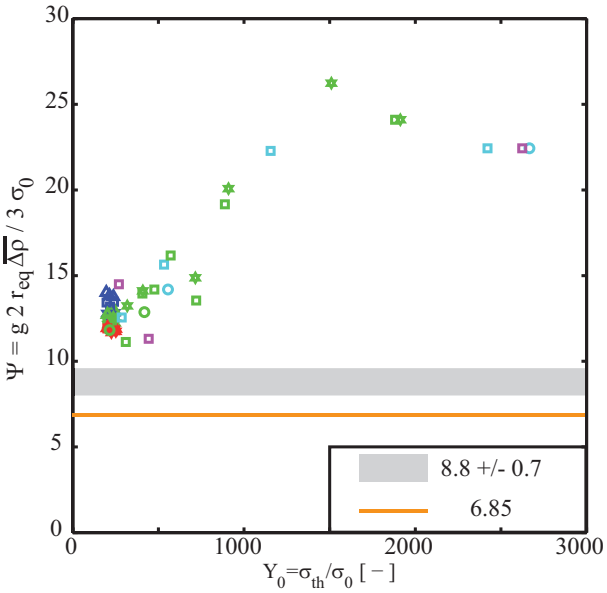

Figure 4.12: Color convention as fig. 4.5. Yield number Ψ with mean density difference $\overline{\Delta\rho}$ between mean density of hot pocket with radius r_{eq} and ambient fluid at plume onset versus yield parameter. Orange line indicates $\Psi = 6.85$ (*Beris et al. [1985]*, *Dubash and Frigaard [2004, 2007]*, *Tabuteau et al. [2007]*) and grey bar corresponds to $\Psi = 8.8 \pm 0.7$ (*Davaille et al. [2013]*).

of the plume. The data range accessible from the simulations provides a much cleaner way to determine this parameter, than by the laboratory experiments. Similar to *Davaille et al. [2013]* we determine the volume of the fluid with a temperature excess $0.1\,\Delta T$ at the onset, where ΔT is the temperature difference between the heated patch and the ambient fluid. We then calculate the equivalent radius of a sphere with the same volume r_{eq} and determine its mean buoyancy, which is derived via the temperature difference of the mean temperature of the hot pocket and the ambient fluid $\overline{\Delta T}$ as $\overline{\Delta\,\rho} = \alpha\,\rho\,\overline{\Delta T}$. Substituting these values into the definition of *Dubash and Frigaard [2007]*

$$\Psi = \frac{g\,d\,\Delta\rho}{3\,\sigma_0} \tag{4.13}$$

with $d = 2\,r_{eq}$ yields values well above, for our simulations 1.6 to 3.8 times, the critical value $\Psi_c = 6.85$ given by these authors (cf. fig. 4.12). This indicates that $\Psi \geq 6.85$ is a necessary but not sufficient criterion, as at the same time the Bingham number also needs to be supercritical ($Bi < 1$).

Plotting the maximum velocity versus the product of the equivalent radius r_{eq} and the maximum shear rate (fig. 4.14) yields a good agreement between those two velocities. Thus, treating the thermal anomaly as a hot pocket of radius r_{eq} rising through the fluid is a good approximation.

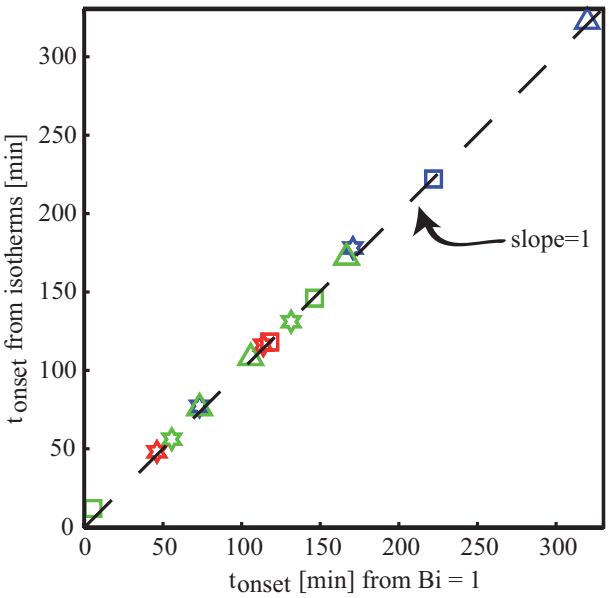

Figure 4.13: Onset time determined from spatiotemporal evolution of a horizontal pixel line of the temperature field in the thermal boundary layer versus onset time determined from the criterion $Bi = 1$. Colour convention as in fig. 4.5.

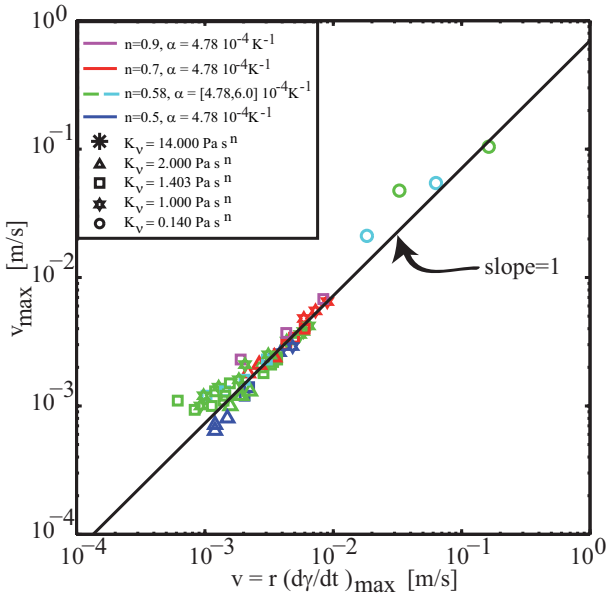

Figure 4.14: Maximum velocity v_{max} during plume uplift versus radius of hot pocket times maximum shear rate during plume uplift. The radius has been evaluated from the size of the thermal boundary layer at the onset of the plume, as described in *Davaille et al. [2013]*. The black line indicates a slope equal to one.

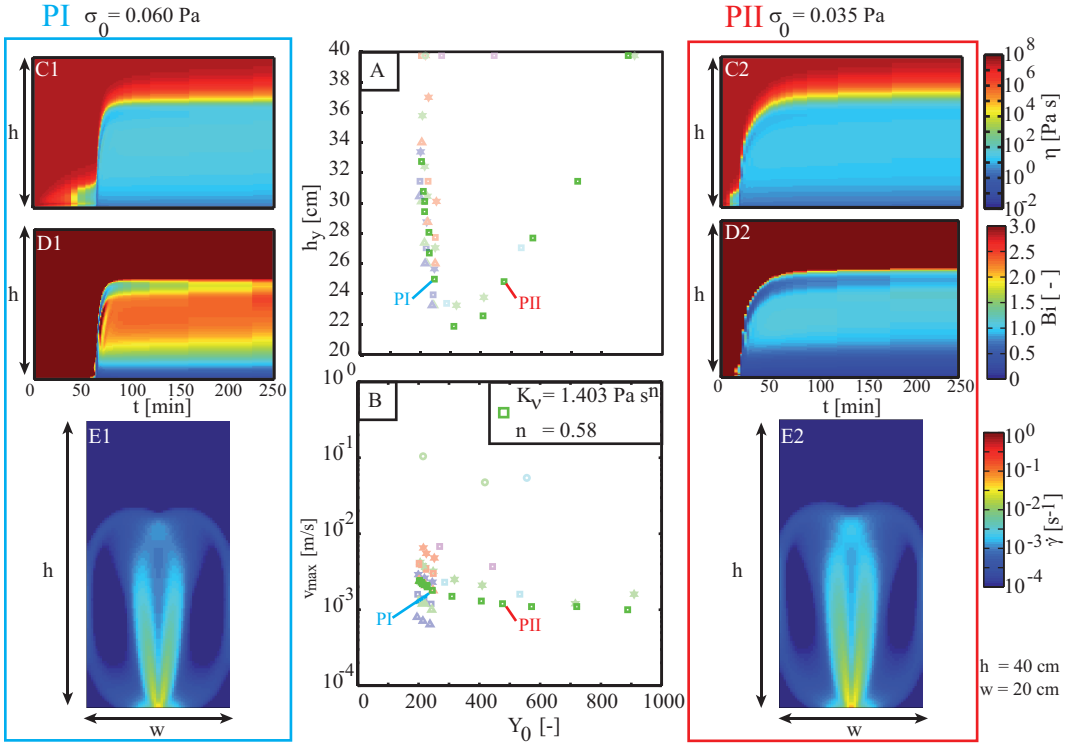

Figure 4.15.: Height h_y (A) and maximum velocity (B) versus yield parameter. Dark green boxes show simulations for $K_\nu = 1.403\,\mathrm{Pa\,s^n}$ and $n = 0.58$, transparent values shown for comparison with colour convention as in fig. 4.5. C: spatiotemporal evolution of the viscosity at plume axis. D: spatiotemporal evolution of the Bingham number at the plume axis. E: vertical cross section of the shear rate at the plume axis, shear rate limited from $\dot{\gamma} = 10^{-4}\,\mathrm{s^{-1}}$ to $\dot{\gamma} = 10^{0}\,\mathrm{s^{-1}}$ to highlight the different morphologies.

4.5.2. Height where the Plume Stops

In section 4.4 we illustrated the effect of the rheological properties of the fluid on the evolution of the thermal instability and found that all parameters strongly influence the height h_y where the plume stops. Fig. 4.15 summarizes these results for the simulations. Fig. 4.15 A therefore assembles h_y for all the simulations with $Y_0 < 1000$. For higher Y_0 the plume always arrives at the surface. The highlighted series (green square, $K_\nu = 1.403\,\mathrm{Pa\,s^n}$, $n = 0.58$ and varying σ_0) will now be discussed. With increasing yield parameter Y_0, we can observe that h_y first decreases and then increases again. We therefore compare two simulations that stop at approximately the same height but are on either branch of that curve (cf. points marked as PI and PII in fig. 4.15). For each simulation we visualized the evolution of the viscosity on the plume axis through time (fig. 4.15 C1 and C2). The plume at lower yield parameter, PI with $Y_0 = 245.1$, starts much later than PII ($Y_0 = 476.2$). Once it starts, PI is much faster than PII, as shown by the maximum velocity (fig. 4.15 B), which is 1.5 times higher for PI than for PII. This can be explained by PI having accumulated much more buoyancy than PII, as it was heated for a longer time. In fig. 4.14 we can see that a plume with a higher shear thinning exponent (comparing red points with $n = 0.7$ to blue points with $n = 0.5$) rises much faster. Fig. 4.15 A and B show that these faster plumes also rise higher (higher h_y). However this does not explain why the plume stops and how the transition from the left to the right branch of fig. 4.15 takes place.

A plume rises if it is buoyant enough, and as we could see at the onset, the Bingham number has to be supercritical ($Bi < 1$). We therefore calculate in a first step the Bingham number along the plume axis through time (fig. 4.15 D) using the local shear rates and the respective fluid parameters. Comparing this evolution for each fluid shows that the Bingham number for PI becomes subcritical ($Bi > 1$) at the plume head as the plume stops. On the other end PII stops even though its Bingham number is still supercritical. In a second step we now calculate the local yield number Ψ, with the maximum temperature difference between head of the plume and ambient fluid and r_{eq} as determined for the onset. We find that as PII stops the yield number becomes $\Psi = 5.124$, which is below the critical value of $\Psi = 6.85$ given by *Beris et al. [1985]*, *Dubash and Frigaard [2004, 2007]*, *Tabuteau et al. [2007]* and also the one determined experimentally for the thermal instability in Carbopol by *Davaille et al. [2013]*.

If we do this analysis for all data points, we find simulations in which the Bingham number is already subcritical while the yield number Ψ is still supercritical and vice versa. This indicates that, as soon as Bi or Ψ become subcritical, the plume stops rising. The critical yield number is $\Psi_c = 5 \pm 1.2$. This uncertainty is due to the fact that we are not saving every field at every time step.

We then determined for each simulation, which parameter becomes subcritical first, i.e. whether it is the Bingham or the yield number that causes the plume to stop, and the time t_s when the respective parameter becomes subcritical. At t_s we now determined

the value of the other parameter, which is still super critical at this time. The results are plotted against the yield parameter Y_0 (fig. 4.16) where the filled symbols show the yield number Ψ (when the Bingham number becomes subcritical) and the open symbols the Bingham number (when the yield number becomes subcritical).

The plot (fig. 4.16) is divided into two parts, where separation occurs at $Y_0 = Y_{0c} \approx 300$, corresponding to the minimum observed in fig. 4.15 A. Approaching $Y_{0c} = 300$ the yield number approaches the critical value ($\Psi \rightarrow \Psi_c$) and the Bingham number $Bi \rightarrow Bi = 1$.

Besides the differences for h_y we can observe that the morphology of the plume changes from the left to the right branch (fig. 4.15 E). On the left branch, where the dynamics are dominated by the Bingham number, the strongest deformation occurs at the edges of the instability. Around the plume axis, deformation is low ($\dot{\gamma} < 10^{-3}\,\mathrm{s}^{-1}$) and inside the instability as well (fig. 4.15 D1). The transition from the edges of the instability towards the inside is rather sharp, compared with (fig. 4.15 D2 and fig. 4.15 E2) PII on the right branch, where it is more smeared out. For PII the deformation pattern resembles much more the pattern observed in a Newtonian or purely shear thinning fluid.

4.6. Conclusions

We performed a systematic numerical study on the influence of the rheological properties in a regularized Herschel-Bulkley fluid on the development of thermal instabilities produced by a small heated patch. The comparison with laboratory experiments shows that the purely viscous description of *de Souza Mendes and Dutra [2004]* is adequate to describe the plume onset and its development. In agreement with *Davaille et al. [2013]*, we find that the yield parameter $Y_0 = \alpha\,\rho\,g\,P\,/\,k\,\sigma_0$ is the key external parameter to describe the transition from a slowly convecting hot cell around the heater towards a rising plume. Its critical value depends on the heater geometry and is $Y_{0c} = 165 \pm 25$ for a heater flush-mounted on the bottom of the tank. In addition, the determination of the 3D temperature, velocity, shear stresses and viscosity fields allows us to show that there are two necessary local conditions for a plume to take off and continue to rise. First, the local buoyancy of the hot pocket of fluid should be greater than the yield stress (which implies that $\Psi = \Delta\rho\,g\,2\,r_{eq}\,/\,3\,\sigma_0$, $\Psi_c = 5 \pm 1.2$). Second, the Bingham number, which compares the yield stress to the viscous stresses, $Bi = \sigma_0\,/\,K_\nu\,\dot{\gamma}^n$, should be smaller than 1.0. This implies that the local shear rate should be greater than a characteristic shear rate scale that only depends on the rheological properties of the fluid. As soon as $\Psi < \Psi_c$ or $Bi > 1$, the plume stops its upwards progression. Hot material will continue to rise from the bottom of the tank but it will spread under an unyielded, high viscosity region at the top of the box. Further work is now under way to characterize plume dynamics in steady state.

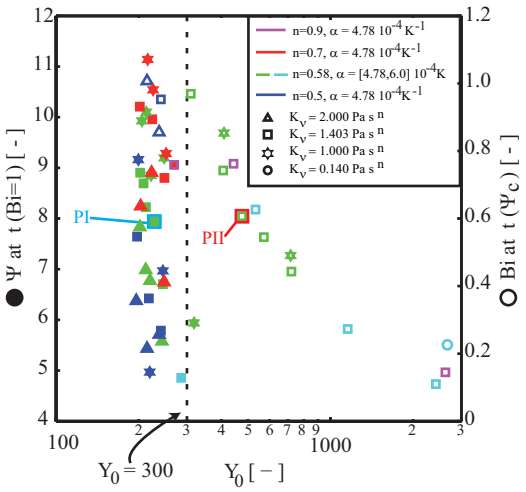

Figure 4.16: Yield number ($\Psi = \Delta\rho\, g\, 2\, r_{eq}/3\sigma_0$, filled symbols) at the time when, at the plume head, the Bingham number passes $Bi = 1$ and Bingham number (empty symbols) at the time when the yield number passes critical value $\Psi_c = 5 \pm 1.2$ versus yield parameter ($Y_0 = \alpha\, \rho\, g\, P/k\, \sigma_0$). For low yield parameter ($Y_0 < 300$) the Bingham number is the parameter that evokes a stopping of the plume, while Ψ is still supercritical. For higher yield parameter ($Y_0 > 300$) the stopping of the plume is caused by a loss of sufficient buoyancy, therefore Ψ becomes subcritical, while the Bingham number is still super critical ($Bi < 1$).

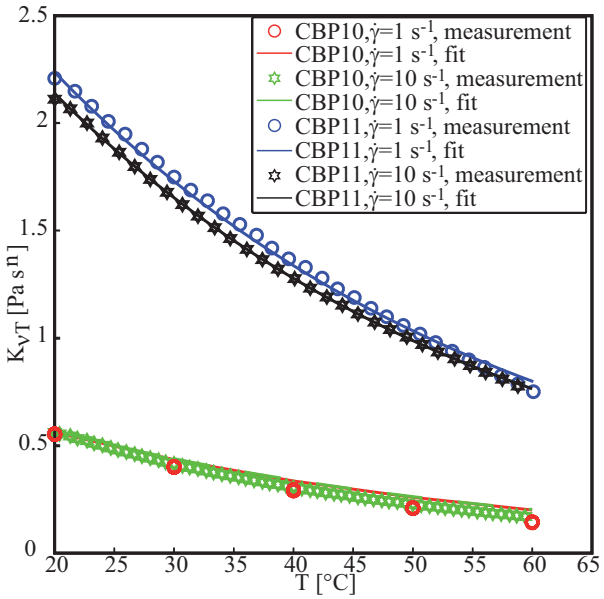

Figure 4.17: Dependence of consistency $K_{\nu T}$ on temperature T. Rheological properties measured in flow test for CBP10: $\sigma_0 = 0.018\,\mathrm{Pa}$, $K_\nu = 0.75\,\mathrm{Pa\,s^n}$, $n = 0.62$ and for CBP11: $\sigma_0 = 0.1\,\mathrm{Pa}$, $K_\nu = 1.5\,\mathrm{Pa\,s^n}$, $n = 0.5$. Measurements are fitted with $K_{\nu T} = K_\nu\, a\, e^{-bT}$, with $A = 1.6927$ and $B = -0.0257\,\mathrm{K^{-1}}$.

Acknowledgments The work has benefited from discussions with François Boulogne, Georg Dietze and Fabien Mahaut and help in the laboratory from Floriane Touitou, Alban Aubertin and Lionel Auffray. The manuscript was improved, thanks to the comments of two anonymous reviewers. A. Massmeyer and T. Rolf are supported by the Initial Training Network (ITN) Crystal2Plate, an FP7-funded Marie Curie Action under grant agreement number PITN-GA-2008-215353. E. Di Giuseppe was funded by the French Agence Nationale de la Recherche (PTECTO NT09-604042).

Appendix A: Temperature Dependence of the Consistency

The temperature dependence for $K_{\nu T}$ has been evaluated performing a temperature sweep test at constant shear rate. To verify the uniformness of the model, we used two different mixtures of Carbopol (for rheological properties see figure caption fig. 4.17) and applied two different shear rates $\dot\gamma = 1\,\mathrm{s^{-1}}$ and $\dot\gamma = 10\,\mathrm{s^{-1}}$. The results are plotted in fig. 4.17. The figure shows that the model $K_{\nu T} = K_\nu\, A\, e^{-BT}$ with the coefficients $A = 1.6927$ and $B = -0.0257\,\mathrm{K^{-1}}$ fits the data reasonably well, for both fluids and at both shear rates.

5. Characterization of the Steady State

The temperature fields in fig. 5.1 for the laboratory experiment ($Y_0 = 316$, $K_\nu = 1.114\,\mathrm{Pa\,s}^n$, $n = 0.62$) and the numerical simulation ($Y_0 = 224.11$, $K_\nu = 1.403\,\mathrm{Pa\,s}^n$, $n = 0.7$) look quite different, due to the different fluid parameters and the different power applied. Therefore the question arises, whether there is a unifying formulation that allows to predict certain characteristics of the thermal instability in the steady state. We may therefore assume, that the plume stem has a characteristic radius $a(z)$, corresponding to the size of the shear zone (fig. 5.2 A) and rises with an average vertical velocity $w(z)$.

5.1. Dimensional Analysis for the Steady State

In *Davaille et al. [2013]* we have shown that the velocity field inside the instability resembles a plug-flow. Therefore the vertical velocity w should be proportional to the product of the radius of the instability a (here the conduit) and the shear rate that is created around it (cf. fig. 5.2)

$$w \propto \dot{\gamma} a \Leftrightarrow w = C_3 \dot{\gamma} a. \tag{5.1}$$

The governing equations for a stationary plume are as follows: the Stokes equation may be expressed as the total stress in the system due to the buoyancy stress of the fluid inside the stem and is therefore written as

$$\sigma_0 + K_\nu \dot{\gamma}^n = C_1 \alpha \overline{\Delta T}(z)\, a\, g \tag{5.2}$$

where $\overline{\Delta T}$ is the temperature difference between source and ambient fluid. In the experiments, the heat source is operated at constant power. Therefore conservation of power requires

$$P = \rho C_p \int w \overline{\Delta T}(z) 2\pi r dr \Leftrightarrow \overline{\Delta T}(z) = \frac{P}{\pi C_2 \rho C_p w a^2} \tag{5.3}$$

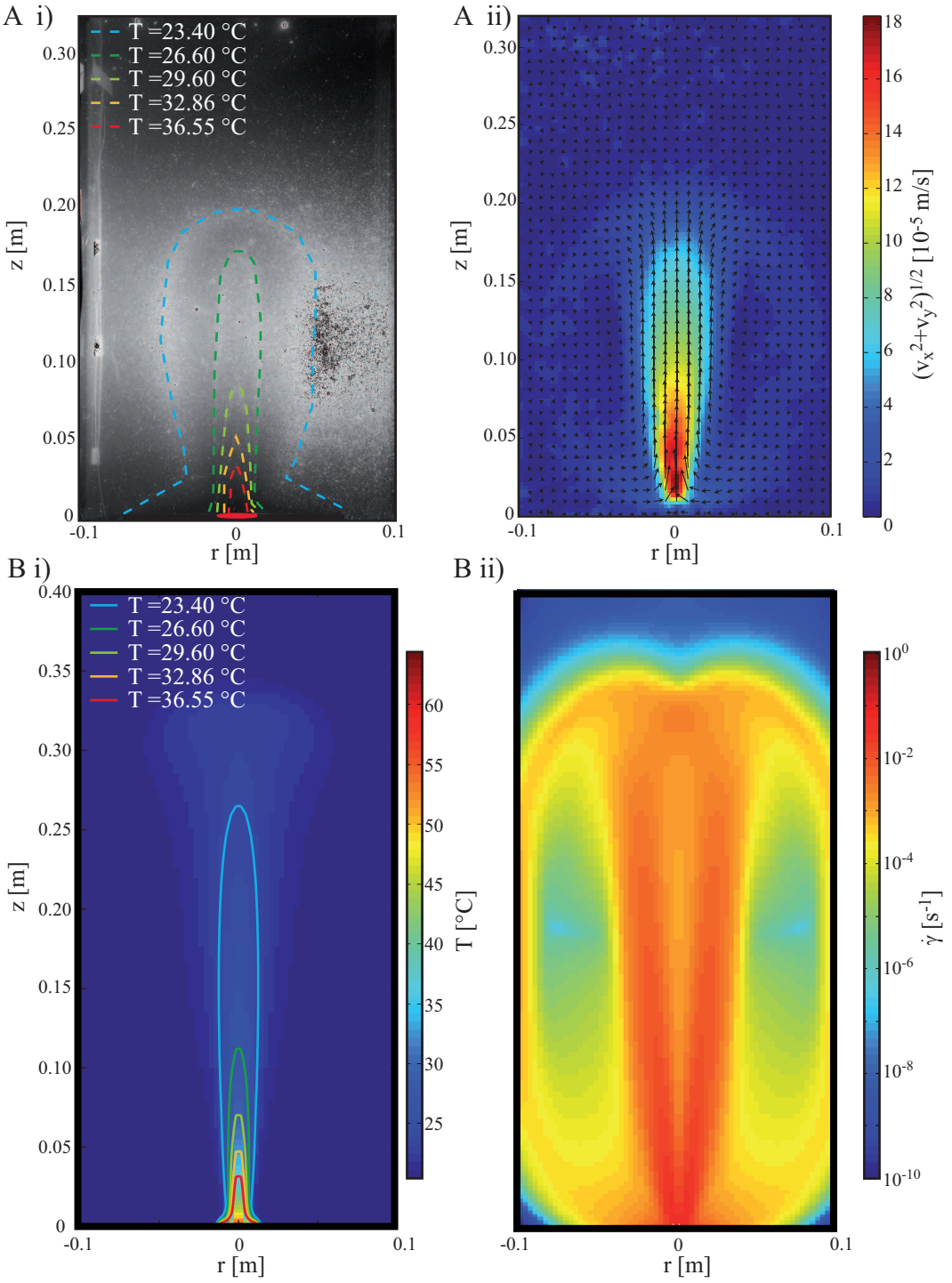

Figure 5.1.: Results from laboratory (A) and numerical (B) experiments for A for $Y_0 = 316$ and B $Y_0 = 224.11$. A and B i): temperature field, A ii) velocity field and B ii) strain rate. A: red ellipse at the bottom indicates copper-plate dimension.

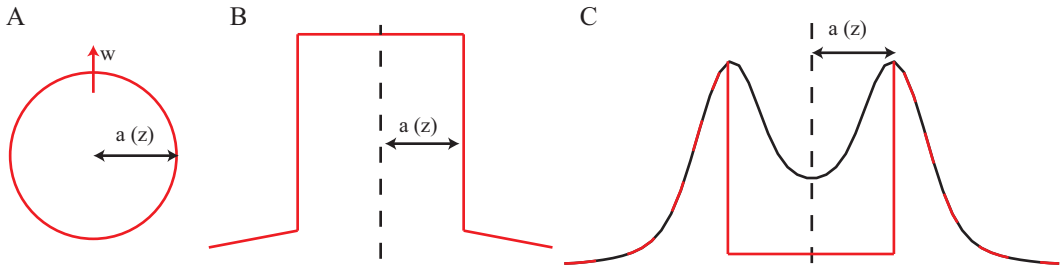

Figure 5.2.: A: schematic idea of fluid pocket rising as a solid object. The pocket moves at constant speed, therefore produces a plug-flow, cf. B: velocity profile created by the rising pocket. C: shear rate profile with typical profile (black line) and profile that would result from solid object.

Conservation of heat implies

$$(\mathbf{v}\cdot\nabla)\,T = \kappa\nabla^2 T \tag{5.4}$$

$$\Leftrightarrow \frac{w}{z}\Delta T = C_4\frac{\kappa\Delta T}{a^2} \tag{5.5}$$

$$\Leftrightarrow a^2 w = C_4\kappa z$$

$$\Leftrightarrow \boxed{a = \left(C_4\frac{\kappa z}{w}\right)^{1/2}} \tag{5.6}$$

$$\Leftrightarrow \boxed{w = C_4\frac{\kappa z}{a^2}} \tag{5.7}$$

Substitution of 5.7 into 5.3 yields the temperature at the axis of the instability as a function of the supplied power, the height and the fluids density and thermal conductivity

$$\boxed{\overline{\Delta T}(z) = \frac{1}{\pi C_2 C_4}\frac{P}{\rho C_p \kappa z}}. \tag{5.8}$$

Substituting equations 5.3 and 5.1 into 5.2 yields

$$\sigma_0 + K_\nu\left(\frac{w}{C_3 a}\right)^n = \alpha g\frac{PC_1}{\pi C_2 C_p}\frac{1}{aw}. \tag{5.9}$$

For simplicity we assume that the yield stress is small compared to the viscous stress. In fact the Bingham number is about $Bi \approx 0.5$ where the shear rate is maximum, as the plume rises. Expressing the velocity w with the radius a (eq. 5.6) leads to a formulation of the characteristic radius

$$\boxed{a = C(n)\left(\frac{K_\nu C_p(\kappa z)^{n+1}}{\alpha g P}\right)^{\frac{1}{3n+1}}}, \tag{5.10}$$

where $C(n)$ is a combination of different constants and a dependence on n.

5.2. Validation of the Proposed Scalings

5.2.1. Temperature along the Plume Axis

The temperature along the plume axis should be described by 5.8. To illustrate the applicability of this scaling, fig. 5.3 shows the temperature difference between plume axis and ambient fluid for simulations and experiment and the prediction by equation 5.8. With $C_2C_4 = 1.25 \pm 0.25$, scaling and simulation correspond well within 1 K for all three simulations. The difference is bigger for the experiment, however the only uncertainty regarded here, is the uncertainty of the isotherms. Additionally the thermal power is only certain within 10 %, which could result in a shift of the curve towards the left, if the real thermal power was lower. Therefore the laboratory results agree with the prediction within the errorbar.

5.2.2. The Characteristic Radius of the Stem

In fig. 5.4 Ai) the radius where the shear rate is maximum is compared to the radius obtained from equation 5.10. A good fit between the different radii is obtained for the coefficient

$$C(n) = C_a^{\frac{C_b n}{C_c}} \tag{5.11}$$

where $C_a = 0.1645$, $C_b = 3.122$ and $C_c = 1.632$, with a root mean square error of 0.002148 for $C(n)$. The radius can then be translated into a shear rate by substituting equation 5.7 into 5.1. This can be done for

- evaluating the position (and therefore the radius) of the maximum shear rate (fig. 5.4Aii) dashed lines)
- the radius calculated from equation 5.10 (fig. 5.4Aii) straight lines).

5.2.3. Shear Rate and Velocity

A comparison with the maximum shear rate in the simulations (fig. 5.4Aii) dots) shows that the curves collapse well, whereby the constants are $\sqrt{C_4}C_3 = 0.7 \pm 0.2$.
Equation 5.7 then permits to calculate the velocity. Fig. 5.5 shows that the velocity averaged over the plume stem (inside a) is well approximated by equation 5.7 with $C_4 = 0.1875 \pm 0.0285$.

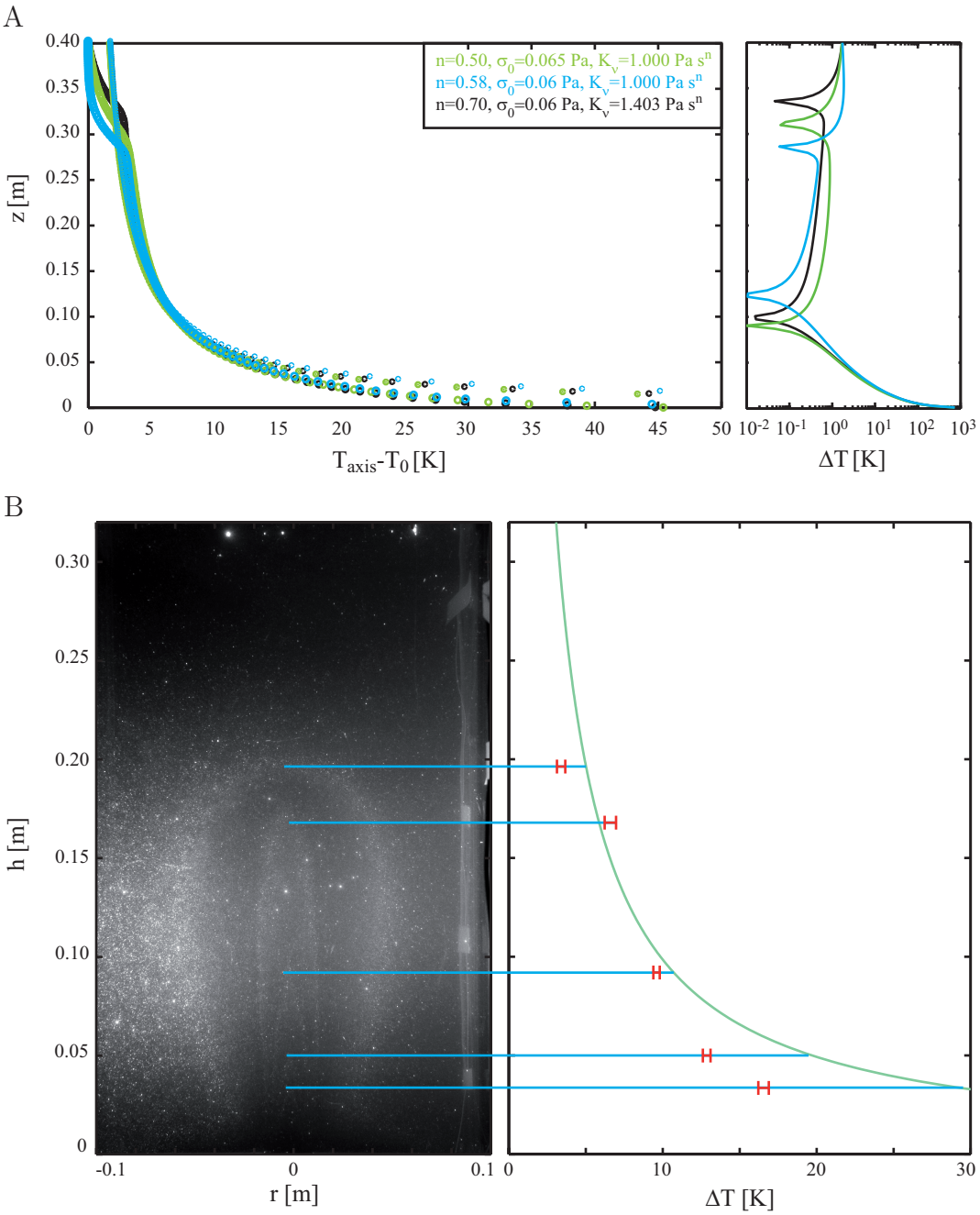

Figure 5.3.: A: Temperature profiles for simulations and calculated from equation 5.8 and the difference between those two temperatures ΔT. The temperature is well predicted within 1 K inside the plume stem. B: Temperature profile for experiment with CBP14 at $P = 2.02$ W and calculated from equation 5.8 with $C_2C_4 = 1.25$. Red bars indicate temperature difference between ambient fluid and isotherm, where the errorbar indicates the error from the isotherm-calibration.

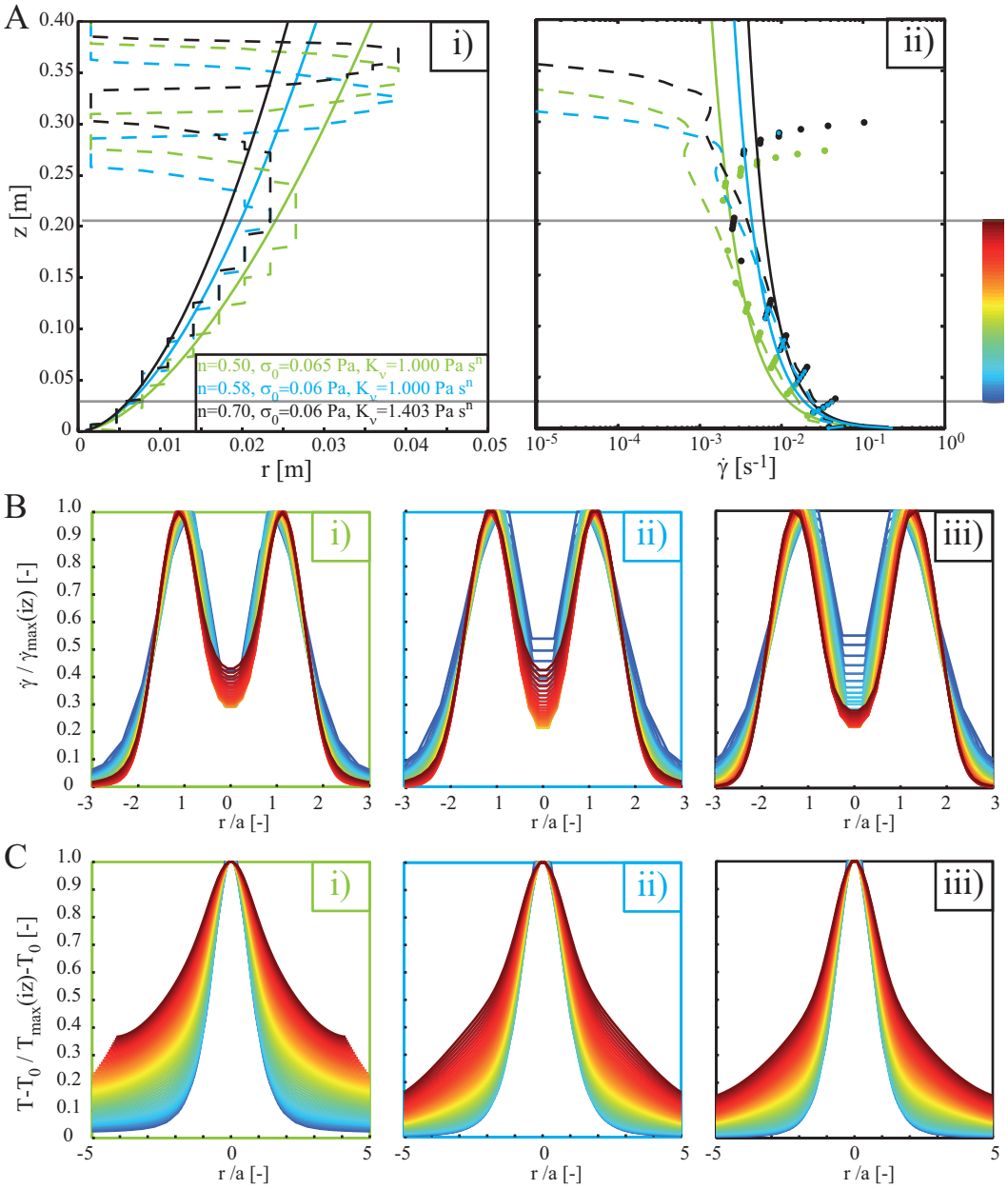

Figure 5.4.: A: Radius i) and shear rate ii) obtained from scaling (straight line) and simulation (dashed line). Dots indicate the shear-rate obtained with equation 5.10 for the radius where $\dot{\gamma}$ is maximum. Colorbar indicates height-colorcode used in B and C. B: Normalized shear rate profiles and C: Normalized temperature profiles as function of the normalized radius.

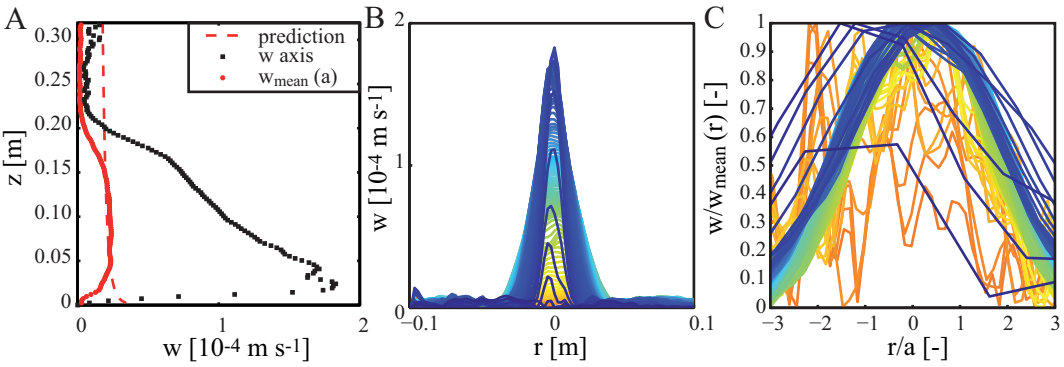

Figure 5.5.: A: velocity-depth profile for the maximum velocity along axis (black square), the mean velocity inside the characteristic radius a (red dots) and the predicted radius after equation 5.6 (red dashed line). B: velocity profile for different depths between for $z = 0 - 0.24\,\mathrm{m}$. C: velocity normalized by mean velocity inside characteristic radius a as a function of the normalized radius.

5.2.4. Justification of Simplifying Assumption: Yield-Stress Inside the Plume Stem can be Neglected

Fig. 5.6 is an attempt to combine the results obtained in chapter 4 with the scaling obtained for the temperature along the plume axis in the steady state. If the radius is taken as a (from eq. 5.10), the yield number Ψ becomes subcritical before the height h_y is reached. This is interesting, as the material inside the plume still continues to rise. This is also the case if the radius to calculate the yield number is taken as the radius of a sphere with equivalent volume as the hot pocket that forms around the heater, r_{eq}. This highlights, that inside the plume, the yield stress is negligible and justifies that this was assumed for the calculation of a.

5.3. Conclusions - Scaling for the Steady State

Here we propose a scaling for the characteristic radius of the plume stem in the steady state. The characteristic radius corresponds to the distance of the maximum shear rate from the plume axis and is a function of the height, applied power and fluid properties, where the yield stress is neglected. The mean velocity inside the stem scales with the radius. The temperature along the plume axis is independent of the rheological properties of the fluid and scales with the applied thermal power, the thermal properties of the fluid and height. We have validated the scaling with several numerical simulations and a laboratory experiment to cross-check the results.

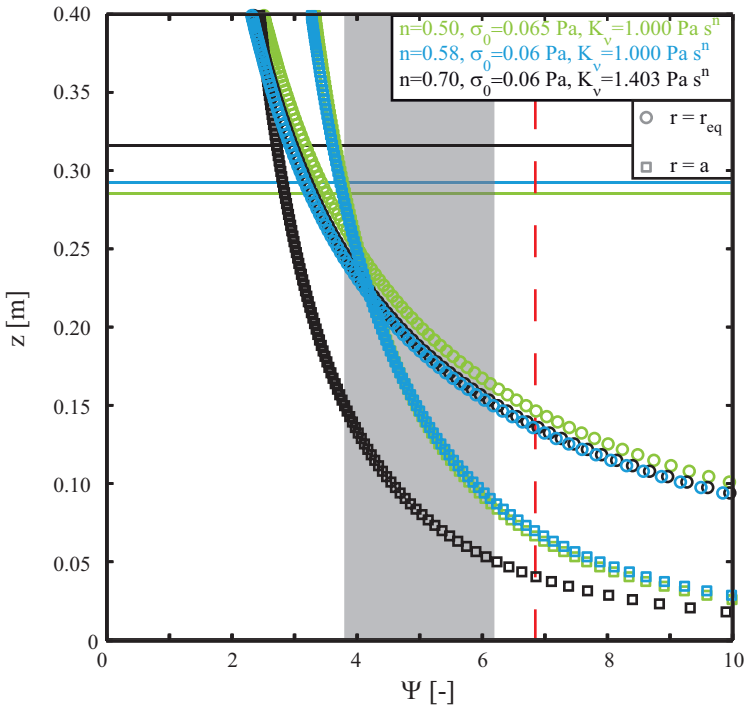

Figure 5.6.: Yield number Ψ (eq. 4.2) calculated with the radius of the equivalent bubble r_{eq} (circles) and a (eq. 5.10, squares) for different simulations. The horizontal lines indicate the height h_y where the plume stops, as defined in fig. 4.2. The grey region indicates $\Psi = 5 \pm 1.2$, which is the critical value found in *Massmeyer et al. [2013]* (chapter 4), red dashed line $\Psi = 6.85$ (*Dubash and Frigaard [2004, 2007]*, *Beris et al. [1985]*, *Tabuteau et al. [2007]*).

6. Thermal Instabilities in a Complex Lithosphere and Mantle.

An overview of the complexity of Earth's rheology is given in section 1.2, describing that the lithosphere may act as a solid even on geological timescales, but may also show a visco-elastic behaviour. This chapter shows how the results obtained in chapters 3-4 may be applied to the Earth and may help to better constrain Earth rheology.

6.1. Magmatic Intrusions in the Lithosphere

Dykes are fast intrusions of magma into the lithosphere. They propagate at few metres per second and are seismologically detectable (*Einarsson and Brandsdòttir [1979]*) as they fracture through the solid lithosphere on a very short timescale. Dykes are very thin, compared to their breadth (cf. fig. 6.1) and their thickness varies between some millimeters to a few meters (eg. *Kavanagh et al. [2012b], Gudmundsson [1983]*). Hence the process is limited by the strength of the ambient matrix, and dyking is only possible if the pressure in the magma source (e.g. a magma chamber) is sufficiently high to overcome the yield stress of the lithosphere. The propagation of the dyke then releases the pressure in the magma chamber and the dyke will slow down (*Buck et al. [2006]*). *Jònsson [2012]* inverts InSAR-data recording a dyking event on the western Arabian Peninsula from 2009 and finds a tensile rock strength between $1 - 3\,\mathrm{MPa}$.
Due to the short timescale of the dyking-event, the lithosphere's response is supposed to be mainly elastic. An analog material behaving elastically on short timescales under high stresses is gelatine (*Di Giuseppe et al. [2009]*). Hence, several studies used gelatine to model the emplacement of dykes in an elastic lithosphere (e.g. *Menand and Tait [2001], Menand et al. [2003], Walter and Troll [2003], Rivalta et al. [2005], Kavanagh et al. [2006], Maccaferri et al. [2010], Kavanagh et al. [2012a]*). The dykes form fissures taking the shape of two-dimensional sheets. In experiments with one layer, the dykes fracture vertically towards the surface. If several layers are used, models show that the dyke may spread horizontally at the contact with a stronger layer, therefore forming sills (e.g. *Rivalta et al. [2005], Kavanagh et al. [2006]* for experiments and *Maccaferri et al. [2010]* for simulations and experiments).
Another form of magmatic intrusions in the lithosphere are diapirs. Diapirs are three-dimensional objects, similar to plumes, with a diameter of a few 10 km. Their emplacement

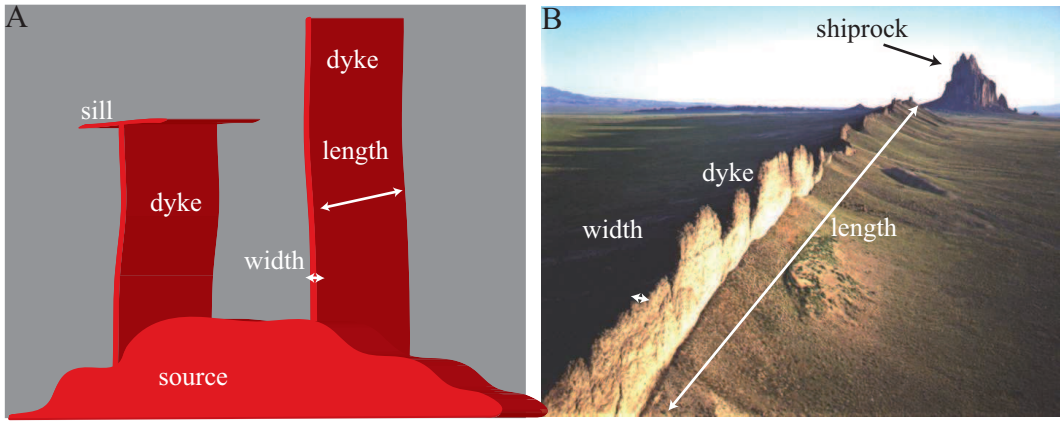

Figure 6.1.: A: schematic illustration of a dyke propagating from a source, e.g. a magma chamber. Dykes may evolve, when the overpressure in the magma source is sufficiently high. B: Photo of the shiprock (eroded volcano throat) with a joined dyke. Note that the dyke width is much smaller than its length. Image source: www.geology.com/images/st-pauls-island/magmatic-dike-dyke-shiprock.jpg.

is much slower than the emplacement of dykes: For example the uplift measured above the Altiplano-Puna magma body is only a few mm/year *Fialko and Pearse [2012]*, fig. 6.2. Hence, due to the different time-scale of emplacement, numerical studies on diapir intrusions into the crust use stress and temperature dependent rheology without (e.g. *Bittner and Schmeling [1995]*) or with an elastic crust (e.g. *Gerya and Burg [2007]*, *Fialko and Pearse [2012]*). *Gerya and Burg [2007]* place a partially molten peridotite body at $\approx 200\,\mathrm{km}$ depth (fig. 6.3) and study the shape of the ascending material and the resulting surface deformation, as a function of the properties of the overlying crust and mantle. *Fialko and Pearse [2012]* show that the central uplift and surrounding subsidence (forming a sombrero-shape, cf. fig. 6.2) observed above an active magma body in the central Andes (Altiplano-Puna ultralow-velocity zone) may be explained by a mid-crustal diapir.

Jousselin and Nicolas [2000] study an off-axis diapir emplaced in a ridge context in Oman (cf. fig. 6.4). While the on-axis diapir has a very smooth deformation pattern, the off-axis diapir presents strong deformation localized to its edges. The different morphologies can be explained by the viscosity being mostly temperature dependent at the ridge, hence the observed deformation resembles more a Newtonian fluid. However as the lithosphere spreads away from the ridge it cools, and will therefore present viscoelastic properties, i.e. the lithosphere should present a yield stress. Therefore it is not surprising that the diapir strongly resembles the instabilities studied in sections 3 and 4.

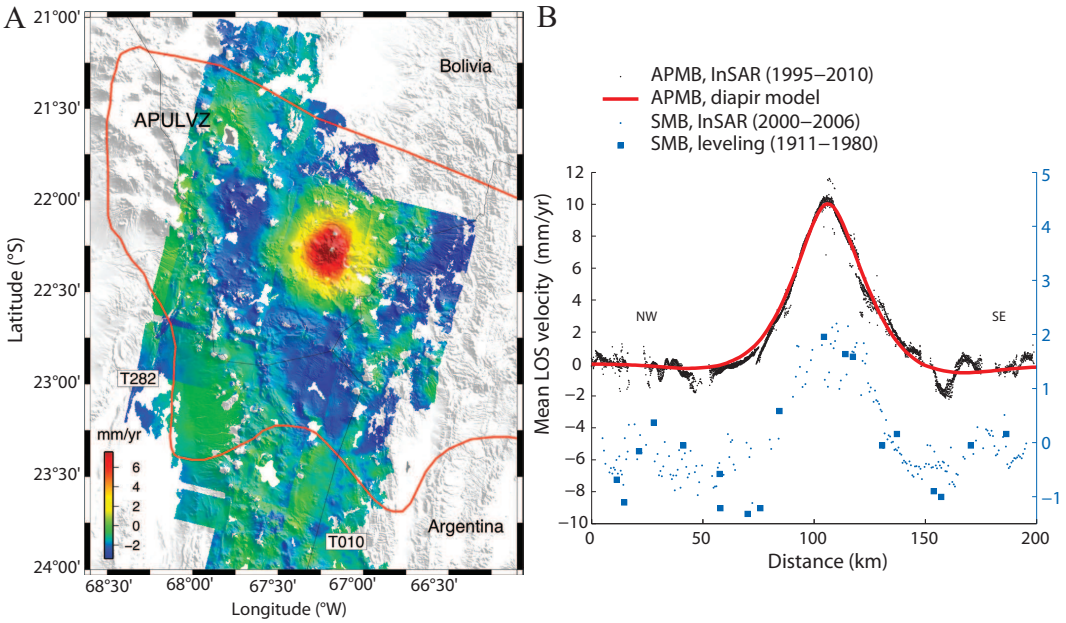

Figure 6.2.: Adapted from *Fialko and Pearse [2012]* APULVZ: Altiplano-Puna Ultralow-Velocity Zone. A: Color indicates uplift (red) and subsidence (blue) line-of-sight (LOS) velocities, evaluated from ERS-1/2 and EnviSAT data. Red line denotes extent of the seismically imaged ultra-low-velocity-zone (ULVZ) in the middle crust. B: Observed (black dots) and predicted (solid red line) LOS velocities along northwest-to-southeast profile, crossing the center of the uplift (A). Blue symbols (right axis) show surface velocities due to the Socorro Magma Body (New Mexico).

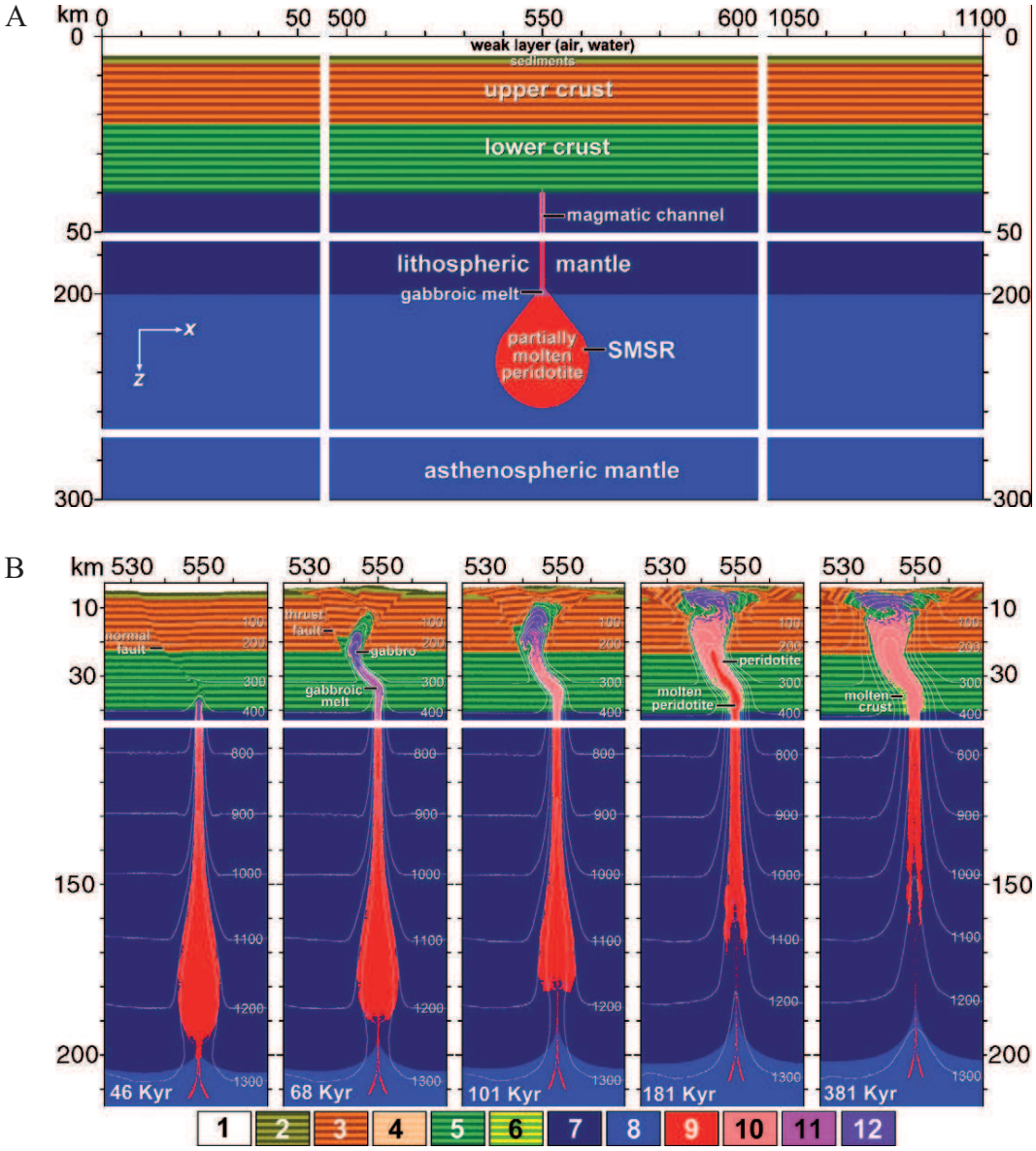

Figure 6.3.: from *Gerya and Burg [2007]*. A: initial model setup, with partially molten peridotite at 200 km depth. B: the partial melt ascends through a heated channel and forms intrusions in the crust. Colorcode: weak layer (1), sediments (2), upper solid (3) and molten (4) crust, lower solid (5) and molten (6) crust, lithospheric (7) and asthenospheric (8) mantle, molten (9) and crystallized (10) peridotite, molten (11) and crystallized (12) gabbro. White lines are isotherms in °C.

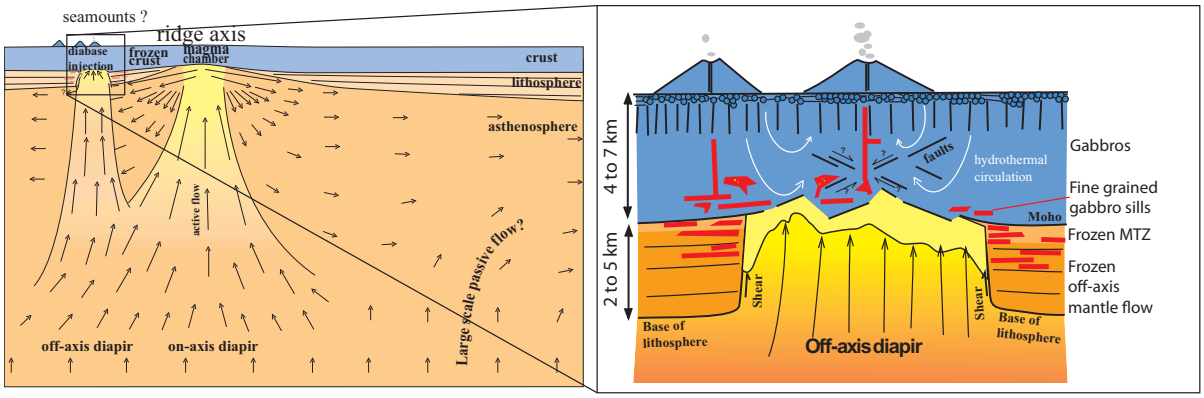

Figure 6.4.: Sketch of ridge-cross section, courtesy of *Jousselin and Nicolas [2000]*. Detail shows deformation as observed for the off-axis ridge, where strong deformation is localized at the edges of the diapir.

6.2. Conditions for Emplacement of Diapirs and Plumes in Lithosphere or Mantle with Complex Rheology

The results from section 4 show, that two conditions need to be fulfilled to allow for an instability to rise in a yield stress fluid:

- $\Psi = \frac{2gr\Delta\rho}{3\sigma_0} > 6.85$
- $Bi = \frac{\sigma_0}{K_\nu \dot{\gamma}^{1/n}} = \frac{\sigma_0}{K_\nu \dot{\gamma}^n E} < 1.$

The first equation can be reformulated to calculate the maximum yield stress that allows for a given density anomaly to develop. This is the case for yield stresses smaller or equal to

$$\sigma_0 = \frac{2}{3}\frac{gr\Delta\rho}{6.85}. \tag{6.1}$$

In fig. 6.5 the maximum yield stress allowing for an instability to rise in a yield stress matrix is shown, depending on its density difference to the ambient matrix as well as its radius. The implications of this will be discussed in the following for upwellings in the lithosphere and in the mantle.

6.2.1. Emplacement Conditions for Instabilities in the Lithosphere

The diapir (*Jousselin and Nicolas [2000]*) has a diameter of $d \approx 10\,\mathrm{km}$. The temperature at a distance of 35 km from the ridge should be around 900 °C at 5 km depth. Assuming a density of $\rho = 3000\,\mathrm{kg\,m^{-3}}$, a thermal expansivity of $\alpha \approx 2\,10^{-5}\,\mathrm{K^{-1}}$ and

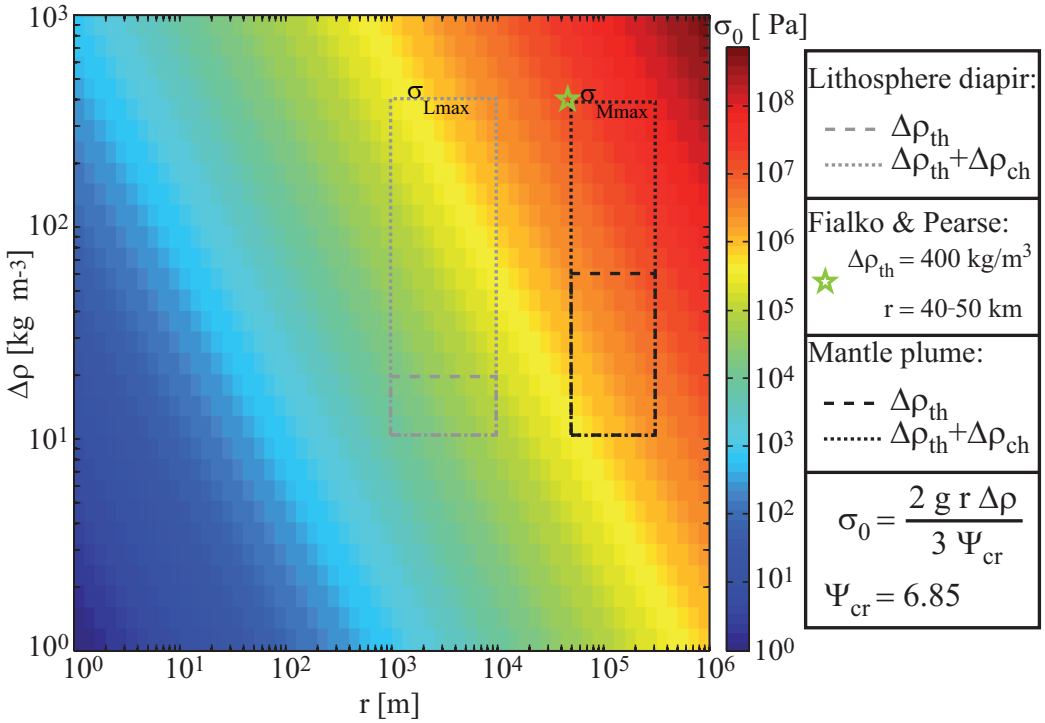

Figure 6.5.: Maximum yield stress σ_0 that allows for an instability of given radius r with density difference $\Delta\rho$ to rise. Rectangles highlight regions for possible diapirism due to a purely thermal density contrast (dashed) or thermal and chemical density contrast, as well as mantle plumes (dash-dotted). Maximum possible yield stresses for instabilities in the lithosphere and mantle are named σ_{Lmax} and σ_{Mmax} respectively.

that the temperature of emplacement is $T \approx 1200\,°\mathrm{C}$, results in a density difference of $\Delta\rho \approx 10 - 20\,\mathrm{kg\,m^{-3}}$. Therefore the maximum yield stress allowing for such an instability to rise would be around $\sigma_{Lmax} = 100\,\mathrm{kPa}$. Such a low yield stress indicates that the surrounding matrix would need to be at least partially molten (*Kohlstedt and Zimmerman [1996]*, *Scott and Kohlstedt [2006]*). This is based on the assumption that the diapir is a result of an asthenospheric, purely thermal, instability (*Jousselin and Nicolas [2000]*). In the case of plume-ridge interaction (*Mittelstaedt and Ito [2005]*) 1) the temperature difference may be higher and 2) chemical heterogeneities may aid by lowering the density. Another buoyancy source may be decompression melting (e.g. *Scott and Stevenson [1989]*) or melt depletion (e.g. *Schutt and Lesher [2006]*). All these mechanisms could increase the density difference uo to $\Delta\rho \approx 400\,\mathrm{kg/m^3}$ Therefore a diapir could rise through a matrix with a yield stress of up to $\sigma_{Lmax} = 3\,\mathrm{MPa}$ (cf. fig. 6.5). This value corresponds well to the ones found by *Jònsson [2012]* for the dyking event on the western Arabian

Peninsula of $1-3\,\mathrm{MPa}$. Furthermore this explains why *Gerya and Burg [2007]* had to use a plastic strength of 1 MPa stating that "*higher plastic strength precludes the ascent of magma*". *Fialko and Pearse [2012]* find that their model best fits the observation if a density difference of $\Delta\rho = 400\,\mathrm{kg\,m^{-3}}$ is assumed, while the radius of their instability is about $r = 40-50\,\mathrm{km}$. Such a large diapir with its huge buoyancy could be emplaced in a matrix with a yield stress of up to $\sigma_{Lmax} = 19\,\mathrm{MPa}$.

6.2.2. Emplacement Conditions for Mantle Plumes

Most models assume that the Earth's mantle is Newtonian (e.g. *Trompert and Hansen [1998]*, *Tackley [2000a]*, *Stein et al. [2004]*) and therefore without a yield stress. However, a rising plume may be stopped by a strong upper mantle as in the jelly sandwich model (see e.g. *Burov and Watts [2006]*), if the stress induced by its buoyancy becomes too small compared to the yield stress (cf. section 4). The density contrast might thereby be increased by melting or incorporated chemical heterogeneities in the plume. A purely thermal plume would therefore be stopped for mantle yield stresses between 0.5 MPa for small plume radius and small density contrast and 17 MPa if the plume is larger and more buoyant. If its buoyancy was further increased it might even enter a matrix of up to $\sigma_{Mmax} \approx 114\,\mathrm{MPa}$. These values question the possibility of the jelly sandwich model with a strong upper mantle. Depending on the strength this strong layer could make it impossible for thermal instabilities from the mantle to enter the upper mantle or crust.

6.3. Possible Implications for Viscosity and Shear Rate

The second condition $Bi \leq 1$ allows to calculate the minimum shear rate $\dot{\gamma}$ that is needed for given parameter constellations of the yield stress σ_0, consistency K_ν and shear thinning parameter n and the corresponding maximum viscosity that allows for a plume to develop at those conditions

$$\dot{\gamma}_{min} = \left(\frac{\sigma_0}{K_\nu}\right)^{n_E} \Leftrightarrow \eta_{max} = 2\,\sigma_0 \left(\frac{\sigma_0}{K_\nu}\right)^{-n_E}. \tag{6.2}$$

On Earth, rheology depends on several parameters (cf. section 1.2) and writes (after *Hirth and Kohlstedt [2003]*) as

$$\dot{\gamma} = A\,\sigma^{n_E}\,d^{-p} f_{H_2O}\,exp\left(\beta\,\Phi\right)\,exp\left(-\frac{E^* + P\,V^*}{RT}\right), \tag{6.3}$$

where A is a constant, d is the grain-size with the grain-size exponent p, f_{H_2O} is water fugacity , Φ is the melt fraction, β is a constant, T is the temperature, P pressure, E^* is

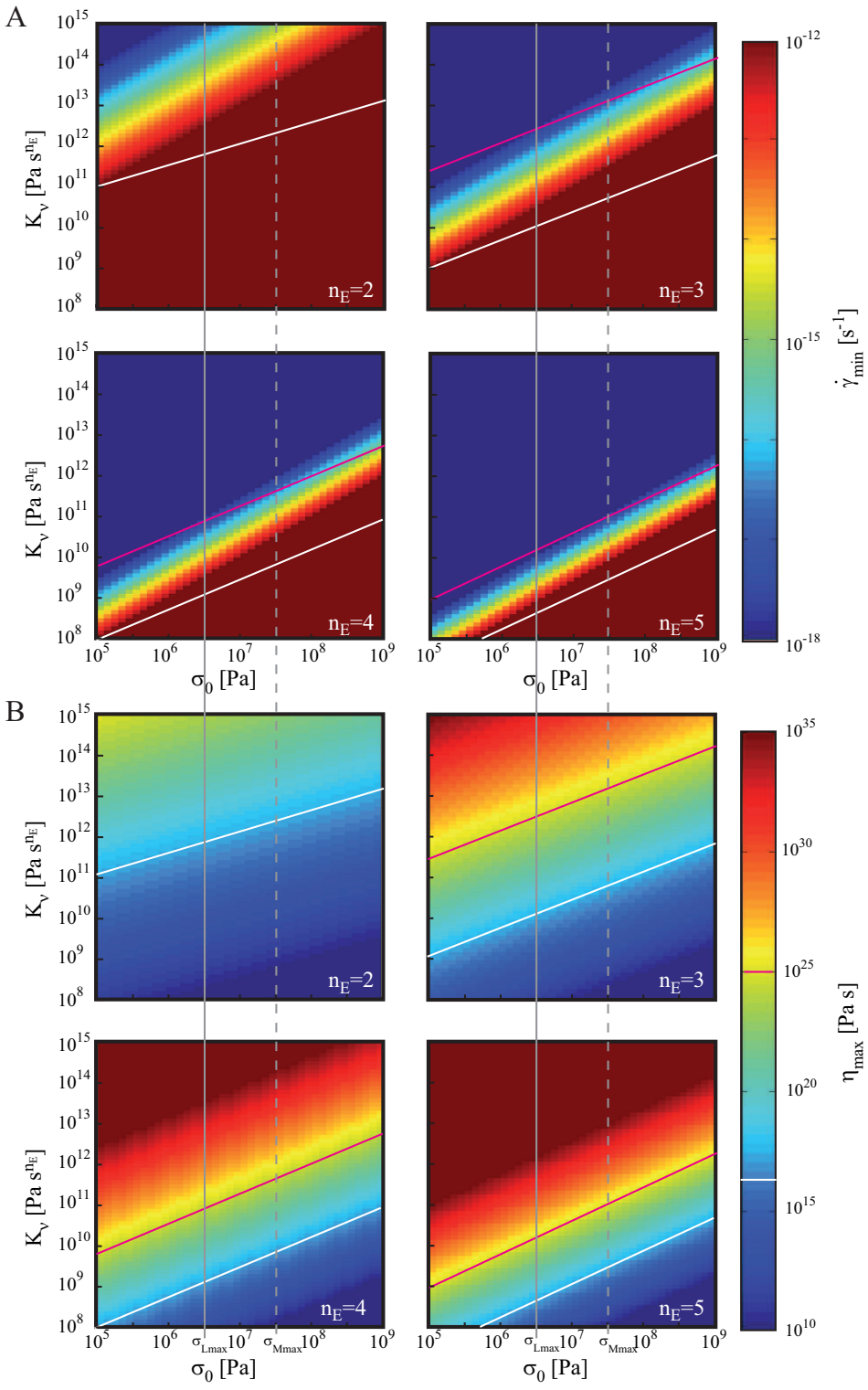

Figure 6.6.: A: Shear rate $\dot{\gamma}_{min}$ and B: corresponding viscosity η_{max} at $Bi = 1$ after equation 6.2 in dependence of K_ν and σ_0 for four different n_E. Vertical grey lines indicate maximum yield stress that allows for instability to develop after fig. 6.5 in the lithosphere σ_{Lmax} and in the mantle σ_{Mmax}. White and pink straight lines mark minimum and maximum realistic viscosities.

the activation energy , V^* is the activation volume and R is the universal gas constant. A similar reformulation for the Herschel-Bulkley model yields

$$\dot{\gamma} = (\sigma - \sigma_0)^{n_E} \frac{1}{K_\nu^{n_E}} \tag{6.4}$$

and shows that K_ν translates for Earth as follows

$$K_\nu = \left(A\, d^{-p} f_{H_2O}\, exp\,(\beta\, \Phi)\; exp\left(-\frac{E^* + P\, V^*}{RT} \right) \right)^{(-1/n_E)} \tag{6.5}$$

The viscosity of the Earth's mantle should roughly be within the range of 10^{17} to 10^{25} Pas (cf. section 1.2), which corresponds to the range between the white and pink lines on fig. 6.6. The shear thinning exponent is varied between $n_E = 2 - 5$, since for the lithosphere n_E is in between 2 and 4.5, e.g. *Ranalli [1995]*. Taking into account the yield stress limits σ_{Lmax} and σ_{Mmax} for lithosphere and mantle shows that, depending on the intensity of stress dependence, the "choice" of K_ν is rather limited. In order to obtain realistic shear rates and viscosities, the interval for K_ν depends on the shear thinning index n_E. For example $n_E = 5$ would limit K_ν between $3.2\,10^8$ and $10^{11}\,\mathrm{Pa\,s^5}$.

6.4. Conclusions - Geophysical Application

In section 6.2 we have shown that the question whether a diapir may be emplaced strongly depends on the rheology of the surrounding matrix. Applying the non dimensional parameters that we obtained in chapter 4, places strong constraints on the strength of the lithosphere and the upper mantle. Depending on the size and the buoyancy of an anomaly, the strength that would permit for such an object to rise, varies between 100 kPa and 114 MPa, corresponding to the results from *Jònsson [2012]*. This means, that the lithosphere has to be rather weak in order to allow for intrusions. Those values furthermore question the possibility of the jelly sandwich model, as a strong upper mantle could make it impossible for a mantle plume to penetrate the upper mantle or lithosphere.
In section 6.3, we place ourselves on the marginal case, where the Bingham number is equal to one, i.e. where the viscous forces are as strong as the yield stress. This places constraints on the maximum value that the consistency K_ν may have in order to allow for an instability to develop.

7. Conclusion and Outlook

In this study, we have combined laboratory experiments and numerical simulations to investigate the dynamics of thermal plumes in a yield stress fluid. We show that a thermal instability in Carbopol is well described with a regularized Herschel-Bulkley model. In both, numerical simulations and laboratory experiments, the instability has a finger-like shape as described in *Davaille et al. [2013]* and deformation is localized close to the thermal instability.

The numerical simulations permitted to identify the key parameters that determine whether a thermal instability may develop and rise. The first critical parameter is the yield number Ψ, comparing the stresses due to the buoyancy of the hot pocket forming around the heater to the yield stress. We find a critical value of $\Psi_c = 5 \pm 1.2$. This value is close to the critical yield parameter found for bubbles that rise in (*Dubash and Frigaard [2004, 2007]*) and spheres that sink into (*Beris et al. [1985]*, *Tabuteau et al. [2007]*) a yield stress fluid, which is $\Psi'_c = 6.85$. The second parameter is the Bingham number Bi, comparing the yield stress to the viscous stresses. We show that the plume develops out off a cell and only if the convection of this cell is vigorous enough and produces sufficiently high shear rates, it may evolve into a plume. The critical Bingham number therefore is $Bi = 1$, i.e. the viscous stresses are equal to the yield stress. These parameters do not only determine whether a plume starts, but also whether it may continue to rise through the fluid.

A comparison of the different regimes that maybe obtained, to those we have found with a different setup in *Davaille et al. [2013]* shows, that the different heat-source geometries lead to different critical yield parameters. We show that if we correct the thermal power that is available as a buoyancy source for the plume for the experiments of *Davaille et al. [2013]*, both geometries have the same critical parameter of $Y_{c1} = 100 \pm 10$ for the transition from no motion to a cell and $Y_{c2} = 150 \pm 10$ for the transition from cell to plume.

We have shown, that for the dynamics of the plume stem in steady state, the yield stress can be neglected and only the viscous stresses with the shear thinning part need to be taken into account. This allows to derive scaling laws for velocity, temperature at the plume axis and size of the shear zone in the plume stem in the steady state.

When we apply the non-dimensional parameters that we find in the numerical simulations and the laboratory experiments to Earth, we find fluid dynamic constraints for the evolution of diapirs. The Bingham number allows to calculate the maximum viscosity that would allow for a plume to develop. More importantly, our results show that, changing with the size and buoyancy of the source, a diapir can only develop, if the strength of the surrounding matrix is limited. This limiting strength is smaller than 100 kPa for small diapirs with diameter of a few ten kilometres and with low buoyancy and smaller than 114 MPa for large and buoyant plumes.

The work presented here is limited to a single instability. It would be interesting to study the spacing between several instabilities. Due to the yield stress it is difficult to study this in a Rayleigh-Bénard setup. A simple way around this could be to study instabilities that form from a heated line. We have performed preliminary tests that were exhibiting an intermittent behaviour, switching between two and one instabilities in time, but those preliminary results would need to be looked at in detail. Besides this, the work opens more interesting perspectives. One question is, whether a yield stress in the Earth's mantle would influence the shape of an instability. Hence it would be interesting to couple a yield stress rheology with a strong temperature dependence, e.g. numerically. Another question could be to investigate what happens to an instability that forms in a Newtonian fluid and tries to penetrate into a non-Newtonian fluid. This could be done with a layered system, e.g. of Natrosol and Carbopol. The difficulty here would be to find two fluids that have similar densities, so that the instability in the lower fluid would be less dense than the upper fluid layer, while at room temperature the upper fluid is less dense. A way around this, could be to study Rayleigh-Taylor instabilities employing for example a technique like *Renoult et al. [2011]*. Another possibility would be to inject hot newtonian fluid into a tank that is filled with a non-Newtonian fluid like Carbopol.

A. Appendix

A.1. Thermal instabilities in a yield stress fluid: Existence and Morphology[1].

Abstract We present new laboratory experiments on the development of thermal plumes out of a localized heat source in Carbopol, a yield-stress and shear-thinning fluid. Depending on the Yield number Y_0, which compares the thermally-induced stress to the yield stress, three different regimes obtain. For low Y_0 (<120), no convection develops; while for intermediate values, a small-scale convection cell appears and remains confined around the heater. For high Y_0 (>260), thermal plumes develop. Their morphology differs from the mushroom-shape typically encountered in Newtonian fluids. Combined temperature and velocity field measurements show that a plug flow develops within the plume thermal anomaly, therefore producing a rising finger-shape. Moreover, light scattering highlights the development of a damaged zone prior to the plume onset, and the peculiar structure of the gel around the plume as it rises. This brings new insights into the solid-liquid transition of soft gels.

A.1.1. Introduction

Although non-Newtonian fluids are common in natural and industrial systems undergoing thermal convection (*ie* food or glass processing, lava lakes, planetary mantles..), the occurrence and characteristics of thermal instabilities in such fluids are still poorly documented and understood. Part of the difficulty is that the viscosity of these fluids approaches infinity when the shear rate vanishes. Hence, from a theoretical point of view, convective instabilities cannot grow from a static conductive state submitted to infinitesimal perturbations (Zhang et al. [2006]; Solomatov and Barr [2007]; Balmforth and Rust [2009]; Vikhansky [2009]), contrary to the case of Rayleigh-Benard convection in Newtonian fluids (Chandrasekhar [1961]). In laponite, where the non-Newtonian effects increase as the fluid ages, convection is killed after a while (Bellon et al. [2007]). Recent qualitative experiments in constant yield stress fluids show that thermal convection only started with the help of spurious bubbles, forced mixing or temperature heterogeneities at the top free surface (Balmforth and Rust [2009]). When we performed similar experiments with well controlled temperature conditions and no impurities in the fluid, an unstable linear conductive temperature gradient developed but motion never occured (even after three weeks). Most quantitative studies have therefore been limited to configurations where the onset of any motion would not require a critical threshold if the fluid was Newtonian: creeping motion of solid spheres (Beris et al. [1985]; Gueslin et al. [2006]; Putz et al. [2008]) and bubbles (Dubash and Frigaard [2004, 2007]), Saffman-Taylor instabilities (Coussot [1998]), Poiseuille flow (Frigaard et al. [1994]; Gabard and Hulin [2003])

[1]this section has been published in *Journal of Non-Newtonian Fluid Mechanics*, *Davaille et al. [2013]*

or Rayleigh-Poiseuille instabilities (Frigaard and Nouar [2003]; Martinand et al. [2006]; Metivier and Nouar [2008]).

Here, we investigate experimentally the development of thermal instabilities out of a localized heat source in a yield stress shear-thinning fluid (Carbopol solutions). This set up has been extensively used to study laminar Newtonian starting plumes (1975 Jr. and Luther [1975]; Olson and Singer [1985]; Campbell and Griffiths [1990]; Kaminski and Jaupart [2003]; Vatteville et al. [2009]; Davaille et al. [2011]). Combined Particle Image Velocimetry (PIV) and Thermochromic Liquid Crystals (TLC) visualizations allowed us to measure simultaneously the velocity and temperature fields (Davaille and Limare [2007]). As the heating power and the rheology of the experimental fluid were varied, different convective regimes and instability morphologies were observed. We focus here on their phenomenology and conditions of existence.

A.1.2. Experimental Setup and Fluids

A.1.2.1. Setup

The heat source consists of a Peltier element covered by a copper disk of thickness d=4 mm and radius R=12.5 mm. It is placed at the center of a square plexiglas tank 20x20x30 cm (fig.1a). The heater is fixed directly on the bottom surface (fig.1b). The upper fluid surface is free but there is a plexiglas lid on the tank to avoid evaporation and temperature fluctuations induced by the room. The room is kept at 21.0 ± 1.0^oC (the air-conditioning has a 15 to 20 min period) and the tank walls are 3 cm thick. This allows to filter the room temperature oscillations and to ensure a quiescent isothermal initial state in the tank. At time t=0, a constant power P_{elec} is applied to the heater. The ambient temperature and the temperature of the heater surface are measured by thermocouples and monitored through time, as well as the electric current voltage and intensity. Because of the non-linear response of the Peltier device, the thermal power P delivered into the fluid is not equal to the electric power supplied to the Peltier (Davaille et al. [2011]). However, for each experiment, an estimate of the thermal power actually delivered to the fluid can be computed using the Peltier element characteristics (see Annex 1).

The fluid is seeded with three types of encapsulated thermochromic liquid crystals (TLC), each reflecting light at a different temperature. A vertical cross-section of the tank is illuminated by a 532 nm laser sheet, and images are recorded every second using a CCD camera (fig. A.1). Depending on the temperature field, several bright lines can be seen on the images (fig.1), each of which represents a different "isotherm" (for details on the method see Davaille et al. [2011]). In our aqueous mixtures of carbopol, the TLCs sometimes also aggregate to form "particles" which scatter light, even without a temperature field (e.g. fig. A.5 and A.6). We therefore use these aggregates as tracer

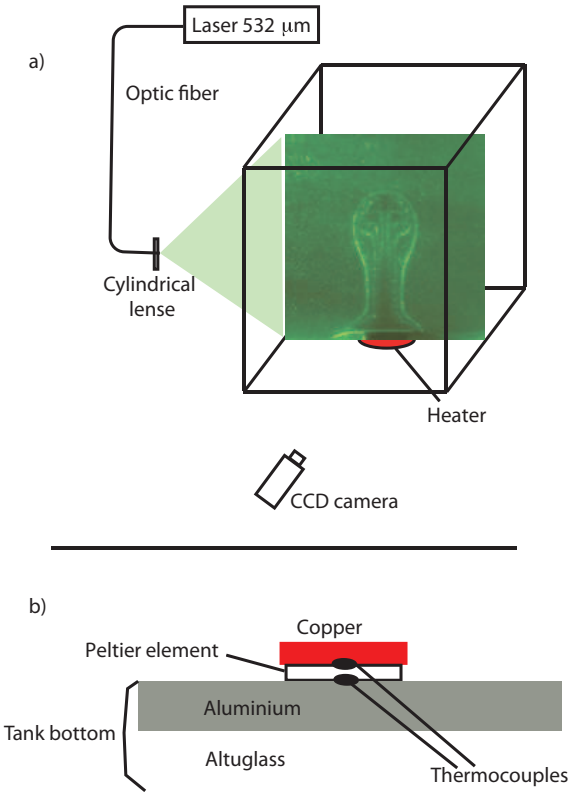

Figure A.1: a) Experimental set up. The heater is placed on the center of the bottom plate of the tank. At time t=0, the heater is switched on, and a thermal plume can develop. Here is shown an image of the thermal plumes obtained in Newtonian glucose syrups (e.g. Davaille et al. [2011]). The bright lines represent isotherms (see text). b) Close up on the heater configuration. The cold junction of the Peltier element is placed on an metallic plate to dissipate the cold, while the hot junction is in contact with the copper disk. We verified that the temperature on the copper disk was homogeneous (Vatteville et al. [2009]) and that the flow was not perturbed by the thermocouples.

particles and calculate velocity fields using Particle Image Velocimetry (PIV package from LaVision).

A.1.2.2. Fluids

The fluids are mixture of carbopol (Noveon ETD2050), distilled water and glycerin (between 0 and 56 wt%, see Table 1). The Carbopol powder (0.4-0.8g/L) was dispersed in the water-glycerin solvent for 2 days using a magnetic agitator. Then the solution was neutralized with a sodium hydroxide solution (5M). It was then left at rest for 8 days before use to ensure that the gel hydration was complete.

The TLCs were added once the tank is filled. For each fluid, the density and thermal expansion coefficient have been measured as a function of temperature between 15 and 65 ^{o}C with a Anton Paar DMA5000. Given the very small quantity of carbopol added, the other physical properties are those of the water-glycerin mixtures (Peixinho [2004]).

The rheological behavior of the fluids has been measured as a function of shear rate $\dot{\gamma}$ and temperature with a RS600 (ThermoHaake) and a MCR501 (Anton Paar). All measurements lead to a description of the fluid rheology with a Herschel-Bulkley model (Piau [2007]; Coussot et al. [2009]; Oppong and de Bruyn [2011]; fig. A.2):

$$\sigma = \sigma_0 + K_v \dot{\gamma}^n \tag{A.1}$$

where σ is the stress. The values of $\dot{\gamma}$ typically reached with the rheometer ranged between 10^{-4} and 10^2 sec^{-1}. The rheological parameters values given in Table 1 were obtained by fitting the descending part of the flow curve measured using a Couette geometry. Because the stresses generated by thermal buoyancy are small (see next section), we have to use solutions with very low yield stresses, which are delicate to measure. The existence of a real yield stress at very low values of $\dot{\gamma}$ is even still debated (e.g. Roberts and Barnes [2001]; Piau [2007]; Moller et al. [2006]). Overall, our flow curves become more noisy when $\dot{\gamma} < 10^{-2}$ sec^{-1}, which could be caused by wall slip and/or transitional effects (e.g. Piau [2007]). We therefore kept only the data which was reproducible, i.e. when $\dot{\gamma} > 10^{-2}$ sec^{-1}. Measurements on the same fluid, but with different apparatus, lead to variations in yield stress σ_0 of 30%. This large uncertainty is due to the low values of the yield stress. The exponent n is much more reliable, and varies between 0.50 and 0.63 (Table 1), which is in the range found in the literature (Roberts and Barnes [2001]; Peixinho [2004]; Divoux et al. [2010]). σ_0 and n do not show any significant variations with temperature (Peixinho [2004]), while the consistency K_v decreases by a factor of 2 for a temperature increase of 20^{o}C.

Table 1 summarizes the rheological parameters and the thermal properties of the various studied fluids. The addition of glycerin results in increasing the coefficient of thermal expansion, and in reducing the yield stress and the consistency compared to water with a similar quantity of carbopol.

Fluid	Glycerol wt%	Carbopol g/l	H mm	σ_0 Pa	n -	K_v Pa s^n	ρ_0 kg/m^3	α 10^{-4} K^{-1}	k W/m K
J1	56.5	0.4	180	0.037	0.63	0.345	1144	4.69	0.40
M2	0	0.8	180	0.35	0.5	1.57	999	2.10	0.58
M4	51.0	0.6	155	0.16	0.5	0.86	1129	4.89	0.41
J5	56.0	0.65	140	0.15	0.60	0.535	1142	4.61	0.40
J6	56.0	0.625	187	0.106	0.54	0.855	1142	4.61	0.40
S7	56.0	0.6	166	0.10	0.54	0.76	1142	4.62	0.40

Table A.1.: Fluid properties at 20^{o}C. Rheological properties: σ_0 yield stress, n shear-thinning index, K_v consistency. Thermal properties at 20 ^{o}C: ρ density , α thermal expansion , thermal conductivity k.

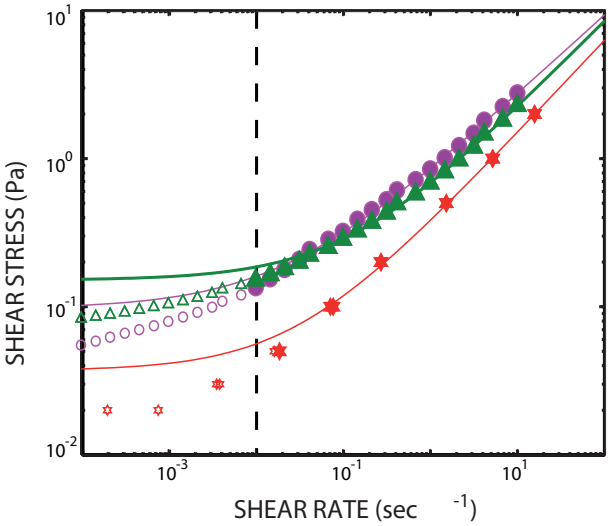

Figure A.2: Flow curves measured for three fluids, J1 (red stars), J5 (green triangles) and S7 (magenta disks) and their fits by a Herschel-Bulkley law (solid lines). For the fits, only the measurements for shear rates above 10^{-2} have been considered (see text).

A.1.2.3. Parameters

Given our experimental set up and the rheology of the fluid, several parameters are needed to characterize the system (e.g. Zhang et al. [2006]; Balmforth and Rust [2009]):

-the box aspect ratio L/H, where H is the fluid height in the tank and L its width. Here L/H ranged between 0.83 and 1.21 depending on the runs.

- the size aspect ratio between the heater and the box R/H, which varied between 13.3 and 19.4 depending on the runs.

- the Reynolds number can be estimated using (e.g. Dubash and Frigaard [2007]):

$$Re = \frac{\rho R^n W^{2-n}}{K_v} \tag{A.2}$$

where W is the velocity. It never exceeds 1 mm/sec in our experiments, so that $Re < 0.01$ and the instabilities are always in the creep regime.

-the Bingham number Bi compares the yield and viscous stresses in (A.1):

$$Bi = \frac{\sigma_0}{K_v \dot{\gamma}^n} \tag{A.3}$$

When motions are observed, the measured typical shear rates range between 10^{-6} and 0.05 sec^{-1}. This implies Bi between 0.6 and 1000.

-the yield parameter Y_0 compares the yield stress to the stress induced by the thermal density anomaly σ_{th}:

$$Y_0 = \frac{\sigma_{th}}{\sigma_0} = \frac{\alpha \rho g P}{\sigma_0 k} \tag{A.4}$$

since for a constant power supply , the hot pocket of fluid applies under the action of gravity a stress which scales as $\sigma_{th} \sim \alpha \rho g P/k$. In a yield stress fluid initially at rest, the hot pocket will be able to rise only if σ_{th} is greater than the yield stress (e.g. Beris et al. [1985]; Dubash and Frigaard [2004, 2007]; Tabuteau et al. [2007]; Balmforth and Rust [2009]). So, Y_0 is the key parameter to determine the onset of convection.

Owing to the small values of the thermal expansion coefficient, and to the maximum temperature difference that the system can encounter without generating bubbles, the thermally induced stresses are small. Therefore, convective instabilities are expected only for rather small yield stresses (Table 1). Using 6 different fluids (see Table 1) and varying the electric power input between 0.02 and 6.5 W, we run 62 experiments with σ_{th} ranging from 1.5 to 80, leading to Yield parameters between 20 and 1600 (fig. A.3). The typical duration of an experiment ranged between 30 minutes and four days.

A.1.3. Three Different Regimes

Once the heat source is turned on, a pocket of hot fluid first grows by diffusion around the heater (fig. A.6a). Then depending on the applied thermal stress and the yield

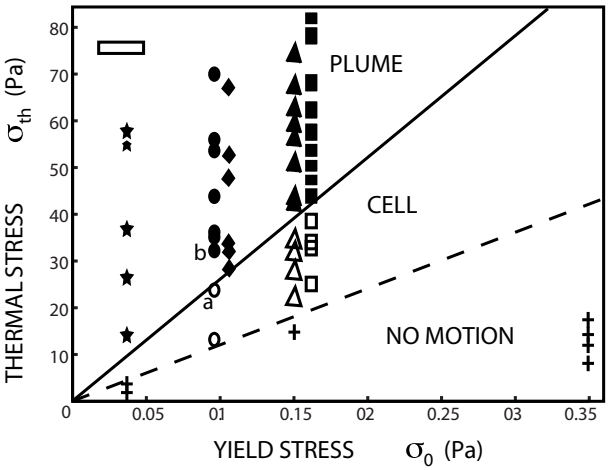

Figure A.3.: Phase diagram as a function of the yield stress σ_0 and of the stress of thermal origin σ_{th}. Filled symbols stand for the plumes, empty ones for convection confined around the heater, and crosses for no convection. The solid line represents $Y_{c2} = 260$ and the dotted line $Y_{c1} = 120$. Stars stand for fluid J1, disks for S7, diamonds for J6, triangles for J5, and squares for M4. The empty black rectangle in the top left corner shows the uncertainty on the stresses. "a" points toward an experiment without any plume even after four days while experiment "b" generated a plume in less than 30 min.

stress of the fluid, three different regimes occur. Fig. A.3 shows that the transition between the different regims depends primarily on the Yield parameter. For Y_0 smaller than $Y_{c1} = 120(\pm 15)$, no motion was detected. For moderate Y_0 ($Y_{c1} < Y_0 < Y_{c2}$, $Y_{c2} = 260(\pm 20)$), small scale convection cells remain confined around the heater (fig. A.5). For $Y_0 > Y_{c2}$, plumes develop (fig. A.6). The transition at $Y_0 = Y_{c2}$ is quite sharp: on fig. A.3, experiment "a" did not show any plume even after four days while experiment "b" generated a plume in less than 30 min.

A.1.3.1. No Motion

For low thermal powers, no motion is recorded: a drop of dye will remain at its initial position, and the presence of rising bubbles neither starts the flow nor perturbs the temperature field. A steady state temperature structure develops by conduction and the heater temperature compared to the initial fluid temperature scales as $\Delta T = P/4kR_{eff}$ (Carslaw and Jaeger, 1959, p215). Given the geometry of the heater (fig.1b), we can take $R_{eff} \sim R + d$. The fluid behaves as a solid and due to thermoelasticity, the temperature gradient can produce elastic deformations. Until the heater has reached steady state, the thermoelastic stresses σ_{TE} will build up. According to linear thermoelasticity (Landau and Lifshitz [1986]) , σ_{TE} should scale as:

$$\sigma_{TE} = C_0.\Delta T.\frac{\alpha.E_Y}{1-2\nu_p} \tag{A.5}$$

where ν_p is the Poisson ratio, $E_Y = 2(1+\nu_p)G'$ is the Young modulus, G' is the elastic modulus and C_0 is a constant which depends on the geometry of the set up.

As long as σ_{TE} remains smaller than the yield stress, no viscous flow can occur. The first critical value of the yield parameter Y_{c1} therefore corresponds to $\sigma_{TE} \sim \sigma_0$, which according to (A.4) and (A.5) gives:

$$Y_{c1} \sim \frac{\rho.g.(R+d)}{C_0.G'}.\frac{2(1-2\nu_p)}{(1+\nu_p)}. \tag{A.6}$$

Equation (A.6) shows that the first transition Y_{c1} depends on the fluid properties and the set up geometry. We do not see variations in the experiments presented here because we are always using the same set up (same R, d and C_0) and fluids which are quite similar. We were not able to measure the elastic modulus at the time of the experiments, but since then, rheometry measurements performed on similar solutions (Massmeyer et al, in prep.) gave us elastic modulus estimates between 0.5 and 3 Pa, similar to values obtained in pure water-carbopol solutions (Oppong and de Bruyn [2011]; Gutowski et al. [2012]). The Poisson ratio for Carbopol solutions is unknown, but we expect it to be close to an incompressible liquid, i.e. between 0.4 and 0.5. Fig. A.4 then shows that the predicted values of Y_{c1} are close to the observed ones (120 ± 15) for constant C_0 between 0.2 and 1.

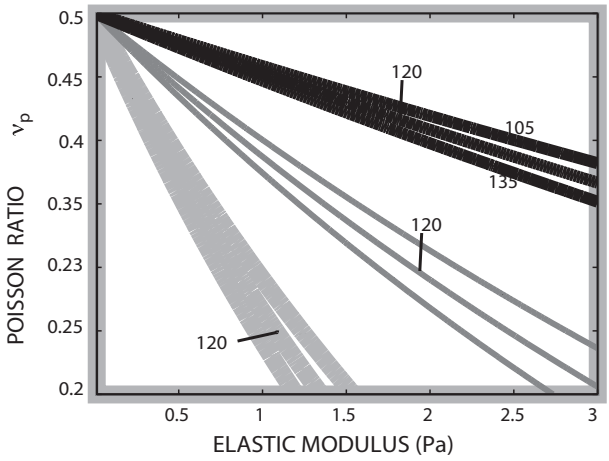

Figure A.4: Value of Y_{c1} predicted by equation (A.6) as a function of the elastic modulus and the Poisson ratio, for three different values of C_0 (or set ups) and ρ=1142 kg/m^3. The heavy grey lines represents C_0=1, the thin grey lines C_0=0.5, and the thick black lines C_0=0.2. The numbers indicate the Y_{c1} values of 120±15.

A.1.3.2. Cellular Convection

Fig. A.5 shows the convective pattern obtained for intermediate Y_0: after 3 hours of experiment, the temperature structure around the heater has reached its steady state (fig. A.5b-e) for the isotherms $\leq 31°$ C. The isotherms closer to ambient temperature take longer to stabilize (about a day) but no plume will ever developed (even after four days, fig. A.5e). However, on 30 min time-scale, very slow particle motions (typically 2 to 3 orders of magnitude slower than in the plume cases) are detectable within the hot pocket around the heater (fig. A.5f). Dyed areas in the fluid are continuously deformed under the action of the viscous flow as seen on fig. A.5. This is radically different from their behaviour in the previous elastic regime, and shows that the velocity we computed indeed represents motion and not elastic deformation. The very low velocity results in a very low Peclet number ($Pe = W\,R/\kappa \sim 0.1$), which implies that advection is negligible compared to diffusion of heat in the conservation of energy equation. Therefore, only solving the heat conduction equation (ignoring the advection) predicts quite well the thermal structure (fig. A.5e): only the 24.6 ^{o}C isotherm is broader than predicted by the analytical solution, which is compatible with the temperature homogeneization in the core of a convective cell.

A.1.3.3. Plumes Development

Fig. A.6-A.9 show the development of a hot instability when $Y_0 > Y_{c2}$. First, the hot pocket grows by diffusion around the heater and the particles record no motion ($t <$ 200 sec on fig. A.7 and fig. A.9). Then slow motions can be detected within the hot fluid pocket for $200 < t < 500$ sec, although the growth of the latter is still dominated by heat conduction (fig. A.6a). It is impossible to determine exactly when the transition for no motion to the small convective cell occurs since the detection of very low velocities requires correlation between images 50 to 250 sec apart! However the transition to the

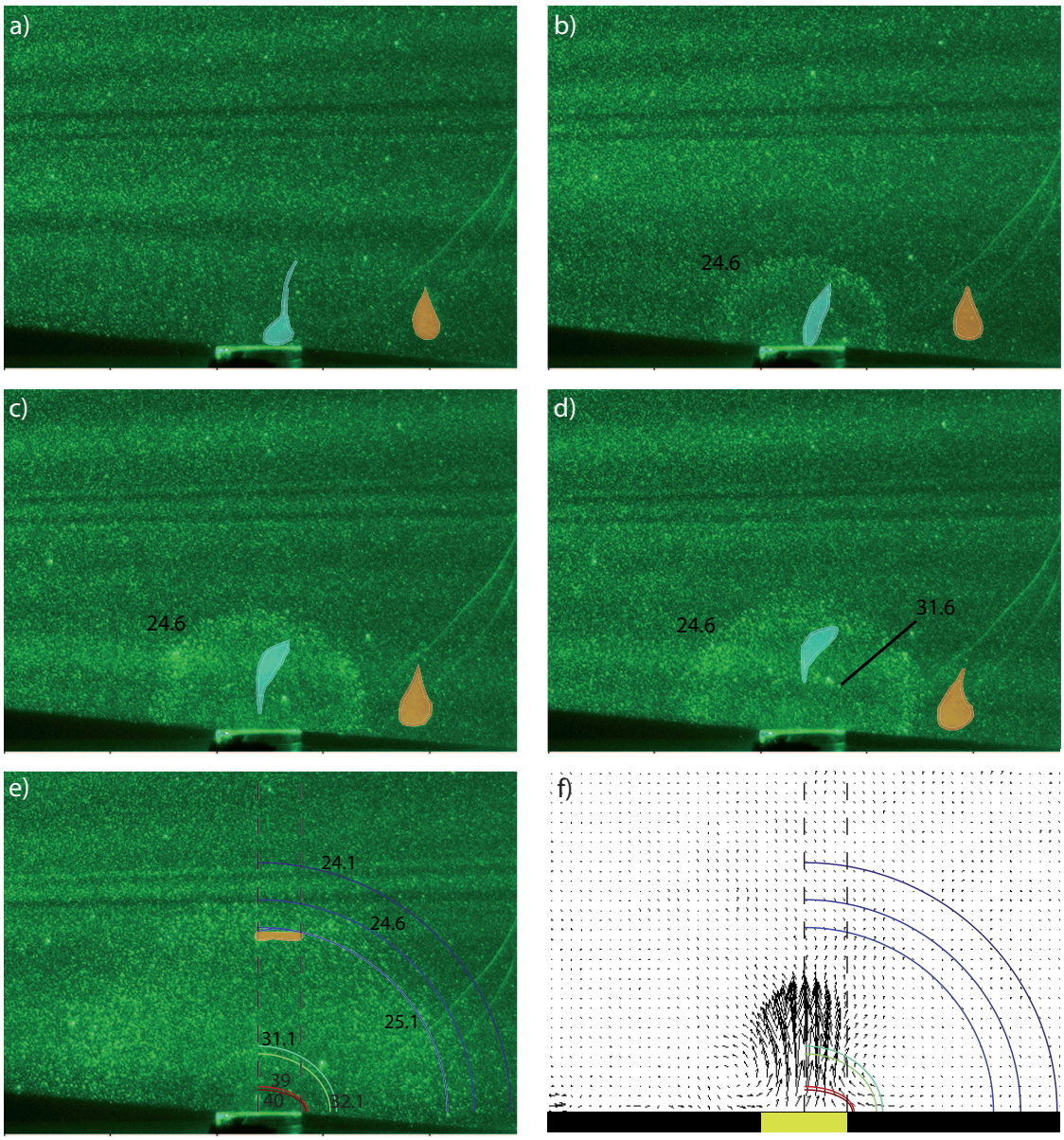

Figure A.5.: Images for the cellular regime (fluid S7 at P=1.85 W, Y_0=247). a) t=0. Two dyed drops of fluid have been outlined in orange and green. b) t=2000 sec. The isotherms (values indicated in black) appear as bright linear zones and their thickness reflects the local temperature gradient; c) t=6000 sec.; d) t=12000sec. ; e) t=3.2×10^5 sec. Superimposed is the analytical solution for the steady state in pure conduction (Carslaw and Jaeger [1959]). The values of the isotherms are indicated in ^{o}C. The orange drop is now stretched in an horizontal bar, and the green drop has been stretched in a filament that we cannot distinguish from the isotherm anymore. f) velocity field obtained for e) with PIV (cross-correlation of images 250 sec. apart). The maximum velocity is 1.3×10^{-6} m/s. The fluid colder than isotherm 24.1^{o}C remains unyielded. Significant velocity remains confined around the heater.

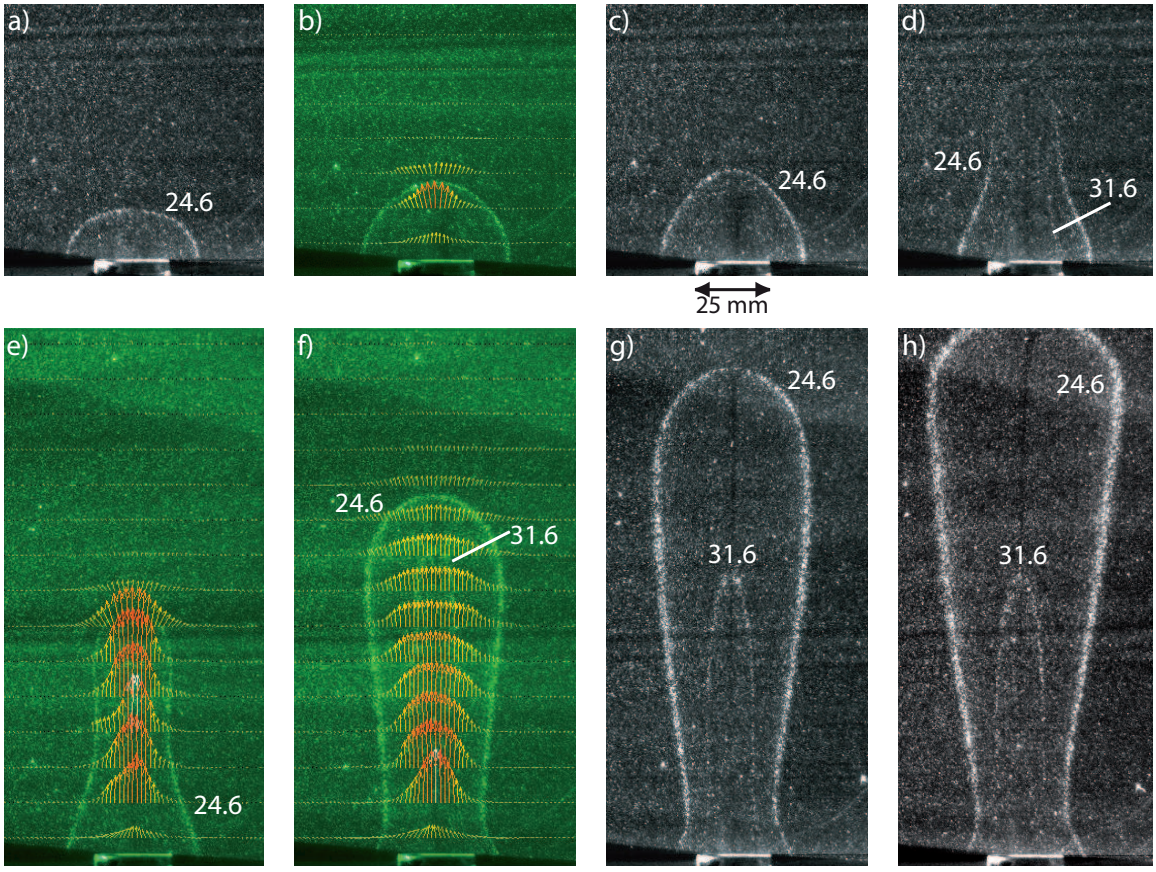

Figure A.6.: Development of a plume (fluid S7 at P=4.15 W, Y_0=554). The bright lines are the TLCs isotherms: a) t=300 sec; b) t=532 sec. The colours arrows show the vertical component of the velocity field W_z. They are superimposed on the raw image. The same colour scale has been applied for images b), e) and f). The maximum W_z (in white) is 0.38 mm/sec ; c) t=560 sec; d) t=600 sec; e) t=652 sec; f) t=1140 sec; g) t=1700 sec; h) t=2200 sec. The velocity fields were calculated with PIV using cross-correlation of images 5 sec. (b) to 1 sec.(c-h) apart.

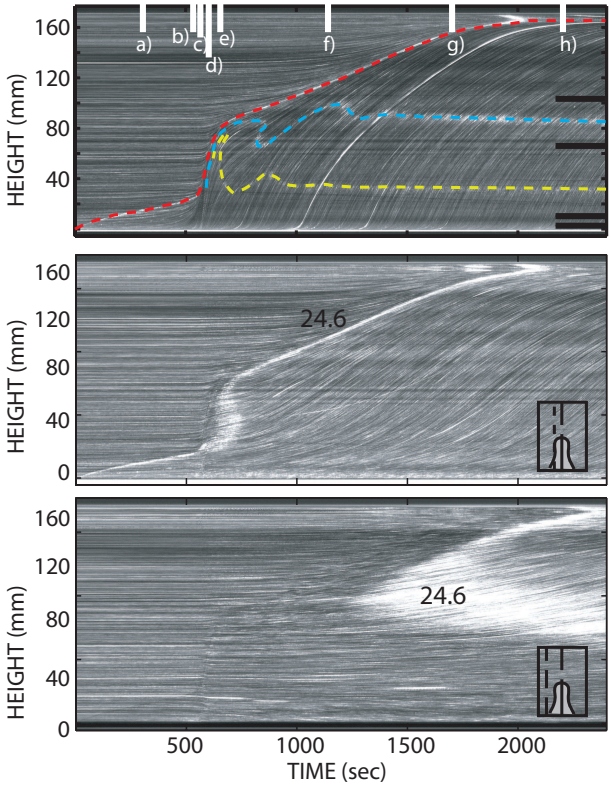

Figure A.7: Development of a plume (same as fig. A.6). Light intensity of the pixels line: a) along the plume axis (r=0) as a function of time and height. The isotherms have been highlighted in red (24.6^{o}C), blue (31.5^{o}C) and yellow (39.5^{o}C). We can also follow the particles as they rise along the axis. After a stage where the heat transfer in the fluid is mainly by conduction, the plume rises quickly around 550 sec. The white vertical bars correspond to the snapshots of fig. A.6 and the black horizontal bars to the horizontal cross-sections in fig. A.9. b) vertically above the heater edge (r=12.5 mm). c) vertically above r=25 mm. The numbers in black indicate the isotherm value.

plume formation is very easy to spot. For $t > 500$ sec, a finger of hot fluid emerges from the hot pocket (fig. A.6b-d). It rises in two phases, quickly at first, and then at a steady slower pace (fig. A.7,A.8). Close inspection of the isotherms inside the plume shows that their heights oscillate through time before becoming constant. And so is the velocity field (fig. A.8). Nevertheless, in these experiments, all the plumes eventually reach the surface.

Transition from Cellular Convection to Plume:

The departure of the hot instability is quite sudden: it corresponds to the fast uplift of the isotherms on the vertical spatio-temporal diagram (fig. A.7) and to the necking of the isotherms close to the heat source on the horizontal spatio-temporal diagrams (arrows on fig. A.9c,d). It also coincides with the maximum temperature recorded on the heater (fig. A.8a) since heat is suddenly removed from the heater surface when the plume starts. As it is the thermal power which is kept constant and not the heater temperature, the latter decreases in response to motion. We define here the instability "onset time" t_c as the necking time. Other definitions based on the isotherms uplift or on the heater temperature give slightly different measurements (variations of less than 3 %) but the overall trend remains unchanged.

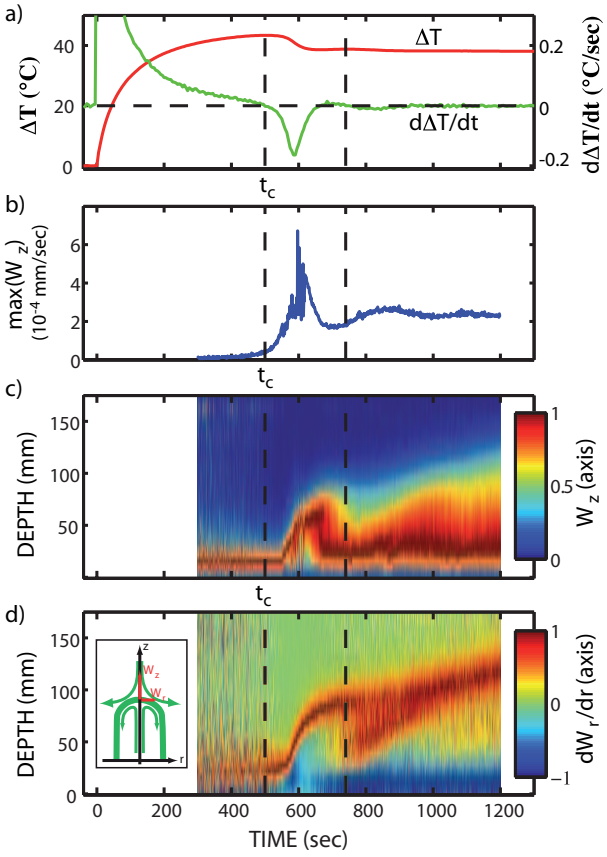

Figure A.8: Development of a plume (same as fig. A.6). a) Temperature difference ΔT between the Peltier heater and the bulk fluid (red curve) and its time-derivative as a function of time. b) maximum vertical velocity W_z recorded on the plume axis. c) Vertical velocity along the plume axis normalized by its maximum at each time, as a function of depth and time. d) dW_r/dr along the plume axis normalized by its maximum at each time, as a function of depth and time. Its maximum corresponds to the stagnation point at the top of the plume (inset). The two vertical dashed lines show the onset time and the second uplift event (cf. text).

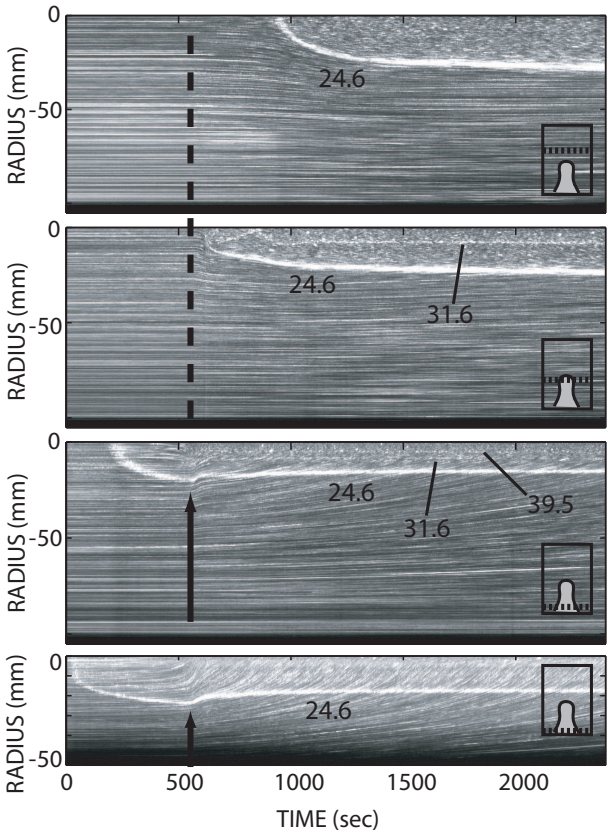

Figure A.9: Development of a plume (same as fig. A.6). Light intensity of the pixels line along a radius as a function of time at four different depths z: a) $z = 102.1$ mm; b) $z = 66.5$ mm; c) $z = 12.1$ mm; d) $z = 3.2$ mm. The black arrows indicate the "necking" time used to define the plume onset time (see text). The insets show where is the cross-section relative to the tank.

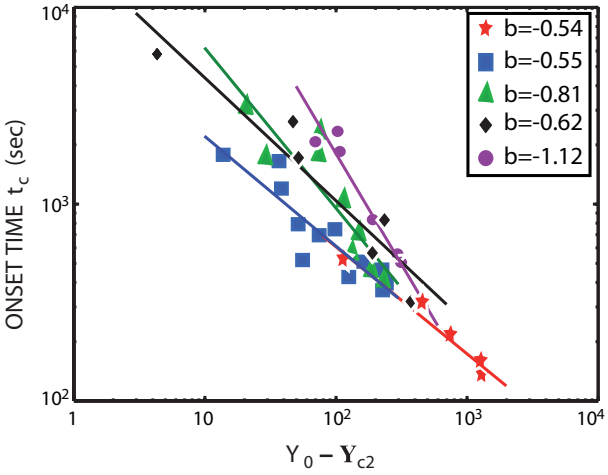

Figure A.10: Plume dimensionless onset time as a function of the Yield parameter. The same symbols as in fig.3 have been used for the different fluids. The thick dashed line corresponds to $Y_{c2} = 260$. To each fluid (and set of rheological parameters), correspond one of the thinner lines, which outlined the trend followed by the data points.

Fig. A.10 shows the onset time as a function of $Y_0 - Y_{c2}$. As expected, the closer to the Y_{c2} transition, the latest the onset time. For each fluid, the data points can be fitted with a power law

$$t_c = a(Y_0 - Y_{c2})^b, \tag{A.7}$$

but we could not find any rationale between the coefficients a and b and the physical properties of the fluids.

Y_{c2} is much higher than the one reported for sedimentation of solid spheres ($Y_c = 6.85$, Beris et al. [1985], Tabuteau et al. [2007]) or bubbles (Dubash and Frigaard [2004, 2007]). However, in the latter case, the yield number is defined as $Y = g.D.\Delta\rho/3\sigma_0$, where D is the sphere diameter, and $\Delta\rho$ its density excess. In our case, buoyancy is produced by the temperature differences and $\Delta\rho = \alpha\rho\Delta T_{av}$. Since we know the temperature field for each experiment, we therefore can calculate at each time the averaged temperature excess ΔT_{av} contained in the hot pocket of fluid around the heater. We can also calculate the effective radius of a sphere that would have the same volume, and so we finally can estimate Y. To define what constitutes the "hot pocket", we choose all the fluid with a temperature excess greater than 0.1 ΔT. Then the boundary between the cellular convection and the plume formation occurs for $Y = 8.8 \pm 0.7$. This value now is of the same order as Y_c. That the two values are different are expected since we have a bottom rigid boundary condition instead of a free surface (as in the experiments for the sphere) and since the geometry of the rising plume is different from a sphere, on which the critical Yield parameter value might depend (Dubash and Frigaard [2004, 2007]).

Episodicity

We have already mentioned the strong time-dependence of the plumes, whereby the temperature and velocity fields fluctuate before reaching steady state (fig. A.7,A.8). In some cases (fig. A.11), the plume completely stops and cools down. Then a second pulse

is registered. We could distinguish up to 3 pulses before the steady-state is reached with time lapse between two pulses ranging from 140 to 1000 sec. Given the long time-scales involved, this is not due to the elasticity of the fluid (as seen in falling motions of solid spheres for exemple, i.e. Tabuteau et al. [2007]), but it is due to instabilities in the plume conduit. Such instabilities have already been reported for Newtonian fluids (e.g. Olson et al. [1993]; Vatteville et al. [2009]; Davaille et al. [2011]) and shear thinning fluids (e.g. van Keken [1997]) although their origin remains unknown. Here, we notice that the velocity of the first pulse is much higher than the steady state velocity in the plume conduit, and that the amplitude of the velocity variations is decreasing through time (fig. A.8b). The steady state represents the hot flow that the heat source is able to support continuously. Since it needs to penetrate unyielded material, the first pulse is the most buoyant (i.e. the hottest) and carry more buoyancy than what is produced continuously. Therefore the plume head start drains the source and almost detach from it. However, as it rises, it looses its heat by conduction (i.e. Batchelor [1954]), until its local buoyancy cannot overcome anymore the yield stress, which explains its strong slow down, or even arrest (fig. A.11). Meanwhile, the thermal boundary layer around the heater is building again until a new pulse starts. In the referential of the rising plume, its tip is characterized by a stagnation point where dW_r/dr is maximum (fig. A.8d, Davaille et al. [2011]). We see clearly on fig. A.11d and fig. A.11 that the second pulse also bears this characteristic signature and starts from the bottom of the tank. However, as it is following the conduit previously built, it needs carrying less buoyancy that the first pulse, therefore its velocity is smaller, closer to what the heat source can sustain continuously. The system therefore will approach steady state by a serie of pulses decreasing in amplitude.

Plume Morphology and Plug Flow:

In newtonian fluids, hot less viscous plumes entering a colder and more viscous environment are mushroom-shaped (e.g. fig. A.1), while cold more viscous plumes are finger-shaped (Jr. and Luther [1975]; Olson and Singer [1985]). The morphology of the hot and less viscous plumes observed in our experiments is therefore significantly different from the newtonian case. On the other hand, intrusion of fluid in elastic matrices like gelatin or rocks are known to produce columnar or 2-D dikes shapes (i.e. Menand and Tait [2001]).

A close inspection of the velocity field (fig. A.6e-f) reveals that the upwelling material is entirely confined within the thermal anomaly. Moreover, the velocity radial profiles around the plume axis are quite flat (fig. A.6f). As a measure of the shear rate, we can calculate the second invariant of the strain rate tensor from the velocity field (W_r, W_z). For an axisymmetric configuration, it writes:

$$\dot{\gamma_0} = [(\frac{dW_r}{dr})^2 + \frac{W_r^2}{r^2} + (\frac{dW_z}{dz})^2 + \frac{1}{2}(\frac{dW_z}{dr} + \frac{dW_r}{dz})^2]^{1/2} \tag{A.8}$$

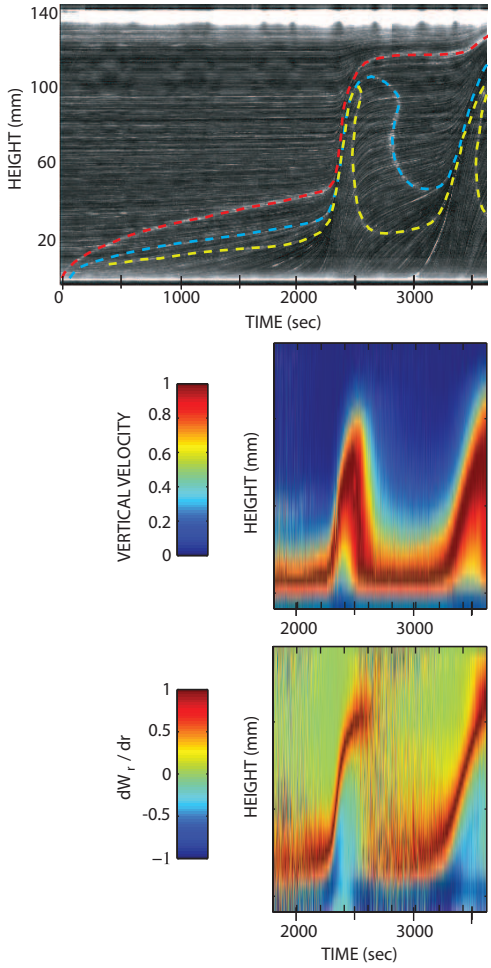

Figure A.11.: Strong plume episodicity (fluid J5 at P=3.9 W, Y_0=333) . a) Light intensity of the pixels line along the plume axis (r=0) as a function of time and height. The isotherms have been highlighted in red (24.6^{o}C), blue (31.5^{o}C) and yellow (39.5^{o}C). b) Vertical velocity along the plume axis normalized by its maximum at each time, as a function of depth and time. c) dW_r/dr along the plume axis normalized by its maximum at each time, as a function of depth and time. After the conduction stage, the plume rises quickly at 2200 sec until it stops completely and cools down. Then a second pulse is recorded, starting around 3100 sec.

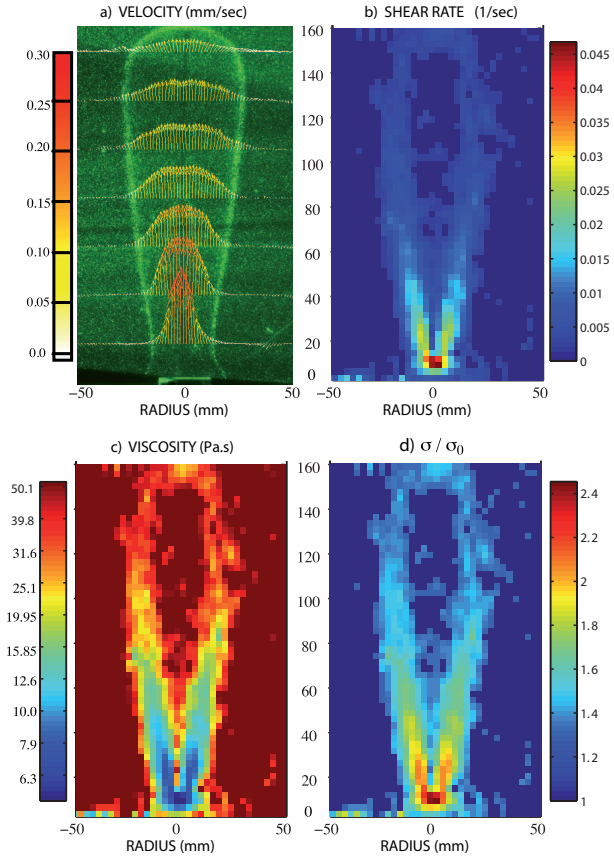

Figure A.12: Vertical cross-section of the plume structure at t=2000 sec ((same plume as fig. A.6)). a) Vertical velocity, b) shear rate according to equation (A.8), c) viscosity calculated with $\eta = \sigma/\dot{\gamma}_0$, d) shear stress normalized by the yield stress. Dark blue areas are for shear rates below the detection level and are therefore probably unyielded.

Fig. A.12b shows the map of the characteristic shear rate for $t = 2000$ sec.: the shear rate in most of the plume axis region is zero (within the uncertainties on the shear rate field). So the fluid there is not sheared but moves up as a plug. This shear localization is characteristic of a yield stress fluid and is commonly observed in pipe flows (e.g. Gabard and Hulin [2003]). Moreover, even when the velocity along the axis has reached its steady state, the plume conduit thermal anomaly enlarges slowly with time (fig. A.9a,b): this is due to the progressive erosion by the plume flow of the solid part of the fluid. As seen in rheometry measurements (Baudez and Coussot [2004]; Divoux et al. [2010]), we observe the slow outward propagation of the interface between the two phases (fig. A.6g-h, fig. A.9a-b). However, a region of plug flow always remains along the plume axis (fig. A.12), and the plume shape remains columnar.

A.1.4. From Solid to Flowing Behaviour

The development of the thermal instabitities reported here always goes through three phases: first thermo-elastic deformation, then very slow creep where heat transfer is still dominated by conduction and the Bingham number (equation (A.3)) remains high, and

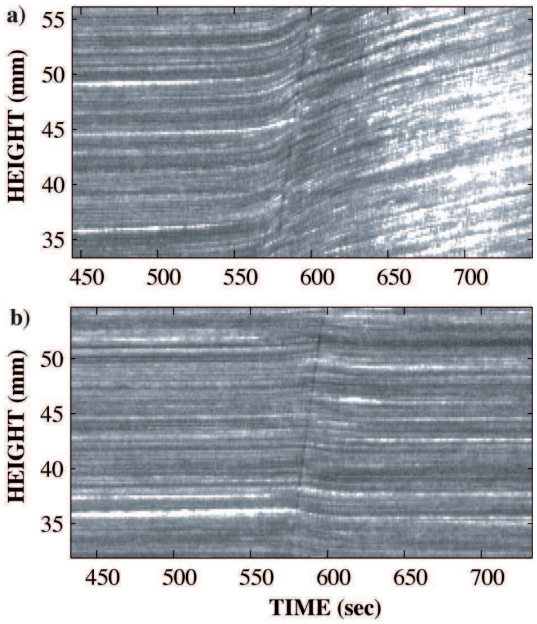

Figure A.13: Development of a plume (fluid S7 at P=4.15 W, Y_0=554). Zoom on the vertical spatio-temporal evolution off axis: a)r=12.5 mm, and b) r=25 mm. Note that the offset is towards the top for a) which means that the material is rising, while it is downwards for b), which means that the downwards return flow is close to the plume.

finally the sudden rise of a hot finger, with strong shear localization. This behaviour is reminiscent of the sequence of events reported in recent rheometry creep experiments using carbopol (Caton and Baravian [2008]; Divoux et al. [2010]). Those experiments were investigating the transition to fluidization of a sample when a constant stress was applied. In our case of heating at constant power, the applied stresses, due to the building temperature, are increasing through time till the system reaches steady state. However, in both systems, fluidization involves an episode of strong shear localization and/or shear banding. Divoux et al. [2010] observed total slip on the wall of the apparatus, prior to the establishment of steady shear, while Caton and Baravian [2008] suggested the presence of fractures.

On fig. A.7 and fig. A.9, horizontal bright lines represent particles at rest (i.e. unyielded areas), and continuous oblique lines moving particle trajectories (yielded areas). However, in between the two zones, that is just before onset and around the plume thermal anomaly, there exists a more chaotic zone, which propagates as the plume rises. fig. A.13 presents a zoom on the particles trajectories during the stage of fast uplift of the plume: at the 0.1 mm scale, the trajectories of the particles around the hot thermal anomaly are not continuous but show sudden offsets, as if a damaged zone was developing around the plume. Studies of the microscopic structure of Carbopol solutions show that they are concentrated suspensions of swollen polymer "sponges" with typical size 5-20 μm size (Piau [2007]; Gutowski et al. [2012]). So the fact that we are able to see at the 0.1-0.5 mm scale the intermittent sudden disruptions suggests that the transition from solid to flowing behaviour may occur through intermittent plastic events correlated over a finite size area, as proposed by recent models (e.g. Picard et al. [2005]). However, we are lacking

resolution, both in time and space, to tell if those events are fractures or slip of one gel particles aggregate onto another one.

A.1.5. Conclusions

We have conducted experiments on thermal instabilities in yield stress fluids. The Yield parameter, the ratio of stresses of thermal origin over the yield stress, is shown to be the key parameter to predict the convective regime. Given the small value of the thermal expansion coefficient, leading to weak thermal stresses, plumes will develop only for very low yield stresses and will involve weak shear rates ($\leq 2.10^{-2}$ sec^{-1}). However, their morphology and dynamics are markedly different from those of a Newtonian plume, and unyielded areas coexist with flowing regions. Further work is now under way to quantify the characteristics of plume dynamics, the damage zone extent and the transition from solid to flowing behaviour.

A.1.6. Appendix: Determination of the Thermal Power Delivered by the Peltier Heater

A Peltier element develops a temperature difference between its two surfaces, $\Delta T = T_{hot} - T_{cold}$, when it is fed with a current of intensity I. The thermal power P delivered on the hot surface then writes:

$$P = S_p.I.T_{hot} + \frac{1}{2}I^2.R_p - K_p.\Delta T \tag{A.9}$$

where S_p is the Seebeck coefficient, R_p is the electric resistance, and K_p the thermal conductivity. Since we measure the temporal evolution of the voltage U and intensity I, we can determine for each experiment S_p and R_p through:

$$U = R_p.I + S_p.\Delta T \tag{A.10}$$

and

$$R_p = \frac{U - S_p.\Delta T}{I} \tag{A.11}$$

At the end of each experiment, the intensity is switched off but because the temperature difference takes some time to vanish, a residual voltage is measured, which decreases through time, and which is indeed proportional to ΔT. According to equation (A.10), this gives us a measure of S_p, which is found to be constant through all the experiments: S_p=0.023 Volts/^{o}K.

Then, using equation (A.11), the resistance is determined for each time. It is found that R_p slightly varies with temperature, in agreement with the manufacturer.

B. 3D Visualization of the temperature

B.1. Flowchart: 3D-Isotherm-Script

Here the different steps, how to isolate and visualize the isotherm, are summarized in a flowchart (fig. B.1. In a first step the brightest isotherm is isolated for every picture Image(i). First the first picture Image0(i) is subtracted to get rid of noise (e.g. reflections at the sides). Then several filters are applied to get rid of other bright reflections, e.g. reflections from PIV-particles and less bright isotherms. Then the gradient of the image is calculated. It is pointing "away" from the isotherm and its value is around zero on the isotherm. Thus the isotherm is defined as the point where the gradient is around zero and the local intensity is higher than a previously defined threshold value. On a new matrix all points that full fill the criterion are set to *one*, all other points are set to *zero*.
To create a 3D-plot of the brightest isotherm a mesh needs to be defined. In the easiest case this can be done with meshgrid. However, the laser sheet prescribes an angle and therefore the scanned area is small on the side where the laser sheet enters the box and then increases to the other side. To take account correct for this deformation, the grid can be calculated using *pol2cart, meshgrid* and *TriScatteredInterp*. The drawback is, that *TriScatteredInterp* is very RAM- and time-consuming.
For the plotting all values equal to *1* are patched onto the grid (*patch*) and then plotted with isonormals. For better visualization isocolors may be used, e.g. to colorcode the height (as in fig. 2.3)

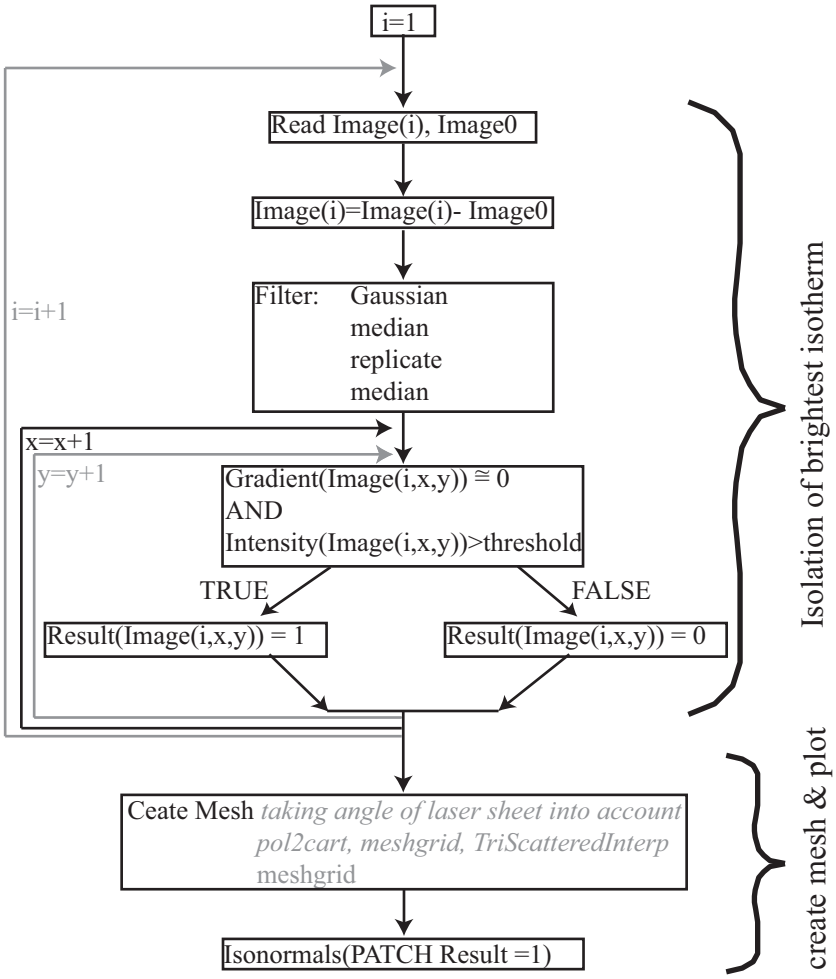

Figure B.1.: Flowchart of how to isolate the brightest isotherm of each Image(i), creation of mesh and the subsequent isosurface plot combining all images. *pol2cart, meshgrid* and *TriScatteredInterp* are used used if correction to the angle of the laser sheet is applied. If distortion is ignored, only meshgrid is used to create the mesh.

Bibliography

A. N. Alexandrou, T. M. McGilvreay, and G. Burgos. Steady herschel-bulkley fluid flow in three-dimensional expansion. *J. Non-Newton. Fluid Mech.*, 100:77–96, 2001.

S. Androvandi, A. Davaille, A. Limare, A. Foucquier, and C. Marais. At least three scales of convection in a mantle with strongly temperature-dependent viscosity. *Phys. Earth Planet. Inter.*, 188:132–141, 2011.

Q. Bai, S. J. Mackwell, and D. L. Kohlstedt. High-Temperature Creep of Olivine Single Crystals: 1. Mechanical Results for Buffered Samples. *J. Geophys. Res.*, 96:2441–2463, 1991.

N. J. Balmforth and A. C. Rust. Weakly nonlinear viscoplastic convection. *J. Non-Newton. Fluid Mech.*, 158:36–45, 2009.

A. C. Barr, R. T. Pappalardo, and S. Zhong. Convective instability in ice I with non-Newtonian rheology: Application to the icy Galilean satellites. *J. Geophys. Res.*, 109: E12008, 2004.

G. K. Batchelor. Heat convection and buoyancy effects in fluids. *Q. J. R. Meteorolog. Soc.*, 80:339–358, 1954.

J. C. Baudez and P. Coussot. Abrupt transition from viscoelastic solidlike to liquidlike behavior in jammed materials. *Phys. Rev. Lett.*, 93:128302–1 – 128302–4, 2004.

L. Bellon, M. Gibert, and R. Hernandez. Coupling between aging and convective motion in a colloidal glass of laponite. *Eur., Phys. J. B*, 65:101–107, 2007.

H. Bénard. *Les Tourbillons cellulaires dans une nappe liquide propageant de la chaleur par convection, en régime permanent.* Gauthier-Villars, 1901.

D. Bercovici. Plate generation in a simple model of lithosphere mantle flow with dynamic self-lubrication. *Earth Planet. Sci. Lett.*, 144 (1-2):41–51, 1996.

D. Bercovici. The generation of plate tectonics from mantle convection. *Earth Planet. Sci. Lett.*, 205:107–121, 2003.

A. N. Beris, J. A. Tsamopoulos, R. C. Armstrong, and R. A. Brown. Creeping motion of a sphere through a Bingham plastic. *J. Fluid Mech.*, 158:219–244, 1985.

E. C. Bingham. An investigation of the laws of plastic flow. *Bulletin of the Bureau of Standards*, 13:309–353, 1916.

D. Bittner and H. Schmeling. Numerical modelling of melting processes and induced diapirism in the lower crust. *Geophys. J. Int.*, 123:59–70, 1995.

J. R. Booker. Thermal convection with strongly temperature-dependent viscosity. *J. Fluid Mech.*, 76:4:741–754, 1976.

W. R. Buck, P. Einarsson, and B. Brandsdòttir. Tectonic stress and magma chamber size as controls on dike propagation: Constraints from the 1975-1984 Krafla rifting episode. *J. Geophys. Res.*, 111:B12404, 2006.

S. L. Burgess and S. D. R. Wilson. Spin-coating of a viscoplastic material. *Phys. Fluids*, 8:2291–2297, 1996.

E. B. Burov and A. B. Watts. The long-term strength of continental lithosphere: "jelly sandwich" or "crème brûlée"? *GSA today*, 16:4–10, 2006.

I. H. Campbell and R. W. Griffiths. Stirring and structure in mantle starting plumes. *Earth Planet. Sci. Lett.*, 99:79–93, 1990.

H.S. Carslaw and J.C. Jaeger. *Conduction of Heat in Solids*. Oxford Univ. Press, 1959.

F. Caton and C. Baravian. Plastic behavior of some yield stress fluids: from creep to long-time yield. *Rheol. Acta*, 47:601–607, 2008.

S. Chandrasekhar. *Hydrodynamic and hydromagnetic stability*. Oxford, Clarendon Press, 1961.

P. N. Chopra and M. S. Paterson. The role of water in the deformation of dunite. *J. Geophys. Res.*, 89(B9):7861–7876, 1984. ISSN 2156-2202. doi: 10.1029/JB089iB09p07861. URL http://onlinelibrary.wiley.com/doi/10.1029/JB089iB09p07861/abstract.

U. Christensen and H. Harder. 3-D convection with variable viscosity. *Geophys. J. Int.*, 104:213–220, 1991.

U. R. Christensen. Heat transport by variable viscosity convection and implications for the earth's thermal evolution. *Phys. Earth Planet. Inter.*, 35:264–282, 1984.

P. Cordier, J. Amodeo, and P. Carrez. Modelling the rheology of MgO under Earth's mantle pressure, temperature and strain rates. *Nature*, 481:177–181, 2012.

P. Coussot. Saffman-Taylor instability in yield stress fluids. *J. Fluid Mech.*, 380:363–376, 1998.

P. Coussot, A. Ragouilliaux, G. Ovarlez, and B. Herzhaft. Transition from a simple yield stress fluid to a thixotropic material. *AIP Conf. Proc.*, 1027:713, 2008.

P. Coussot, L. Tocquer, C. Lanos, and G. Ovarlez. Macroscopic vs. local rheology of yield stress fluids. *J. Non-Newton. Fluid Mech.*, 158:85–90, 2009.

F. Crameri and B. J. P. Kaus. Parameters that control lithospheric-scale thermal localization on terrestrial planets. *Geophys. Res. Lett.*, 37:L09308, 2010.

F. Crameri, P. J. Tackley, I. Meilick, T. V. Gerya, and B. J. P. Kaus. A free plate surface and weak oceanic crust produce single-sided subduction on Earth. *Geophys. Res. Lett.*, 39(3):L03306, 2012. ISSN 1944-8007. doi: 10.1029/2011GL050046. URL http://dx.doi.org/10.1029/2011GL050046.

M. Darbouli, C. Métivier, J.-M. Piau, A. Magnin, and A. Abdelali. Rayleigh-Bénard convection for viscoplastic fluids. *Phys. Fluids*, 25:023101, 2013.

A. Davaille and C. Jaupart. Transient high-Rayleigh-number thermal convection with large viscosity variations. *J. Fluid Mech.*, 253:141–166, 1993.

A. Davaille and A. Limare. *Laboratory studies of mantle Convection*, volume 7. Elsevier, Amsterdam, Mantle Dynamics edition, 2007.

A. Davaille, E. Stutzmann, G. Silveira, J. Besse, and V. Courtillot. Convective patterns under the indo-atlantic "box". *Earth Planet. Sci. Lett.*, 239:233–252, 2005.

A. Davaille, A. Limare, F. Touitou, I. Kumagai, and J. Vatteville. Anatomy of a laminar starting thermal plume at high Prandtl number. *Exp. Fluids*, 50:285–300, 2011.

A. Davaille, B. Gueslin, A. Massmeyer, and E. Di Giuseppe. Thermal instabilities in a yield stress fluid: Existence and Morphology. *J. Non-Newton. Fluid Mech.*, 193:144–153, 2013.

G. F. Davies. *Dynamic Earth: Plates, Plumes and Mantle Convection*. Cambridge University Press, 1999.

P. R. de Souza Mendes and Eduardo S. S. Dutra. Viscosity function for yield-stress liquids. *Appl. Rheol.*, 14:296–302, 2004.

P. R. de Souza Mendes, M. F. Naccache, P. R. Varges, and F. H. Marchesini. Flow of viscoplastic liquids through axisymmetric expansions-contractions. *J. Non-Newton. Fluid Mech.*, 142:207–217, 2007.

S. Demouchy, A. Tommasi, F. Barou, D. Mainprice, and P. Cordier. Deformation of olivine in torsion under hydrous conditions. *Phys. Earth Planet. Inter.*, 202-203:56–70, 2012.

E. Di Giuseppe, F. Funiciello, F. Corbi, G. Ranalli, and G. Mojoli. Gelatins as rock analogs: a systematic study of their rheological and physical properties. *Tectonophysics*, 473:391–403, 2009.

T. Divoux, D. Tamarii, T. Barentin, and S. Manneville. Transient shear banding in a simple yield stress fluid. *Phys. Rev. Lett.*, 104:1–4, 2010.

T. Divoux, C. Barentin, and S. Manneville. From stress-induced fluidization processes to Herschel-Bulkley behaviour in simple yield stress fluids. *Soft Matter*, 7:8409–8418, 2011. doi: 10.1039/C1SM05607G.

N. Dubash and I. A. Frigaard. Conditions for static bubbles in viscoplastic fluids. *Phys. Fluids*, 16:4319–4330, 2004.

N. Dubash and I. A. Frigaard. Propagation and stopping of air bubbles in Carbopol solutions. *J. Non-Newton. Fluid Mech.*, 142:123–134, 2007.

P. Einarsson and B. Brandsdòttir. *Seismological Evidence for Lateral Magma Intrusion During the July 1978 Deflation of the Krafla Volcano in NE-Iceland*. Raunvísindastofnun Hàskòlans, 1979.

Y. Fialko and J. Pearse. Sombrero uplift above the Altiplano-Puna magma body: Evidence of a ballooning mid-crustal diapir. *Science*, 338:250–252, 2012.

I. A. Frigaard, S. Howison, and I. J. Sobey. On the stability of Poiseuille flow of a Bingham fluid. *J. Fluid Mech.*, 263:133–150, 1994.

I.A. Frigaard and C. Nouar. On three-dimensional linear stability of Poiseuille flow of Bingham fluids. *Phys. Fluids*, 15:2843, 2003.

C. Gabard and J.-P. Hulin. Miscible displacement of non-Newtonian fluids in a vertical tube. *Eur. Phys. J. E Soft Matter*, T 11, Nr. 3:231–241, 2003.

B. Gebhart. Effects of viscous dissipation in natural convection. *J. Fluid Mech.*, 14:225 – 232, 1962.

T. V. Gerya. *Introduction to Numerical Geodynamic Modelling*. Cambridge University Press, 2010.

T. V. Gerya and J.-P. Burg. Intrusion of ultramafic magmatic bodies into the continental crust: Numerical simulations. *Phys. Earth Planet. Inter.*, 160:124–142, 2007.

E. Giannandrea and U. Christensen. Variable viscosity convection experiments with a stress-free upper boundary and implications for the heat transport in the earths mantle. *Phys. Earth Planet. Inter.*, 78:139–152, 1993.

A. Gudmundsson. Form and dimensions of dykes in eastern iceland. *Tectonophysics*, 95: 295–307, 1983.

B. Gueslin, L. Talini, Y. Peysson, B. Herzhaft, and C. Allain. Flow induced by a sphere settling in an aging yield-stress fluid. *Phys. Fluids*, 18:103101, 2006.

I. A. Gutowski, D. Lee, J. R. de Bruyn, and B. J. Frisken. Scaling and mesostructure of Carbopol dispersions. *Rheol. Acta*, 51:441–450, 2012.

U. Hansen and D.A. Yuen. High Rayleigh number regime of temperature-dependent viscosity convection and the Earth's early thermal history. *Geophys. Res. Lett.*, 20: 2191–2194, 1993.

W. K. Hartmann and G. Neukum. Cratering chronology and the evolution of mars. *Space Sci. Rev.*, 96:165–194, 2001.

J. W. Hernlund, C. Thomas, and P. J. Tackley. A doubling of the post-perovskiet phase boundary and structure of the Earth's lowermost mantle. *Nature*, 434:882–886, 2005.

W. H. Herschel and R. Bulkley. Konsistenzmessungen von Gummi-Benzollösungen. *Kolloid-Zeitschrift*, 39:291–300, 1926.

G. Hirth and D. Kohlstedt. Rheology of the upper mantle and the mantle wedge: A view from the experimentalists. In *Inside the Subduction Factory*, volume 138, pages 83–105. AGU, Washington D. C., 2003.

G. Hirth and D. L. Kohlstedt. Water in the oceanic upper mantle: implications for rheology, melt extraction and the evolution of the lithosphere. *Earth Planet. Sci. Lett.*, 144:93–108, 1996.

J. C. R. Hunt. Industrial and environmental fluid mechanics. *Annu. Rev. Fluid Mech.*, 23:1–41, 1991.

L. Guillou C. Jaupart. On the effect of continents on mantle convection. *J. Geophys. Res.*, 100:24217–24238, 1995.

S. Jònsson. Tensile rock mass strength estimated using InSAR. *Geophys. Res. Lett.*, 39: L21305, 2012.

D. Jousselin and A. Nicolas. Oceanic ridge off-axis deep structure in the mansah region (Sumail massif, Oman ophiolite). *Mar. Geophys. Res.*, 21:243–257, 2000.

J. A. Whitehead Jr. and D. S. Luther. Dynamics of laboratory diapir and plume models. *J. Geophys. Res.*, 80:705–717, 1975.

M. Kameyama and M. Ogawa. Transitions in thermal convection with strongly temperature-dependent viscosity in a wide box. *Earth Planet. Sci. Lett.*, 180:355–367, 2000.

E. Kaminski and C. Jaupart. Laminar starting plumes in high-Prandtl-number fluids. *J. Fluid Mech.*, 478:287–298, 2003.

S. Karato. Does partial melting reduce the creep strength of the upper mantle? *Nature*, 319(6051):309–310, January 1986. doi: 10.1038/319309a0.

S. Karato and H. Jung. Effects of pressure on high-temperature dislocation creep in olivine. *Phil. Mag. A*, 83, 3:401–414, 2003.

S. Karato and P. Wu. Rheology of the upper mantle: A synthesis. *Science*, 260:771–778, 1993.

B. J. P. Kaus and Y. Y. Podladchikov. Initiation of localized shear zones in viscoelastoplastic rocks. *J. Geophys. Res.*, 111:B04412, 2006.

J. L. Kavanagh, T. Menand, and R. S. J. Sparks. An experimental investigation of sill formation and propagation in layered elastic media. *Earth Planet. Sci. Lett.*, 245:799–813, 2006.

J. L. Kavanagh, T. Menand, and K.A. Daniels. Gelatine as a crustal analogue: Determining elastic properties for modelling magmatic intrusions. *Tectonophysics*, 582:101–111, 2012a.

J. L. Kavanagh, R. Stephens, and J. Sparks. Insights of dyke emplacement mechanics from detailed 3d dyke thickness datasets. *Journal of the Geological Society*, 168:965–978, 2012b.

D. L. Kohlstedt and M. E. Zimmerman. Rheology of partially molten mantle rocks. *Annu. Rev. Earth Planet. Sci.*, 24:41–62, 1996.

D. L. Kohlstedt, B. Evans, and S. J. Mackwell. Strength of the lithosphere: Constraints imposed by laboratory experiments. *J. Geophys. Res.*, 100:173587–17,602, 1995.

R. Krishnamurti. On the transition to turbulent convection. Part 1. The transition from two- to three-dimensional flow. *J. Fluid Mech.*, 42(2):295–307, June 1970a.

R. Krishnamurti. On the transition to turbulent convection. Part 2. The transition to time-dependent flow. *J. Fluid Mech.*, 42(2):309–320, June 1970b.

R. Krishnamurti. Theory and experiment in cellular convection. *NATO Advanced Study Institute on Continental Drift and the Mechaniscm of Plate Tectonics, University of Newcastl upon Tyne, England*, pages 245–257, April 1979.

L.D. Landau and E.M. Lifshitz. *Theory of elasticity*. Pergamon Press, 1986.

T. Lay, J. Hernlund, and B. A. Buffet. Core-mantle boundary heat flow. *Nature*, 1:25–32, 2008.

D. Lee, I. A. Gutowski, A. E. Bailey, L. Rubatat, J. R. de Bruyn, and B. J. Frisken. Investigating the microstructure of a yield-stress fluid by light scattering. *Physical Review E*, 83:031401, 2011.

F. Maccaferri, M. Bonafede, and E. Rivalta. A numerical model of dyke propagation in layered elastic media. *Geophys. J. Int.*, 180:1107–1123, 2010.

Christopher W. Macosko. *Rheology: principles, measurements, and applications*. VCH, 1994.

M. Manga and D. Weeraratne. Experimental study of non-Boussinesq Rayleigh-Bénard convection at high Rayleigh and Prandtl numbers. *Phys. Fluids*, 11:2969, 1999.

D. Martinand, P. Carriere, and P.A. Monkewitz. Three-dimensional global instability modes associated with a localized hot spot in Rayleigh-Bènard-Poiseuille convection. *J. Fluid Mech.*, 551:275–301, 2006.

A. Massmeyer, E. Di Giusppe, A. Davaille, T. Rolf, and P. J. Tackley. Numerical simulation of thermal plumes in a Herschel-Bulkley fluid. *J. Non-Newton. Fluid Mech.*, 195: 23–45, 2013.

S. Mei and D. L. Kohlstedt. Influence of water on plastic deformation of olivine aggregates: 2. dislocation creep regime. *J. Geophys. Res.*, 105(B9): 21471–21481, 2000. ISSN 2156-2202. doi: 10.1029/2000JB900180. URL http://onlinelibrary.wiley.com/doi/10.1029/2000JB900180/abstract.

T. Menand and S.R. Tait. A phenomenological model for precursor volcanic eruptions. *Nature*, 411:678–680, 2001.

T. Menand, A. Raw, and A. W. Woods. Thermal intertia and reversing buoyancy in flow in porous media. *Geophys. Res. Lett.*, 30:1291, 2003.

C. Metivier and C. Nouar. On linear stability of Rayleigh-Bènard Poiseuille flow of viscoplastic fluids. *Phys. Fluids*, 20:104101, 2008.

T. Mezger and U. Zorll. *The rheology handbook: for users of rotational and oscillatory rheometers*. Coatings compendia. Vincentz, 2002. ISBN 9783878707455.

E. Mittelstaedt and G. Ito. Plume-ridge interaction, lithospheric stresses, and the origin of near-ridge volcanic lineaments. *Geochem. Geophys. Geosyst.*, 6:Q06002, 2005.

P.C.F. Moller, J. Mewis, and D. Bonn. Yield stress and thixotropy: on the difficulty of measuring yield stresses in practice. *Soft Matter*, 2:274–283, 2006.

L. N. Moresi and V. S. Solomatov. Numerical investigation of 2D convection with extremely large viscosity variations. *Phys. Fluids*, 9:2154–2162, 1995.

M. Murakami, K. Hirose, K. Kawamura, N. Sata, and Y. Oshi. Post-Perovskite phase transition in $MgSiO_3$. *Science*, 304:855–858, 2004.

H.-C. Nataf, B. H. Hager, and R. F. Scott. Convection experiments in a centrifuge and the generation of plumes in a very viscous fluid. In *Annales Geophysicae*, volume 2, pages 303–309. May-June 1984.

H.C. Nataf and M. F. Richter. Convection experiments in fluids with highly temperature-dependent viscosity and the thermal evolution of planets. *Phys. Earth Planet. Inter.*, 29:320–329, 1982.

A. R. Oganov and S. Ono. Theoretical and experimental evidence for a Post-Perovskite phase of $MgSiO_3$ in Earth's D" layer. *Nature*, 430:445–448, 2004.

P. Olson and H. Singer. Creeping plumes. *J. Fluid Mech.*, 158:511–531, 1985.

P. Olson, G. Schubert, and C. Anderson. Structure of axisymmetric mantle plumes. *J. Geophys. Res.*, 98 (B4):6829–6844, 1993.

F. Oppong and J. de Bruyn. Mircorheology and jamming in a yield-stress fluid. *Rheol. Acta*, 50:317–326, 2011. ISSN 0035-4511. URL http://dx.doi.org/10.1007/s00397-010-0519-9. 10.1007/s00397-010-0519-9.

J. Peixinho. *Contribution experimentale a l'étude de la convection thermique en regime laminaire, transitoire et turbulent pour un fluide a seuil en ecoulement dans une conduite*. PhD thesis, Université Henri Poincare, 2004.

J. M. Piau. Carbopol gels: Elastoviscoplastic and slippery glasses made of individual swollen sponges: Meso- and macroscopic properties, constitutive equations and scaling laws. *J. Non-Newton. Fluid Mech.*, 144:1–29, 2007.

G. Picard, A. Ajdari, F. Lequeux, and L. Bocquet. Slow flows of yield stress fluids: Complex spatiotemporal behavior within a simple elastoplastic model. *Phys. Rev. E*, 71:010501, 2005.

J. P. Platt and W. M. Behr. Grainsize evolution in ductile shear zones: Implications for strain localization and the strength of the lithosphere. *J. Struct. Geol.*, 33:537–550, 2011.

Jean-Paul Poirier. *Creep of Crystals*. Cambridge Universtiy Press, 1985.

A. M. V. Putz, T.I. Burghelea, I.A. Frigaard, and D.M. Martinez. Settling of an isolated spherical particle in a yield stress shear thinning fluid. *Phys. Fluids*, 20:033102, 2008.

G. Ranalli. *Rheology of the Earth*. Chapman and Hall, London, 2nd edition edition, 1995.

J. T. Ratcliff, P. J. Tackley, G. Schubert, and A. Zebib. Transitions in thermal convection with strongly variable viscosity. *Phys. Earth Planet. Inter.*, 102:201–212, 1997.

Lord Rayleigh. On convection currents in a horizontal layer of fluid, when the higher temperature is on the under side. *Philosophical Magazine Series 6*, 32 (192):529–546, 1916. ISSN 1941-5982. doi: 10.1080/14786441608635602. URL http://www.tandfonline.com/doi/abs/10.1080/14786441608635602.

C. C. Reese and V. S. Solomatov. Heat transport efficiency for stagnant lid convection with dislocation viscosity: Application to mars and venus. *J. Geophys. Res.*, 103:13,643–13,657, 1998.

K. Regenauer-Lieb and D. A. Yuen. Fast mechanisms for the formation of new plate boundaries. *Tectonophysics*, 322:53–67, 2000.

M.-C. Renoult, R. G. Petschek, C. Rosenblatt, and P. Carlès. Deforming static fluid interfaces with magnetic fields: Application to the Rayleigh-Taylor instability. *Exp. Fluids*, 51:1073–1083, 2011.

Y. Ricard and D. Bercovici. Two-phase damage theory and crustal rock failure: the theoretical 'void' limit, and the prediction of experimental data. *Geophys. J. Int.*, 155, Issue 3:1057–1064, 2003.

F. M. Richter. Convection and the large-scale circulation of the mantle. *J. Geophys. Res.*, 78:8735–8745, 1973.

F. M. Richter, H.-C. Nataf, and S. F. Daly. Heat transfer and horizontally averaged temperature of convection with large viscosity variations. *J. Fluid Mech.*, 129:173–192, 1982.

E. Rivalta, M. Böttinger, and T. Dahm. Buoyancy-driven fracture ascent: Experiments in layered gelatine. *J. Volcanol. Geotherm. Res.*, 144:273–285, 2005.

G. P. Roberts and H. A. Barnes. New measurements of the flow-curves for Carbopol dispersions without slip artefacts. *Rheol. Acta*, 40:499–503, 2001.

T. Rolf and P. J. Tackley. Focussing of stress by continents in 3D spherical mantle convection with self-consistent plate tectonics. *Geophys. Res. Lett.*, 38:L18301, 2011.

G. G. Schaber, R. G. Strom, H. J. Moore, L. A. Soderblom, R. L. Kirk, D. J. Chadwick, D. D. Dawson, L. R. Gaddis, J. M. Boyce, and J. Russell. Geology and distribution of impact craters on venus: what are they telling us. *J. Geophys. Res.*, 97:13,257–13,301, 1992.

H. Schmeling, A.Y. Babeyko, A. Enns, C. Faccenna, F. Funiciello, T. Gerya, G.J. Golabek, S. Grigull, B.J.P. Kaus, G. Morra, S.M. Schmalholz, and J. van Hunen. A benchmark comparison of spontaneous subduction models–Towards a free surface. *Phys. Earth Planet. Inter.*, 171(1-4):198–223, December 2008. ISSN 0031-9201. doi: 10.1016/j.pepi.2008.06.028.

D. L. Schutt and C. E. Lesher. Effects of melt depletion on the density and seismic velocity of garnet and spinel lherzolite. *J. Geophys. Res.*, 111:B05401, 2006.

D. R. Scott and D. J. Stevenson. A self-consistent model of melting, magma migration and buoyancy-driven circulation beneath mid-ocean ridges. *J. Geophys. Res.*, 94:2973–2988, 1989.

T. Scott and D. L. Kohlstedt. The effect of large melt fraction on the deformation behavior of peridotite. *Earth Planet. Sci. Lett.*, 246:177–187, 2006.

J. B. Segur and H. E. Oberstar. Viscosity of glycerol and its aqueous solutions. *Ind. Eng. Chem.*, 43:2117–2120, 1951.

P. M. Shearer. *Introduction to Seismology.* Cambridge University Press, 1999. ISBN 9780521669535.

V. S. Solomatov. Scaling of temperature- and stress-dependent viscosity convection. *Phys. Fluids*, 7:266–274, 1995.

V. S. Solomatov and A. C. Barr. Onset of convection in fluids with strongly temperature-dependent, power-law viscosity. *Phys. Earth Planet. Inter.*, 155:140–145, 2006.

V. S. Solomatov and A. C. Barr. Onset of convection in fluids with strongly temperature-dependent power-law viscosity 2. Dependence on the initial perturbation. *Phys. Earth Planet. Inter.*, 165:1–13, 2007.

V. S. Solomatov and L.-N. Moresi. Scaling of time-dependent stagnant lid convection: Application to small-scale convection on Earth and other terrestrial planets. *J. Geophys. Res.*, 105:21795–21817, 2000.

J. F. Steffe. *Rheological methods in food process engineering.* Freeman Press, 1996. ISBN 9780963203618.

C. Stein and U. Hansen. Plate motions and the viscosity structure of the mantle – insights from numerical modelling. *Earth Planet. Sci. Lett.*, 272(1-2):29–40, July 2008. ISSN 0012-821X. doi: 10.1016/j.epsl.2008.03.050.

C. Stein, J. Schmalzl, and U. Hansen. The effect of rheological parameters on plate behaviour in a self-consistent model of mantle convection. *Phys. Earth Planet. Inter.*, 142(3-4):225–255, May 2004. ISSN 0031-9201. doi: 10.1016/j.pepi.2004.01.006.

C. Stein, A. Finnenkötter, J.P. Lowman, and U. Hansen. The pressure-weakening effect in super-Earths: Consequences of a decrease in lower mantle viscosity on surface dynamics. *Geophys. Res. Lett.*, 38:L21201, 2011.

C. Stein, J.P. Lowman, and U. Hansen. The influence of mantle internal heating on lithospheric mobility: Implications for super-Earths. *Earth Planet. Sci. Lett.*, 361:448–459, 2013.

K. Stemmer, H. Harder, and U. Hansen. A new method to simulate convection with strongly temperature-dependent and pressure-dependent viscosity in a spherical shell: Applications to the earth's mantle. *Phys. Earth Planet. Inter.*, 157:223–249, 2006.

H. Tabuteau, P. Coussot, and J. R. de Bruyn. Drag force on a sphere in steady motion through a yield-stress fluid. *J. Rheol.*, 51:125–137, 2007.

P. Tackley. Self-consistent generation of tectonic plates in time- dependent, three-dimensional mantle convection simulations. part 1: Pseudo-plastic yielding. *Geochem. Geophys. Geosys.*, 1:14, 2000a.

P. J. Tackley. Effects of strongly temperature-dependent viscosity on time-dependent, three-dimensional models of mantle convection. *Geophys. Res. Let.*, 20:2187–2190, 1993.

P. J. Tackley. *Three dimensional models of mantle convection: Influence of phase transistions and temperature-dependent viscosity.* PhD thesis, California Institute of Technology, Pasadena, 1994.

P. J. Tackley. Effects of strongly variable viscosity on three-dimensional compressible convection in planetary mantles. *J. Geophys. Res.*, 101:3311–3332, 1996.

P. J. Tackley. Mantle convection and plate tectonics: Toward an integrated physical and chemical theory. *Science*, 288(5473):2002–2007, June 2000b. doi: 10.1126/science.288.5473.2002.

P. J. Tackley. Modelling compressible mantle convection with large viscosity contrasts in a three-dimensional spherical shell using the yin-yang grid. *Phys. Earth Planet. In.*, 171:7–18, 2008.

M. Thielmann and B.J.P. Kaus. Shear heating induced lithospheric-scale localization: Does it result in subduction? *Earth Planet. Sci. Lett.*, 359-360:1–13, 2012. ISSN 0012-821X. doi: 10.1016/j.epsl.2012.10.002. URL http://www.sciencedirect.com/science/article/pii/S0012821X12005511.

R. Trompert and U. Hansen. Mantle convection simulations with rheologies that generate plate-like behaviour. *Letters to Nature*, 395:686–689, 1998.

O. Turan, N. Chakraborty, and R. J. Poole. Laminar natural convection of Bingham fluids in a square enclosure with differentially heated side walls. *J. Non-Newton. Fluid Mech.*, 165:901–913, 2010.

O. Turan, N. Chakraborty, and R. J. Poole. Laminar Rayleigh-Bénard convection of yield stress fluids in a square enclosure. *J. Non-Newton. Fluid Mech.*, 171-172:83–96, 2012.

D. L. Turcotte. An episodic hypothesis for venusian tectonics. *J. Geophys. Res.*, 98: 17,061–17,068, 1993.

H. J. van Heck and P. J. Tackley. Planforms of self-consistently generated plates in 3D spherical geometry. *Geophys. Res. Lett.*, 35:L19312, 2008.

H. J. van Heck and P.J. Tackley. Plate tectonics on super-Earths: Equally or more likely than on Earth. *Earth Planet. Sci. Lett.*, 310:252–261, 2011.

P. van Keken. Evolution of starting mantle plumes: a comparison between numerical and laboratory models. *Earth Planet. Sci. Lett.*, 148 (1):1–11, 1997.

J. Vatteville, P. van Keken, A. Limare, and A. Davaille. Starting laminar plumes: Comparison of laboratory and numerical modeling. *Geochem. Geophys. Geosyst.*, 10:Q12013, 2009.

A. Vikhansky. Thermal convection of a viscoplastic liquid with high Rayleigh and Bingham numbers. *Phys. Fluids*, 21:103103, 2009. doi: 10.1063/1.3256166.

A. Vikhansky. On the onset of natural convection of Bingham liquid in rectangular enclosures. *J. Non-Newton. Fluid Mech.*, 165:1713–1716, 2010.

A. Vikhansky. On the stopping of thermal convection in viscoplastic liquid. *Rheol. Acta*, 50:423–428, 2011.

T. R. Walter and V. R. Troll. Experiments on rift zone evolution in unstable volcanic edifices. *J. Volcanol. Geotherm. Res.*, 127:107–120, 2003.

D. B. White. The planform and onset of convection with a temperature-dependent viscosity. *J. Fluid Mech.*, 191:247–286, 1988.

J.A. Whitehead Jr. and B. Parsons. Observations of convection at Rayleigh numbers up to 760000 in a fluid with large Prandtl number. *Geophys Astro Fluid*, 9:201–217, 1977.

H.-D. Xi, S. Lam, and K.-Q. Xia. From laminar plumes to organized flows: the onset of large-scale circulation in turbulent thermal convection. *J. Fluid Mech.*, 503:47–56, 2004.

M. Yoshida and A. Kageyama. Low-degree mantle convection with strongly temperature- and depth-dependent viscosity in a three-dimensional spherical shell. *J. Geophys. Res.*, 111:1978–2012, 2006.

J. Zhang, S. Childress, and A. Libchaber. Non-Boussinesq effect: Thermal convection with broken symmetry. *Phys. Fluids*, 9:1034, 1997.

J. Zhang, D. Vola, and I. A. Frigaard. Yield stress effects on Rayleigh-Bénard convection. *J. Fluid Mech.*, 566:389–419, 2006.

H. Zhu, Y.D. Kim, and D. De Kee. Non-Newtonian fluids with a yield stress. *J. Non-Newton. Fluid Mech.*, 129(3):177–181, September 2005. ISSN 0377-0257. doi: 10.1016/j.jnnfm.2005.06.001.